"Analytical Modeling and Experimental Characterization of Cathode material for Lithium-ion batteries"

Thesis Submitted to the Delhi Technological University

for the Award of Degree of

Doctor of Philosophy

in

Department of Electrical Engineering

by

Snigdha Sharma

Electrical Engineering Department

Delhi Technological University

Delhi- 110042, India

"Analytical Modeling and Experimental Characterization of Cathode material for Lithium-ion batteries"

Thesis Submitted to the Delhi Technological University

for the Award of Degree of

Doctor of Philosophy

In

Department of Electrical Engineering

By

Snigdha Sharma

Under the guidance of

Prof. M.M. Tripathi

and

Dr. Amrish K. Panwar

Electrical Engineering Department

Delhi Technological University

Delhi- 110042, India

DECLARATION

This is to certify that this thesis entitled **"** ***Analytical Modeling and Experimental Characterization of Cathode material for Lithium-ion batteries*** **"** being submitted for the award of the degree of **Doctor of Philosophy** to Delhi Technological University, India, represents the original research work carried out by me under the supervision of **Prof. M.M.Tripathi** and **Dr Amrish K. Panwar**, Electrical Engineering Department, Delhi Technological University, India. The results obtained in this thesis have not been submitted in part or full to any other University or Institution for the award of any degree or diploma.

Date: …….. **Snigdha Sharma**

Place: ……. (Enrollment No- 2K17/PHD/EE/03)

Delhi Technological University

Certificate

This is to certify that the research work embodied in the thesis titled **"Analytical Modeling and Experimental Characterization of Cathode material for Lithium-ion batteries"** is the result of original research carried out in the Electrical Engineering Department, Delhi Technological University, for the award of **Doctor of Philosophy** under the supervision of **Prof. M.M.Tripathi** and **Dr. Amrish K. Panwar**. The candidate claims to the best of his knowledge that this work has not been submitted elsewhere for the award of any degree to any other University or Institution.

Snigdha Sharma
(Enrollment No- 2K17/Ph.D/EE/03)

This is to certify that the above statement made by the candidate is correct to the best of our knowledge.

(Prof. M.M. Tripathi)
(Supervisor)
Professor
Electrical Engineering Department
Delhi Technological University
Delhi, India

Dr. Amrish K. Panwar
(Co-Supervisor)
Assistant Professor
Department of Applied Physics
Delhi Technological University
Delhi, India

Through:

Prof. Rachna Garg
Head of Department (HOD)
Electrical Engineering Department
Delhi Technological University
Delhi, India

Dedicated to……
My Teachers and Family

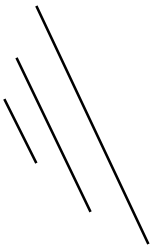

Acknowledgment

At this juncture of fulfilling my desire for satisfactory completion of the present work, I bow before the almighty god to express my deep gratitude for the divine grace. This work would not have the spirit without the invaluable academic, educational, psychological, and human support and belief in me as a writer and researcher, provided by the following:

I would like to express my indebtedness and gratitude to my supervisor **Prof. M.M. Tripathi** and my co-supervisor **Dr. Amrish K. Panwar** for the continuous support of my Ph.D. study and related research for his patience, motivation, and immense knowledge. His guidance helped me in all the time of research and writing of this thesis. I could not have imagined having a better advisor and mentor for my Ph.D. study. Your advice on both research as well as on my career has been priceless.

I would like to extend my regards and cordial thanks to **Prof. Rinku Sharma** (HOD, Department of Applied Physics, Delhi Technological University for providing the necessary facilities in the department for carrying out my research work.

I would also like to thank all the faculty members of the Electrical Engineering department and Department of Applied Physics, for their round the clock availability regarding research and non-research related works.

I gratefully acknowledge the kind support and continuous motivation from my seniors and colleagues, who helped me throughout this journey. I gratefully acknowledge them for creating a friendly atmosphere at the work place and extending all possible help during the course of my experiments. I wish all of them a great career and joyful life.

I am obliged to Mr. Sandeep (Advanced Instrumentation Centre, DTU) for technical help in XRD and SEM facilities.

I would like to acknowledge the support of Tequip-III and Delhi Technological University, India, for fellowship.

I cannot explain how thankful I am to my friends who has always been there for me. It is their continuous moral support and encouragement without which this thesis would not have been possible. No matter where I go, they will always remain in my heart. I wish them best wishes in career and life.

I owe this thesis to my parents and family for their loving support, patience and sacrifice that sustained me through the best and worst of times. Last but not the least, I am thankful to my relatives and close friends for their immense patience and moral support during the course.

My final words of thanks are for my God, for his constant support and companionship through all turmoil of my life.

Date: …… **(Snigdha Sharma)**

Place: ……...

Contents

List of Figures

List of Tables

List of Publications

Published work:

- ***Journal Papers/ Book Chapter***

1. **Snigdha Sharma, Amrish K. Panwar, and M.M. Tripathi** "Multiscale Modelling and Experimental Characterization for Enhancement in Electrical, Mechanical and Thermal Performances of Lithium-ion Battery", Journal of frontiers energy research, 2022 **(SCIE, I.F. 4.8). Doi:** https://doi.org/10.3389/fenrg.2022.851377

2. **Snigdha Sharma, Amrish K. Panwar and M.M. Tripathi** "Electrochemical thermal modeling and Analysis of different Cathode- Anode pairs for lithium-ion battery", Journal of advances in electrical and computer Engineering, vol.21, no.3, pp.57-64, 2021, doi:10.4316/AECE.2021.03007 **(SCI-E, I.F. 1.221).**

3. **Snigdha Sharma, Amrish K. Panwar and M.M. Tripathi** "Storage technologies for Electric Vehicle", Journal of Traffic and Transportation Engineering, ELSEVIER, ISSN: 2095-7564, volume 7, issue 3, June 2020, p.p. 340- 361 **(ESCI & SCOPUS I.F 6.306)**

4. **Snigdha Sharma, Amrish K. Panwar and M.M. Tripathi** "Investigation of 3D Electrochemical, Thermal and Electrical Performance of Lithium-ion Battery module in a high-temperature", International Journal of Renewable Energy Development, ISSN: 2252-4940, DOI: 10.14710/ijred.9.2.151-157 **(ESCI & SCOPUS IF 2.49)**

5. **Snigdha Sharma, Amrish K. Panwar and M.M. Tripathi**, "Enhanced Electrical and Mechanical characteristics monitored by Various software for Lithium-ion Battery Tests" Energy Systems, Drives, and Automations, Proceedings of ESDA 2019, Lecture Notes on Electrical Engineering 664, Springer-Nature ISBN 978-981-15-5089-8 **(Book Chapter).**

6. **Snigdha Sharma, Amrish K. Panwar and M.M. Tripathi** "Experimental characterization and Multiphysics 1D simulation of cathode material for evaluating the performance of the lithium-ion battery", Journal of Engineering Research**, SCIE Indexed (I.F 0.387**). (**Communicated**)

7. **Snigdha Sharma, Amrish K. Panwar and M.M. Tripathi "**Experimental characterization integrated with Computational Approach for Novel Olivine- Spinel Dual Composite ($LiFePO_4$-$LiMn_2O_4$) Cathode Material for Lithium-ion Batteries**",** Journal of Physics, **SCIE Indexed (I.F 0.387**). (**Communicated**)

- ***International Conferences***

1. **Snigdha Sharma, Amrish K. Panwar and M.M. Tripathi**, "Experimental characterization and Multiphysics 1D Simulation of Cathode Material for Evaluating the Performance of Lithium-Ion Battery " 6th International conference on Advanced Production and Industrial Engineering, ICAPIE-2021, DTU, New Delhi, India.

2. **Snigdha Sharma, Amrish K. Panwar and M.M. Tripathi,** "Electrical and Thermal Characterization of Lithium-Ion Batteries with the help of Hardware and Software Simulation" 236th ECS meeting, 13-17 Oct 2019, Atlanta, Georgia, U.S.A.

3. **Snigdha Sharma, Amrish K. Panwar and M.M. Tripathi,** "Enhanced Electrical and Mechanical characteristics monitored by Various software for Lithium-ion Battery Tests" 2nd International Conference on 'Energy Systems, Drives, and Automations', ESDA 2019, 28-29 December 2019, Kolkata, India.

4. **Snigdha Sharma, Amrish K. Panwar and M.M. Tripathi,** "3D simulation of Electrochemical, Thermal and Electrical Performance of Lithium-ion Battery module in different temperature" 13th National Conference on Solid State Ionics (NCSSI-13), 16-18 December 2019, IIT Roorkee, India.

5. **Snigdha Sharma, Amrish K. Panwar and M.M. Tripathi,** "Investigation of 3D Electrochemical, Thermal and Electrical Performance of Lithium-ion Battery module in a high-temperature environment" 2nd international conference on Sustainable Technologies for Environment Management, 25-26 March 2019, DTU, New Delhi.

6. **Snigdha Sharma, Amrish K. Panwar and M.M. Tripathi**, "Structural and Electrochemical Investigation of Olivine Type LiMnPO4 cathode material for Lithium-ion Batteries" International meeting on energy storage Devices (IMESD-2018), 10-12 December 2018, IIT Roorkee, India.

Abstract

Lithium-ion battery technology is proving to be one such technology that can meet the requirements of high energy density, good power density, non-toxicity, good cyclability, environmental friendly, and cost-effectiveness. It is being extensively used to power the range of products or systems including portable electronic products, large-scale power storage in smart grids, computing and communications devices, military and automotive as well as Electric Vehicles (EVs) and Hybrid Electric Vehicles (HEVs), etc. The cathode material present in lithium-ion batteries, together with the anode, separator, and electrolyte, plays a crucial role in the energy and power density factor. The fabrication of a lithium-ion cell with high energy content, low price, lightweight, long life, and environmental compatibility strongly depends on the crystallographic structure of the cathode materials. Cathode materials currently used or processed can be classified into three different types depending on the dimensions in which lithium ions can move such as layered type (2-D), Spinel type (3D), and Olivine type (1-D).

This research work is focused on the spinel and olivine-type structure of cathode material. Spinel-type structure cathodes allow the lithium intercalation pathways in all three dimensions. Spinel compounds are generalized as AB_2O_4 (A = Li, B = Mn, Ni). $LiMn_2O_4$ is the most studied material in this category. It is a low-cost material and has better cycling stability at 4V redox potential, but delivers lower discharge capacity compared to the layered cathode material. Similarly, Olivine type structure cathodes lie in the category of "polyanion compounds" which contain $(XO_4)^{n-}$ (X = P, Si, etc.) tetrahedral anion structural units with a strong covalent X-O bonding network. This structure proves a very promising material in terms of structure stability, a flat voltage plateau, and high theoretical capacity.-$LiFePO_4$ is one such cathode material that falls in olivine-type materials. However, its sluggish lithium-ion diffusion kinetics and poor conductivity limit its commercial use.

In spite of the rigorous research work on spinel-$LiMn_2O_4$ and olivine-$LiFePO_4$ cathode material, a comprehensive study of the change in electrical and electrochemical studies still lacks which prompted to carry out the present research work on spinel and olivine-based cathodes. In order to enhance the characteristics of cathode material, multiple solid solutions of the AB_2O_4- ABO_2 type have gained impressive attention from the research community. Therefore, to provide optimum solution, a series of novel spinel-olivine dual composites ($LiFePO_4$- $LiMn_2O_4$) have been included in the current research work.

This thesis presents a brief introduction to battery technology, focusing on different types of cathode materials for rechargeable lithium-ion batteries. Various types of existing cathode materials have been extensively studied. Among these cathode materials, spinel and olivine type cathode material and their composites have been identified as the potential cathode material for the present study. Hence, literature review on different cathode materials, synthesis, and characterization techniques used for $LiFePO_4$, $LiMn_2O_4$, and their composites has been presented.

In addition, the modeling and simulation approach was also demonstrated to analyze the thermal, electrical, electrochemical, and mechanical properties of different cathode materials. This modeling approach provides a benchmark for new researchers to validate and investigate the electrical, electrochemical, thermal and controlling the internal impedance parameters of the battery.

For the synthesis of the pure phase cathode materials, sol-gel and planetary ball milling methods were used. This work provides details on experimental conditions and parameters used for various physicochemical characterization techniques such as thermogravimetric analysis (TGA), X-ray diffraction (XRD), SEM/TEM, FTIR, I-V, and activation energy measurements. The instrument and conditions used in the electrochemical analysis, such as cyclic voltammetry (CV), electrochemical impedance spectroscopy (EIS), and galvanostatic charge/discharge tests through the coin cell assembly are also given.

Furthermore, the modeling and simulation of cathode material with spinel and olivine structure was performed and the various internal parameters such as electrolyte concentration, battery potential, thermal runaway, internal impedance control parameters, and many more were analyzed. In addition, a new computational model for dual composites was simulated to study the properties of the cathode material at high temperatures.

In addition, after evaluating the computational results, the experimental characterization was performed to develop a spinel and olivine structure cathode material. The synthesized composition for spinel-type cathode material, $LiMn_2O_4$ found that XRD results show that the synthesized sample was crystalline in nature and also reveals the formation of the spinel phase and cubic structure of the LMO material. The SEM characterization reveals the spherical morphology with the average grain size of 8-10 μm grain size of the LMO material. FTIR study helps to determine the vibrational modes across the metal-oxygen bonds of the LMO material and the electrical characterization reveals better electronic conductivity as the resistance was low which is evaluated with the help of activation energy. Similarly, the olivine type structure,

$LiFePO_4$ composition was characterized and evaluated with all the physio-chemical and electrochemical performances. Therefore, after evaluating both the materials, a novel olivine-spinel dual composite is synthesized.

The olivine part is represented by $LiFePO_4$ (LFP) while the spinel part includes the $LiMn_2O_4$ (LMO). Different weight ratios of LFP and LMO were mixed by means of ball-milling named 1LFP/1LMO, 3LFP/1LMO, and 1LFP/3LMO, which refers to different mass ratios 1:1, 3:1, and 1:3, respectively, with olivine and spinel structure to form the intercalation cathode. It has been found that 1LFP/3LMO shows good cycling stability and also contributes to the enhancement of ionic conductivity which can be attributed to all the electrochemical and electrical characterization. 1LFP/3LMO also shows a good discharge capacity curve as compared to other solid solutions at a 1C rate.

After evaluating the simulation and experimental results, the hardware prototype was designed to evaluate the electrical characteristics of the lithium-ion coin cell. This coin cell was fabricated in a research laboratory and used to develop a battery bank. However, this coin cell was used to develop a battery bank for a hardware prototype. This hardware was interfaced with software through the NI-6001 DAQ card and the results were optimized with the help of data acquisition software. The main focus of this experiment is to optimize the electrical characteristics such as battery voltage and current during discharge conditions and also perform battery external short circuit tests for boosting battery characterization. The capacitor bank has been connected in parallel fashion with the battery bank to reduce the fluctuation as well as for enhancement in electrical characteristics.

After performing all the simulation and experimental research work, the results helps to conclude that the dual composite cathode material of 1LFP/3LMO is having superior thermal, electrical and conductive properties as compare to other cathode material. This dual composite cathode material also proofs good electrical properties as a battery bank on hardware system which clearly demonstrates that the dual composite 1LFP/3LMO cathode material is used for high power practical application.

Also, in the future, all the simulation, experimental, and hardware set-up results will be tested for prototype and large-scale battery devices.

Chapter 1 : Introduction and Literature Review

This chapter illustrates a brief overview of the developed primary and secondary battery systems and various types of cathode material developed for lithium-ion batteries (LIBs). Among developed cathode materials, Spinel and Olivine-type structures are considered potential cathode materials. Moreover, a spinel-olivine cathode material composite has also been investigated in this study. The goal of choosing an alternative cathode material for lithium-ion batteries (LIBs) is to achieve high power density, cycling life, and energy density, and to improve other electrochemical properties. These materials are mainly focused on high-energy storage applications such as the automotive industry, energy storage systems (replacement of lead-acid batteries), telecommunication, Diesel generator amendment, and robotics automation systems.

Introduction and Literature Review

1.1 History

Energy storage devices are on high priority to support the growing need for clean energy and a sustainable environment since they are becoming prevalent in numerous industries such as the vehicle sector, communication sector, power sector, and many others [1-3]. Increasing pressure on non-renewable energy sources, limited supplies, and their undesirable side effects such as greenhouse gas production, global warming, and post-use environmental degradation have forced humanity and researchers worldwide to seek alternative energy sources or technologies that prove to be less hazardous to health and environmentally friendly and cover the rapidly growing demand for energy. Among numerous bloomed technology, one such substitute technology is an electric vehicle (EV) which is fastly growing a part of the modern transportation system. According to Chan [4-5], energy and environmental issues have led to the development of EVs where the integration of automobile and electrical engineering is done to achieve high-performance electric vehicles. In the upcoming time, EVs are major field to play an important role in road transportation because of alternate energy sources i.e. secondary batteries, and they may also assist in reducing the environmental pollution. Additionally, EVs may provide power to the electric grid whenever needed form the lithium-ion batteries. The industries require surplus energy from Li-ion batteries because of their power density and energy density, LIBs are the fastest-growing and the most commonly used energy storage technologies on the market today [8-10]. The evolution of lithium-ion batteries began in the 1970s [7-8]. The first lithium-ion battery was launched in the market with a coke-based anode electrode, and then, graphite material was used as anode material in the mid-90s. Similarly, lithium-ion battery cathode materials were also used and they had different materials which have different types of structures such as layered (Li-cobalt oxide ($LiCoO_2$)), spinel, olivine, or a tunneled structure known as Li-manganese oxide ($LiMnO_2$) and many more [10]. Now the

current scenario of the Lithium Ion Battery market is in high demand. The global energy storage projection market is shown in figure 1.1. The global market of LIBs is projected to increase up to fourfold by 2030 because of the adoption of EVs i.e. 2500 GWh capacity whereas other stationary applications gives the deployment of 2-30 times.

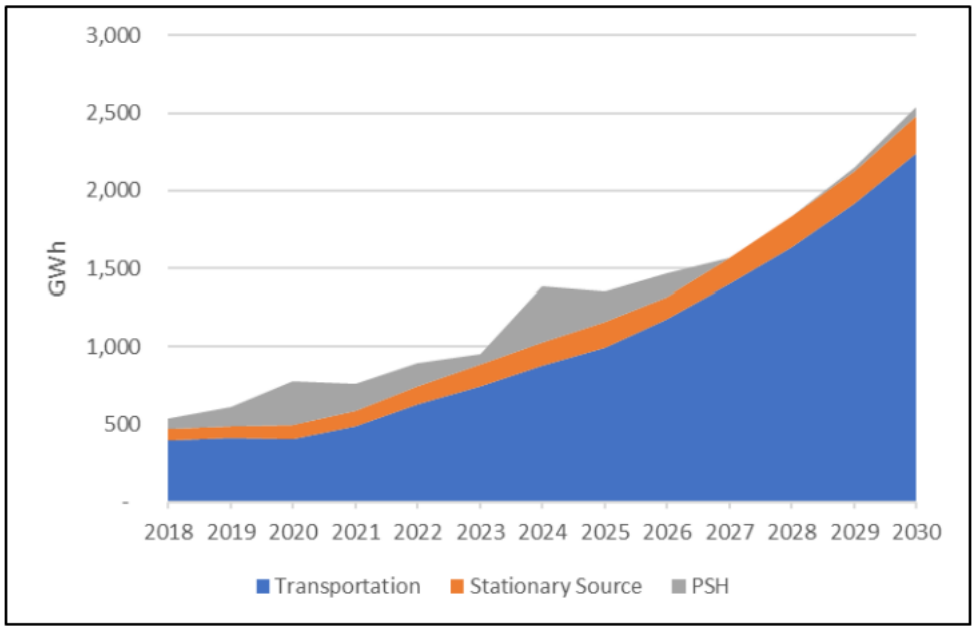

Figure 1.1 *Global market of Energy Storage [10].*

1.2 Types of Energy Storage and Conversion Devices

There are multiple types of energy storage and conversion sources that controls and regulates the flow of energy. At present, the primary emphasis is on energy storage and its essential characteristics such as storage capacity, energy density, power density, and many more. Hence, there are some essential energy storage and conversion system being used so far as;

a. Batteries
b. Super Capacitors
c. Fuel cells
d. A hybrid energy storage system

This type of classification can be rendered in various fields, and analysis can be abstract according to applications [11]. According to Electric Vehicles applications, the electrochemical

ESS is of high priority such as batteries, super capacitors, and fuel cells. An electrochemical system deals with electrochemistry, i.e., the shifting of electrons with the help of chemical reactions at the interface of the electrode and the electrolyte [12-15]. Many other energy-stored devices based on electrochemistry have been fabricated which are named primary and secondary batteries, super capacitors, Fuel cells, electrolyzer, and many more [13].

1.3 Batteries

An electrochemical cell that transforms chemical energy into electrical energy through a redox reaction process is called as battery. There are two types of batteries which can depend on several factors such as reversibility process, charging and discharging and stored capacity.

1.3.1 Primary and Secondary Batteries

The primary batteries are those non-rechargeable batteries that can transforms chemical energy into electrical energy only once in a lifetime and then discarded such as Zinc- carbon/air, manganese dioxide etc. whereas the secondary batteries are rechargeable batteries that are designed for repetitive charge and discharge process such as lead acid, Ni, Lithium-ion.

1.3.1.1 Primary Batteries

The first primary battery was introduced more than 100 years ago, Zinc-carbon was the only battery used in 1940 [15]. After that, many advancements were taken place in primary cells regarding its capacity, operating temperature, life cycle, etc. Hence, there are many primary cells designed using various anode-cathode combinations and some of them are briefly discussed in Table 1.1 [13-14, 17-18].

Table 1.1 *Comparison of Primary Batteries.*

Primary Batteries	Cathode Material	Anode Material	Electrolyte/ Reaction	Nominal Voltage/Current	Practical Capacity
Zinc-Carbon & Alkaline Manganese	*MnO_2*	*Zn*	*Aqueous KOH/NH_4Cl[110]* *$Zn + 2MnO_2 \rightarrow +2H_2O$* *$2MnOOH + Zn(OH)_2$* *$Zn + 2MnO_2 \rightarrow ZnO + Mn_2O_3$*	*0.16 to 44 Ah*	*75 to 35 Ah/Kg*
Zinc-Air	*O2*	*Zn*	*Alkaline electrolyte* *$Zn + 2OH^- \rightarrow Zn(OH)_2 + 2e^-$ (Anode)* *$O_2 + 2H_2O + 4e^- \rightarrow 4OH^-$ (Cathode)* *$Zn + ½\ O_2 \rightarrow ZnO$ (Overall reaction)*	*0.4 to 2 mA*	*40 to 600 mAh*
Silver-Oxide	*Zn*	*Ag_2O*	*KOH or NaOH aqueous electrolyte* *$Zn + Ag_2O \rightarrow ZnO + 2Ag$ (Overall reaction)*	*1.5 to 1.6 V*	*165mAh*
Lithium Sulfur dioxide	*Teflon-bonded acetylene black*	*Li*	*$2Li + 2SO_2 \rightarrow Li_2S_2O_4$ (Overall reaction)*	*2.7 to 2.9 V*	*~260Wh/Kg*
Lithium-Thionyl Chloride	*Porous Carbon*	*Li*	*$4Li + 2SoCl_2 \rightarrow 4LiCl + S + SO_2$ (Overall reaction)*		*450 to 600 Wh/Kg*
Lithium-Manganese Dioxide	*MnO_2*	*Li*	*Ion Conducting Organics* *$Li \longrightarrow Li^+ + e^-$ (Anode)* *$2MnO_2 + Li^+ + e^- \longrightarrow MnO_2^-(Li^+)$(Cathode)* *$MnO_2 + Li \longrightarrow MnO_2^-(Li^+)$ (Total Reaction)*	*3.60*	*200 Wh/Kg*
Lithium-Carbon Monofluoride	*Polycarbon fluoride*	*Li*	*$xLi + CFx \longrightarrow xLiF + xC$ (Overall reaction)*	*2.8 V*	*200 to 600 Wh/Kg*

1.3.1.2 Secondary Batteries

A secondary battery are named as a rechargeable batteries which work as an energy storage system as well as an energy source system. The preliminary battery system of rechargeable battery is lead-acid (Pb) battery, which was introduced by French physicist 'Plante' in 1858 [19-20]. With overdue of time, the nickel-iron (Ni-Fe) alkaline battery was inaugurate by Edison in 1908 as a power source for the electric transportation system [17, 21-23]. Similarly, other critical commercialized rechargeable batteries are summarized in Table 2.2 [13].

A. Lead-acid Batteries

The lead-acid battery was the very commercialize battery in the early era, as this battery was introduced by French physicist in 1859 [13]. As compared with other battery it shows certain advantages such as a high voltage of the cell (2V), high electrochemical activity, low-price, long-life span and excellent reliability [13]. The main components of the lead-acid battery are electrodes, separator, and electrolyte.

Table 1.2 *Comparison of Secondary Batteries.*

SECONDARY BATTERIES	CATHODE MATERIAL	ANODE MATERIAL	ELECTROLYTE/REACTION	NOMINAL VOLTAGE/ CURRENT	PRACTICAL CAPACITY
Lead-Acid	PbO_2	Pb	H_2SO_4 aqueous Solution $Pb + SO_4^{2-} \leftrightarrow PbSO_4 + 2e^-$ (Anode) $PbO_2 + 4H^+ + SO_4^{2-} + 2e^- \leftrightarrow PbSO_4 + 2H_2O$(cathode) $PbO_2 + 2PbSO4 + Pb \leftrightarrow PbSO4 + 2H2O$ (total Reaction)	2V	30 to 50 Wh/Kg
Nickel-Cadmium	NiOOH	Cd	KOH aqueous Solution $Cd + 2OH^- \leftrightarrow Cd(OH)_2 + 2e^-$(Anode) $2NiOOH + 2H_2O + 2e^- \leftrightarrow 2Ni(OH)_2 + 2OH$ (Cathode) $2NiOOH + Cd + 2H_2O \leftrightarrow Ni(OH)2 + Cd(OH)2$ (Total Reaction)	1.2 V	50 Wh/Kg

Nickel-Metal Hydride	NiOOH	Hydrogen Adsorbed Alloy	KOH aqueous Solution $H_2 + 2OH^- \leftrightarrow 2H_2O + 2e^-$ (Anode) $2NiOOH + 2H_2O + 2e^- \leftrightarrow 2Ni(OH)_2 + 2OH$ (Cathode) $2NiOOH + H_2 \leftrightarrow 2Ni(OH)_2$ (Total Reaction)	1.2 V	100 Wh/Kg
Lithium-ion	$LiCoO_2$	C+Li/Li	Organic Electrolyte +Lithium Salt $Li\ (C) \leftrightarrow Li_{(1-X)}(C) + xLi^+ + xe^-$(Anode) $xLi^+ + xe^- + Li_{(1-X)}CoO_2 \leftrightarrow LiCoO_2$ (Cathode) $Li\ (C) + Li_{(1-X)}CoO_2 \leftrightarrow LiCoO_2$ (Total Reaction)	3.6 V	150 to 200 Wh/Kg
Lithium-Sulfur	S	Li	Liquid electrolyte $Li_2S_8 + 2e^- + 2Li^+ \leftrightarrow 2Li_2S_4$ $Li_2S_4 + 2e^- + 2Li^+ \leftrightarrow 2Li_2S_2$ $Li_2S_2 + 2e^- + 2Li^+ \leftrightarrow 2Li_2S$	2.15 V	2600 to 2800 Wh/Kg
Lithium - Air	$LiCoO_2$	C	Liquid or Gel electrolyte $2Li + O_2 \leftrightarrow Li_2O_2$ $4Li + 6H_2O + O_2 \leftrightarrow 4(LiOH.H_2O)$	3.1 V	3620 to 5200 Wh/Kg

In this, the lead di-oxide serves as a positive electrode and Pb serves as a negative electrode, which is submerged in a liquid solution of sulfuric acid known as electrolyte [24]. These batteries have different types of construction such as tubular, bipolar and prismatic type with grid or tubular plates and hence lead to variable characteristics. Since in this Pb-acid rechargeable battery is more substantial in weight, so its specific energy is low 30-50 Wh/Kg [13].

B. Nickel-cadmium (Ni-cd) Battery

Nickel batteries were introduced in 1908-1909 by Edison as a power source for various applications. There are five rechargeable batteries, which belong to Nickel groups named as Ni-Cadmium, Ni-H_2, Ni-Metal hydride, Ni-Zinc and Ni-iron batteries [13]. Presently, Ni-Cadmium (Ni-cd) batteries have two different structures; sealed type and vented type. In all classes of battery, β-NiOOH is used as a cathode and Cadmium is used as an anode. The aqueous KOH solution acts as an electrolyte for LiOH, which helps in improving cycle life as

well as its temperature performance [13]. The advantages of Ni-Cd over other types of batteries are high rate capability and excellent lifespan up to ten years in an optimum temperature range (-30^{o}C to 80^{o}C) [25]. On the other hand, these batteries rapidly lose their capacity at ambient temperature and the major drawback with Ni-cd was very toxic as well as very heavy metal [25].

C. Nickel- metal hydride (Ni-MH) Battery

Nickel-metal hydride battery was first instigate in 1960s as a substitute for both Ni-Cd and Ni-H_2 batteries because of its advantages such as lower pressure, high energy, and low cost as compare to Ni-Cd. The commercialization of Ni-MH rechargeable battery was carried out in the year 1989 for multiple applications such as portable computers, electronic devices, and hybrid vehicle propulsion systems [26]. In Ni-MH battery, the hydrogen alloy is used an anode and β-NiOOH is used as an cathode. During overcharge process, both hydrogen (H_2) and oxygen (O_2) evolve from the cathode and reunite to form H_2O. The energy density of the cell can approach 100Wh/Kg and 300 Wh/L [13]. However, there are significant issues with Ni-MH, which is yet to be solved such as limited high self-discharge, poor low-temperature capability and also high rate capability [13].

D. Lithium-Ion Battery

Lithium-ion secondary batteries have the highest specific energy and energy density of any other secondary batteries [13]. The creation of lithium-ion batteries began in the 1970s [27-28]. An older cathode material for lithium-ion batteries has various layered structures denoted by the names Li-cobalt oxide ($LiCoO_2$) or li-manganese oxide ($LiMnO_2$) [29]. Other metal oxide substances that function as cathodes include $LiMn_2O_4$, $LiFePO_4$, $LiNi_{1-x}Mn_xCo_yO_2$, and many others. [13]. By combining lithium cobalt oxide, $LiCoO_2$, as the cathode material and graphite carbon, C, as an anode, Sony Energy produced the first lithium-ion battery for

commercial use in the years 1990–1991 [13]. The capacity of the graphite is very high (350 Ah/Kg) comparing with the $LiCoO_2$ (~140 Ah/Kg). The advantages of rechargeable lithium-ion batteries are good energy density and power density, long cyclic performance, low memory effect, low self-discharge, etc. However, the disadvantages of rechargeable lithium-ion batteries include their high cost, Co toxicity, and unsafe operation at high temperatures (>100 ˚C), which results in the breakdown of the positive electrode and the electrolyte and the release of gas. [13]. Further, to overcome many drawbacks in existing lithium-ion battery system and to improve electrochemical properties, next generation of lithium based rechargeable energy storage systems are being explored as lithium-sulfur and lithium-air batteries [14-20].

E. Lithium-sulfur and Lithium-air Batteries

In 1962, sulfur type battery had been introduced, but there are particular issues that are still not solved such as the solubility of polysulfide in general liquid organic electrolyte and insulating in nature [30]. Lithium-sulfur battery also shows low coulombic efficiency due to its shuttling effect and its capacity fades rapidly [31]. Based on the overall reaction $S_8 + 16\ Li = 8\ Li_2\ S$, it exhibits a voltage of 2.16 V, an energy density of 2600 Wh/Kg (or 1800 Wh/L), and a specific capacity of 1676 mAh/g, making it five times more powerful than conventional batteries [32-34]. Moreover, the modern advancement in Li-sulfur batteries has been done because of the increasing demands of high storage energy system, and it also gives many opportunities to solve their issues related to bulk material's conductivity [35-38]. The other most developing Li batteries regarding energy density are Lithium-air system since the cathode active mass material is not included in these batteries. The excellent advantage of the lithium-air battery is its energy density of 3621 Wh/Kg (when discharged to Li_2O_2 at 3.2V) or 5210 Wh/kg V (when discharged to Li_2O at 3.2V).

1.3.1.3 Focused on Lithium-ion Batteries (LIBs)

Lithium-ion batteries (LIBs) provide the most complete performance among the several rechargeable battery types investigated because of a number of benefits and a wide range of application possibilities [39-41]. The following are some of the most crucial factors for the introduction of lithium-ion batteries (LIBs):

- Lithium metal is very light in weight, silver-white in appearance and has a low density.
- LIBs have a high specific energy and high energy density.
- The Li/Li^+ in the electrochemical system of LIBs have a high electric potential because it can lose its outer valence electron very easily with counter electrode.
- It has flat discharge characteristic as well as low self-discharge.
- LIBs show long cycling life (Charge/ discharge) and vast discharging temperature range (-20 °C to 65 °C).
- These batteries have negligible Memory Effect.

Hence, Due to multiple advantage, the present global market has easily adopted the LIBs for diverse applications. The working principle of LIBs has been briefly explained in figure 1.2.

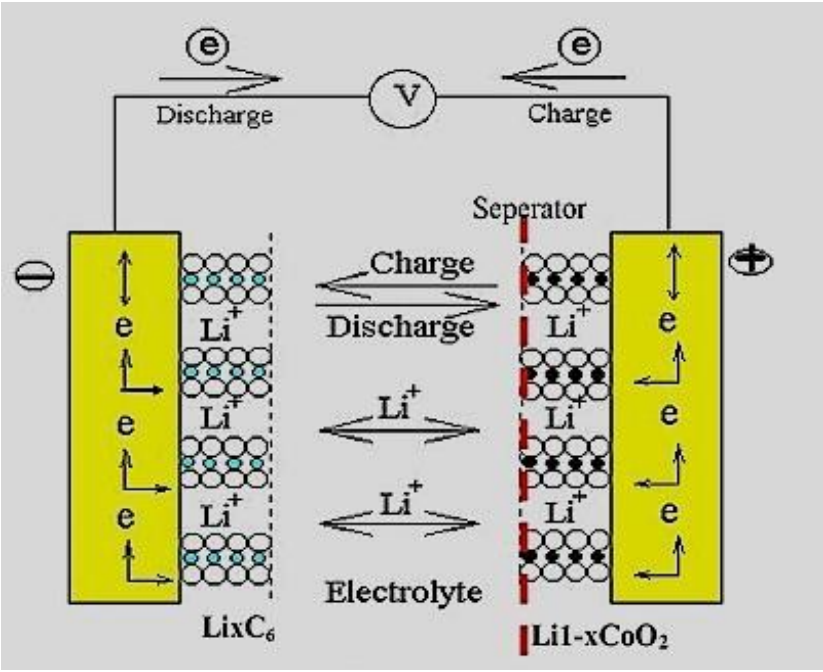

Figure 1.2 *Charge and discharge (redox reaction) process in LIBs [43].*

In lithium-ion cell, the six major components were aligned in a sequential manner such as cathode, positive current collector (CC), separator, electrolyte, anode, and negative current collector (CC) respectively. In this, the function of electrolyte is to provide a smooth passage for the flow of ions during reduction and oxidation process. The function of electrodes is to provide the potential through an electrochemical redox process as per the material of the electrodes and in this, electrodes were directly make a contact with the aluminum current collector on the positive electrode and the copper current collector on the negative electrode to make a proper conduction across the circuit. Li ions moved back and forth between the two electrodes during the charging and discharging operation from the cathode to the anode. Furthermore, the complete process of the lithium-ion cell would only focus on two cathode and anode materials of the electrodes. Therefore, cathode electrode material was chosen during this present study.

A. Types of cathode materials

Since, the inception of the first commercially available rechargeable lithium ion battery prepared by $LiCoO_2$ based cathode material, the investigation of alternative cathode materials in ongoing. $LiCoO_2$ itself has high theoretical capacity and good electrochemical properties. $LiCoO_2$ and $LiNiO_2$ both the layered type cathode has high theoretical capacities of 274 mAh/g and 275 mAh/g, respectively [44]. However, when $LiCoO_2$ is employed in practice, its actual capacity is reduced by half due to several drawbacks. Although $LiNiO_2$ (LNO) was considered as an alternative option because LNO is having theoretical capacity almost equal to $LiCoO_2$, and also available abundantly as raw materials. But due to structural instability and blockage of lithium-ion diffusion by Ni^{3+}, the electrochemical performance is affected [45]. Further, to overcome the issues in layered intercalation type cathode materials, another spinel and olivine type intercalation cathode materials were developed. $LiFePO_4$ (LFP), olivine is known as a suitable intercalation cathode material for today's LIBs because of certain supremacy such as

good theoretical capacity, 170 mAh/g, strong thermal stability, and adequate raw materials. It is being used as cathode material from small portable gadgets to hybrid electric vehicles [46, 47]. Unfortunately, because of poor electrical and ionic conductivities, the pristine $LiFePO_4$ has slow kinetics. Among all of these cathode materials, $LiMn_2O_4$ (LMO) cathode material was considered as alternative cathode because of its 3-D spinel phase structure as well as high theoretical capacity, 148 mAh/g [10]. LMO has several advantages over other cathode materials, including low manufacturing costs, environmental friendliness, simple synthesis procedures, high-rate capacity as well as low internal resistance [48]. Similarly, many other composition of cathode materials for rechargeable lithium-ion battery were also explored for these three classes of layered, spinel and olivine as reported in Table 1.3 [9-10].

Table 1.3 *Different types of Cathode Structures [49].*

S.No	Layered Structure	Spinel Structure	Olivine Structure
1	$LiCoO_2$	$LiMn_2O_4$	$LiFePO_4$
2	$LiNiO_2$	$LiMn_{1.5}Ni_{0.5}O_4$	$LiMnPO_4$
3	$LiNi_xCo_yMn_zO_2$	-	$LiNiPO_4$

However, there are multiple disadvantage of a layered structure cathode material over the other structure such as low capacity, expensive cost, and excessive charging or heating beyond 100° C leads to the breakdown of the cathode electrode as well as an electrolyte, resulting in the release of harmful gases [13]. Due to this, the spinel and olivine structure become more popular and then for practical application, both the structure are having multiple advantages such as good thermal stability, good cyclability, high rate cyclability due to which some more focused research work would be required to develop an efficient battery.

1.4 Material of Selection

1.4.1 Spinel Structure ($LiMn_2O_4$)

Spinel compounds have general formula AB_2O_4 (A=Li, B=Mn, Ni). This cathode structure allows the pathways in all the three dimensions for Li- intercalation. The most common spinel type cathode material is $LiMn_2O_4$ which is also one of the cathode materials for further investigation in present research work because of its high cycling stability, high thermal stability, high operating voltage, and cost-effective material [54-56].

1.4.1.1 Crystal Structure

Li-ions occupy the tetrahedral 8a site, Mn^{3+}/Mn^{4+} ions occupy the tetrahedral 16a site, and oxygen anions have the 32e site, which combined created the cubic-closed crystal structure in the $LiMn_2O_4$ with the fd3m space group [57-58]. This structure provides the three-dimensional (3D) conduction passage for Li-ions during the charging and discharging process. The edges of this crystal structure were shared by MnO_6 octahedral sites with two divergent corners of tetrahedral sites of LiO_4 as represented in figure 1.3 [59].

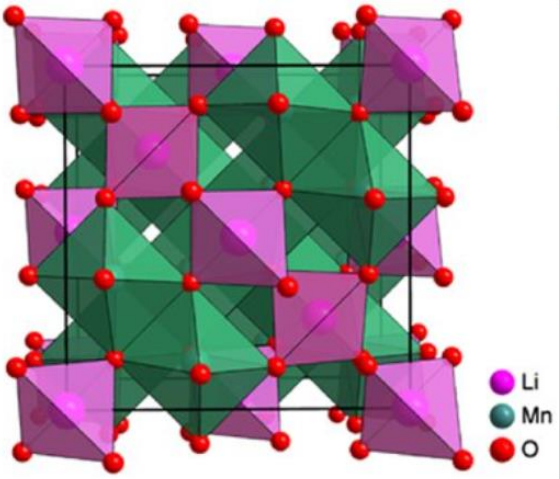

Figure 1.3 *Crystal Structure of $LiMn_2O_4$.*

However, the $LiMn_2O_4$ spinel structure has a Jahn-Teller effect, due to which the manganese ions show the asymmetric structure and also lead to the decrease in energy with high oscillate

and magnetic moment. During the reduction process, the Mn ions (Mn^{4+}) are converted into Mn^{3+}, resulting in the transformation of the cubic structure into a tetrahedral crystal structure with low symmetry, and also the conduction of electrons and the diffusion of Li-ions were also affected [58-59]. Furthermore, the dissolution of Mn ions may also cause dissolution and erosion on the material surface due to the acceleration of Mn^{2+} ions. Hence, $LiMn_2O_4$ has a significant attenuation on the discharge capacity due to the diffusion of Li-ions [59].

1.4.1.2 Properties of $LiMn_2O_4$

Among all the miscellaneous types of cathode materials, (Mn) manganese-based compounds would be some of the best objects of study. Spinel $LiMn_2O_4$ is one of the Mn-based cathodes that is appealing from an economic and environmental standpoint due to its abundance and non-toxicity [62-63]. It is known that $LiMn_2O_4$ has a three-dimensional spinel tunnel structure for lithium-ion migration[61]. In addition, this substance has high theoretical capacity, high operational voltage, cheap manufacturing cost, low toxicity, and a favorable voltage profile, making it appealing to the market as a commercial substance [63]. The main disadvantage of LMO is its electrochemical inactivity in the typical voltage range of 2.2–4.4 V *vs* Li+/Li since all Mn atoms are in the +4 valency. Since of this, lithium cannot be easily removed from $LiMn_2O_4$ because it is difficult to oxidize beyond Mn^{4+} in an octahedrally coordinated environment. [54-59]. Furthermore, during the initial charging process, a high turn-off voltage (~4.8 V vs. Li+/Li) is required to activate by removing Li_2O from the electrode active material.

1.4.2 Olivine Structure ($LiFePO_4$)

1.4.2.1 Crystal Structure

Among olivine type structure, the most commercialized and well-known compound is lithium iron phosphate, $LiFePO_4$ (LFP), which belongs to the lithium transition metal phosphates, $LiMPO_4$ (M=transition metal) [65]. In this structure, LFP belongs to the orthorhombic structure

with the *pnma* space group, in which PO_4 occupies the tetrahedral (4c) sites, while Li and Fe belong to the 4c and 4a sites, respectively as shown in figure 1.4 [65-66]. The unit cell contains a total of 28 atoms with four formulas $LiFePO_4$ [67].

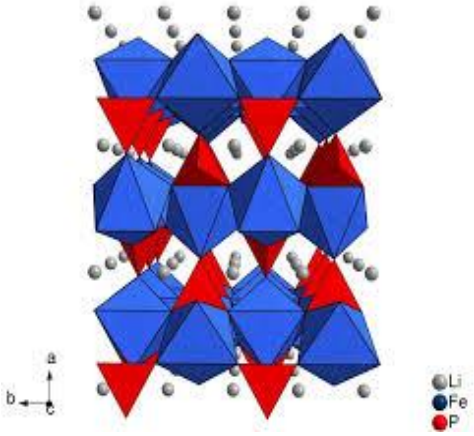

Figure 1.4 *Crystal structure of $LiFePO_4$.*

The strongest covalent bond between the phosphorous and oxygen structural unit helps to stabilize the LFP framework [65-68]. This strong bond also helps to increase the thermal stability of the compound above 400 ˚C as compared to other compounds.

1.4.2.2 Properties of $LiFePO_4$

Several researchers have drawn extensive attention over the past two decades to olivine-type structures for rechargeable lithium-ion batteries. LFP has gained increasing attention in the olivine family among various cathode materials due to its light weight, high theoretical capacity (170 mAh/g), structural stability, environmental friendliness, and a number of other factors [67-68]. However, there are certain drawbacks in pristine LFP as it has a wide band gap due to which the electronic conductivity is in the order of 10^{-9} to 10^{-11}S/cm at room temperature [69]. The presence of a wide band gap in the LFP leads toward the semiconductor material due to which the Li-ion diffusion coefficient also lies in the order of 10^{-14} cm^2/S [69]. So, to enhance its electronic conductivity various approaches has been used in the present research work.

1.5 Approaches for modification

Despite of all the above advantages, there are certain other parameters such as structural stability, and electrochemical performance that need to be enhanced for commercialization. The main parameter was electronic/ionic conductivity and the other was electrochemical properties that need more focus. There are various modification approaches for the enhancement in conductivity such as:

1. Addition of Conductive material for surface material
2. Carbon Coating
3. Morphological modification

1.5.1 Addition of Conductive material for surface modification

Li-ions and electrons are transported by the cathode material's electronic conductivity during the charging and discharging operation. Therefore, many researchers used various metal oxide coatings such as carbon, graphite, ZnO, Ag, SnO_2, TiO_2, Al-ZnO, CuO, etc., which help to increase the ionic conductivity and act as a protective layer on the surface of the active material electrode by direct link with the electrolyte. This coating also helps to reduce charge-transfer resistance and provides an improvement in structural stability [65-69].

1.5.2 Carbon Coating

Among various approaches, coating a carbon source is the most effective approach to improve electrochemical performance. The addition of carbon during the synthesis not only helps in increasing the conductivity, but also play an important role for reducing agent. As shown by previous research studies, the quality of carbon, coating of carbon, amount of carbon, thickness of the coating, and the nature of carbon are the major factors that help in the enhancement of electrochemical performances. There are multiple types of carbon source that are reported in the research work by previous studies such as graphite, MWCNT, CNT, Acetylene black,

sucrose and many more which help in the advancement of electrical conductivity and capacity of the electrode material.

1.5.3 Morphological Modification

In addition to doping/coating/substitution, the electrode material properties were also improved by changing the morphological of the cathode material. The pulverized sample of the electrode material should be controlled with the size variation of the porous microstructure, increase the surface area, and also the change in structure shape/ tailored structure during the compound synthesis. Therefore, all of these methods are other efficient avenues for advancement in electrochemical kinetics.

1.6 Research Objectives

Despite the rigorous research work on the cathode material, a comprehensive study of the change in physical and electrochemical studies is still lacking which prompted us to carry out the present research work on cathodes. Likewise, modeling and simulation work has been incorporated into the current research work, which could explain the effect of changing the internal control parameters for improving the electrochemical performance of the cathode material. Apart from that, a novel olivine spinel dual composite ($LiFePO_4$ - $LiMn_2O_4$) has also been studied. A hardware test bench was also developed to test the battery bank with a DC load, and a capacitor bank was directly interlinked in parallel with the coin-cell battery bank to further upgrade the electrical results. Hence, the objectives of the present investigation are as follows:

- ❖ Analytical modeling and simulation models were developed for investigating the internal parameters of different cathode materials.

- Synthesis and Physio-chemical characterization of alternate cathode material: Spinel structure cathode material: $LiMn_2O_4$, Olivine structure cathode material: $LiFePO_4$, and novel olivine - spinel ($LiFePO_4$ - $LiMn_2O_4$) dual composite.
- Improvement in the conductivity of cathode material, a new olivine-spinel type of alternate cathodes.
- Investigation of electrochemical properties of proposed alternative cathode materials.
- Development a hardware test bench for the study of Electrical characteristics using a data Acquisition system.

Chapter 2: Simulation and Experimental Characterization details

This chapter contains the Simulation and experimental details of material synthesis and characterization techniques used.

2.1 Computational and Modelling approach

Among many rechargeable types, Lithium-ion batteries (LIBs) give the best comprehensive performance. But due to the physical limitation of the electrode material, still the application of these batteries is limited [69-70]. The ionic and electronic conduction, as well as the transport phenomenon in the LIBs are the major focus area of research as the ionic and electronic conduction of LIBs are strongly related to the rate capability of the battery [71]. Hence, to explore the internal properties of the lithium-ion batteries (LIBs). It is essential to understand the governing laws and principle of rechargeable lithium-ion battery system. As all these rechargeable (secondary) batteries such as lead-acid, Ni-MH (Nickel metal hydride), Ni-Cd, and lithium-ion batteries are rechargeable batteries and designed based on the process of multiple charge and discharge phenomenon [69-71].

2.1.1 Basic Principles and Fundamentals of Lithium-ion batteries

Since, the lithium-ion batteries have a redox reaction inside the battery and it depends on the multiple parameters, which are mainly described into two categories:

- The kinetic parameters; the redox reaction in cell is controlled by kinetic parameters and this parameter help to control multiple function such as mass transport through an electrolyte due to migration/ diffusion, charge transport through the electrode, and the ohmic voltage drop due to variation in current [72].
- Thermodynamic/Equilibrium parameters; these parameters are based on the laws of thermodynamics and describe the system at equilibrium state (when no current is flowing). These parameters include entropy of reaction(S), Gibbs free energy (G), enthalpy of reaction (H) [73-75].

The entropy of reaction (S) helps to calculate the reversible energy gain/loss obtained from the electrochemical reactions that occur inside the LIBs. Gibb's free energy (G) defines the amount of chemical energy converted into electrical energy during the redox reaction of LIBs. The amount of energy entropy/enthalpy during the redox reaction inside the LIBs is known as enthalpy of reaction (H) [73-76]. These all the three terminologies are interlinked in the form of equation 2.1.

$$\Delta G = \Delta H - T \cdot \Delta S \tag{2.1}$$

Now, Gibb's energy helps to determine the fundamental values of Li^+ cell potential i.e. equilibrium Voltage (E˚) and the storage capacity as explained in equation 2.2.

$$E^\circ = -\frac{\Delta G^\circ}{n \cdot F} \tag{2.2}$$

Where n · F represents the total amount of electrical charge; F is Faraday constant= 96485 C mol^{-1}; n is the number of exchanged electrons during oxidation and reduction reaction. Therefore, Gibb's energy and electrical energy are directly proportional to each other. Furthermore, there are some other factors that affect the chemistry of LIB as discussed during model formulation.

2.1.2 Model Formulation

For a computational modeling of the LIBs, a pseudo two dimensional (P2D) model has been created with the help of Multiphysics Software. This P2D electrochemical thermal model of a LIB has been implemented through the use of the electrochemical domain [77]. This model is based on a few fundamentals of batteries as already explained in section 2.1.1 such as the transport mechanism, electrochemical kinetics, and thermodynamics, which helps to evaluate rate capability as well as characteristics of the battery [76-79]. A 2D Li-ion battery architecture has been designed for simulation. In this design, a cylindrical battery has been made up of a number of cylindrical cells where every cylindrical cell has to be connected in parallel by the

positive and negative terminal of the battery. Every cell was designed like a sandwich model of five different layers which was sequentially followed by a positive current collector (Aluminum), a positive electrode ($LiMn_2O_4$), separator (microporous polypropylene Celgard 2400), a negative electrode (Graphite/Carbon), and negative current collector (Copper) as shown in figure 2.1. This theoretical model is based on an experimentally validated model [79]. In this model two types of anode materials, graphite and carbon (MCMB) are used with the spinel type cathode material ($LiMn_2O_4$) to obtain the battery characteristic where as in olivine type, the hard carbon has been used as an anode material. The model is formulated to evaluate the spinel and olivine cathode material performance separately during the charging and discharging process.

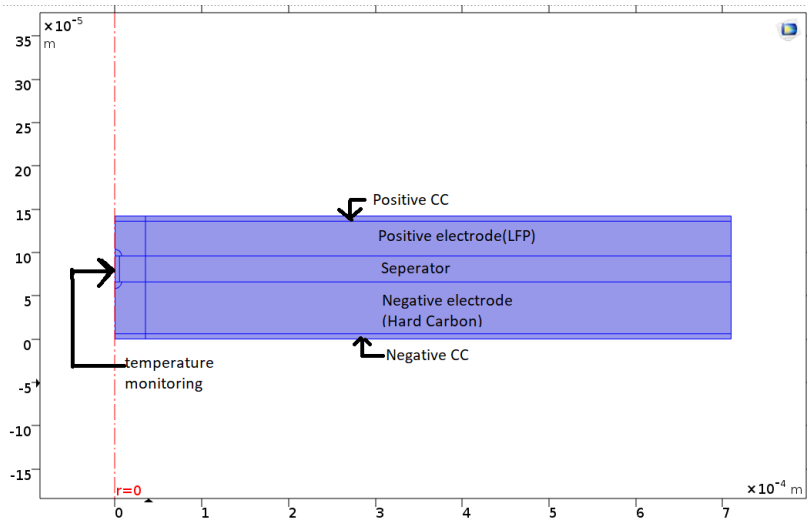

Figure 2.1 *Geometry of Lithium-ion Battery model.*

For model formulation, various input parameters such as geometry design parameters for model layout, both anode and cathode material properties, ambient operating temperature with different boundary conditions and load current have been considered. Table 2.1 contains a list of these input parameters.

Table 2.1 *Measured and model input parameter for the LIBs.*

Name	Units/Equation	Description of Name
rp_neg	2.50 x e^{-6}[m]	negative electrode particle radius

rp_pos	1.70 x e^{-6}[m]	Positive electrode particle radius
epss_pos 1-epsl_pos	-0.170	Positive electrode solid phase volume fraction
epsl_pos	0.401	Positive electrode electrolyte phase volume fraction
brugl_pos	2.97	Positive electrode bruggeman coefficient for tortuosity
epss_neg 1-epsl_neg	-0.1712	Negative electrode solid phase volume fraction
epsl_neg	0.4454	Negative electrode electrolyte phase volume fraction
epsl_sep	0.371	Separator electrolyte phase volume fraction
brugl_sep	3.151	Separator bruggeman coefficient for tortuosity
k_neg	2.1 x e^{-11}[m/s]	Negative electrode reaction rate coefficient
k_pos	5.1 x e^{-10}[m/s]	Positive electrode reaction rate coefficient
cs0_neg	2204	Initial state-of-charge negative electrode
cs0_pos	20925	Initial state-of-charge positive electrode
cl_0	1200	Initial electrolyte salt concentration
a	7.51	C-factor
i_1C	12	1C discharge current
i_load	i_1C x a	Charge/discharge current
L_neg	55.1 x e^{-6}[m]	Negative electrode length
L_sep	70.1 x e^{-6}[m]	Separator length
L_pos	55.1 x e^{-6}[m]	Positive electrode length
d_can	0.251[mm]	Battery canister thickness
r_batt	9[mm]	Battery radius
h_batt	65[mm]	Battery height
r_mandrel	2[mm]	Mandrel radius
L_neg_cc	7[um]	The thickness of negative current collector
L_pos_cc	10[um]	The thickness of positive current collector thickness
L_batt	L_neg+L_neg_cc+L_sep+L_pos+L_pos_cc	The thickness of Cell
kT_pos	1.58[W/(m*K)]	The thermal conductivity of positive electrode
kT_neg	1.04[W/(m*K)]	The thermal conductivity of negative electrode
kT_pos_cc	170[W/(m*K)]	The thermal conductivity of Positive current collector

kT_neg_cc	398[W/(m*K)]	The thermal conductivity of Negative current collector
kT_sep	0.345[W/(m*K)]	The thermal conductivity of Separator
rho_pos	2328.51[kg/m^3]	Density of Positive electrode
rho_neg	1347.32[kg/m^3]	Density of Negative electrode
rho_pos_cc	2770[kg/m^3]	Density of Positive current collector
rho_neg_cc	8933[kg/m^3]	Density of Negative current collector
rho_sep	1008.97[kg/m^3]	Density of Separator
Cp_pos	1269.211[J/(kg*K)]	Heat Capacity of positive electrode
Cp_neg	1437.44[J/(kg*K)]	Heat Capacity of negative electrode
Cp_pos_cc	875[J/(kg*K)]	Heat Capacity of positive current collector
Cp_neg_cc	385[J/(kg*K)]	Heat Capacity of negative current collector
Cp_sep	1978.156[J/(kg*K)]	Separator heat capacity
kT_batt_ang	(kT_pos*L_pos+kT_neg*L_neg+kT_pos_cc*L_pos_cc+kT_neg_cc*L_neg_cc+kT_sep*L_sep)/L_batt	Battery thermal conductivity, angular
kT_batt_r	L_batt/(L_pos/kT_pos+L_neg/kT_neg+L_pos_cc/kT_pos_cc+L_neg_cc/kT_neg_cc+L_sep/kT_sep)	Battery thermal conductivity, radial
rho_batt	(rho_pos*L_pos+rho_neg*L_neg+rho_pos_cc*L_pos_cc+rho_neg_cc*L_neg_cc+rho_sep*L_sep)/L_batt	Battery density
Cp_batt	(Cp_pos*L_pos+Cp_neg*L_neg+Cp_pos_cc*L_pos_cc+Cp_neg_cc*L_neg_cc+Cp_sep*L_sep)/L_batt	Battery heat capacity
Cycle_time	600[s]	Cycle time
T_inlet ""	298.125[K]	Inlet temperature
T_init	T_inlet	Initial temperature
h_connector	3[mm]	connector height
r_connector	3[mm]	connector radius
s_inlet	2 x r_batt	Length of inlet flow region
s_matrix	3 x r_batt	Battery-battery distance in matrix
v_in	0.12[m/s]	Inlet velocity
t	0	Time parameter in the initialization study step

Some other influential input parameters such as the stoichiometry of the model for both positive

and negative electrodes, electrodes charge transfer coefficient, electrolyte coefficient, Bruggeman coefficient are taken from the data available in the literature [80-84]. In this proposed theoretical model, the Li-ions transport phenomenon is based on parameters such as solid-state potential, electrolyte concentration, solid-state concentration within the electrode, and electrolyte potential within the separator. These domains are further explained with the help of mathematical modeling presented in the following section.

2.1.3 Electrochemical-Thermal Mathematical Modelling

The proposed electrochemical-thermal model has some governing equations and boundary conditions which help to evaluate the certain variables for solving the P2D model such as electrochemical kinetics, electric charge conservation, energy conservation, and mass conservation [85-88]. For the simulation of solid-state lithium-ion battery and analyzing its chemistry domain, certain electrochemical kinetics equations were carried out with the help of the Butler-Volmer governing equation [85-86], which is used to describe the lithium concentration as well as charge distribution on the anode and cathode electrodes and electrolyte phase as shown in equation 2.3 [86-91].

$$j^{li} = a_s\, i_0 \left[exp\left(\frac{\alpha_a F}{RT}\eta\right) - \exp\left(\frac{-\alpha_c F}{RT}\eta\right) \right] \tag{2.3}$$

Where j^{li} refers to a reaction current density, a_s is the reaction surface area [88]. Further, the electrodes having a solid active phase and electrolyte as a liquid phase which together creates an interfacial area and known as reaction surface area (a_s) and it is shown with equation 2.4 [91].

$$a_s = \frac{3\varepsilon_s}{r_p} = \frac{(1-\varepsilon_e-\varepsilon_f)}{r_p} \tag{2.4}$$

where ε_s is the active material volume fraction, ε_e is the electrode porosity, r_p is the radius of the active material and ε_f is the fillers of the active material [90]. The relation of the lithium concentration for the potential of both the electrodes is defined with the help of current density (i_o) and it is expressed as equation 2.5 [90].

$$i_0 = k_i(c_e)^{\alpha_a}\ (C_{surf,max} - \ C_{surf,e}\ )^{\alpha_a}\left(c_{surf,e}\right)^{\alpha_c} \quad (2.5)$$

Here, k_i denoted the temperature-dependent reaction rate, α_a, α_c is the symmetry factor of anode and cathode, C_e, is lithium concentration in the electrolyte phase and $C_{surf,\ max}$, $C_{surf,e}$ is the lithium concentration maximum on the surface and electrolyte [90-91].

The electronic charge balance has to be maintained with the equivalence of Li-ions during lithiation and de-lithiation and electron flow in the charging and discharging process. The reaction current density can be expressed as shown in equation 2.6 because the quantity of potential in the solid phase must depend on electrode conductivity [92-94].

$$\nabla(\sigma^{eff}\nabla\phi_s) = j^{li} \quad (2.6)$$

Where φ_s is the potential in the solid phase [27-28]. Similarly, Equation 2.7 explains that the potential in the liquid electrolyte depends on the concentration of the lithium ions and the current density [89].

$$\nabla(\sigma^{eff}\nabla\phi_e) + \nabla\left(k_D^{eff}\nabla lnC_e\right) + j^{li} = 0 \quad (2.7)$$

Where σ^{eff} is the effective conductivity and k_D^{eff} represents the effective diffusional conductivity of the species, and φ_e is the potential in the electrolyte phase [89-91]. For maintaining the mass conservation in the solid phase, it is assumed that the particle size of the electrode material in the model has to be identical and lithium-ion distribution can be explained with the help of Fick's law of concentration gradient as given in equation 2.8 [91]:

$$\frac{\partial(C_s)}{\partial x} = \frac{D_s}{r^2}\frac{\partial}{\partial r}\left(r^2\frac{\partial C_s}{\partial r}\right) \quad (2.8)$$

Where D_s is the diffusion coefficient in the solid phase, C_s are lithium concentration in the solid phase, r is the radius of the material [80-89]. In this electrochemical simulation analysis, the domain equations help to implement the chemical transport equations for the reactant and product species [89]. This further demonstrates the electrochemical reactivity and the transport property of the battery [91-95]. However, this model was formulated with all the domain

equations, which have been shown in the meshed structure of solid-state cylindrical type lithium-ion battery (LIB).

2.1.4 Model Meshed Structure

A 2D cylindrical Lithium-ion battery simulation model has been designed on a COMSOL Multi-physics 5.3a version to evaluate the battery performance in terms of rate capability. The model formulation parameters are explained in the above sections. In this model, various characteristics are demonstrated with the help of mathematical modeling. For example, the kinetics of mass transport in the LIBs, the lithium-ion diffusion is demonstrated with the help of Faraday's equation and the amount of energy and power in the battery is calculated using Ragone plot [90]. The simulation results were generated with the help of the proposed 2D model and the experimental data were validated from the published literature [91-94].

Initially, the geometry of the model was designed considering different components such as porous electrodes, electrolytes, and current collectors. Then, the various governing equations were estimated for the 2D structure of the model for a better understanding of the ionic/ electronic conductivity phenomenon and mass transfer mechanism in a battery [94]. After including the all-necessary operational parameters, a meshed structure of the 2D model is obtained and this structure is analyzed in all three directions with ambient temperature and different boundary conditions [90-95].

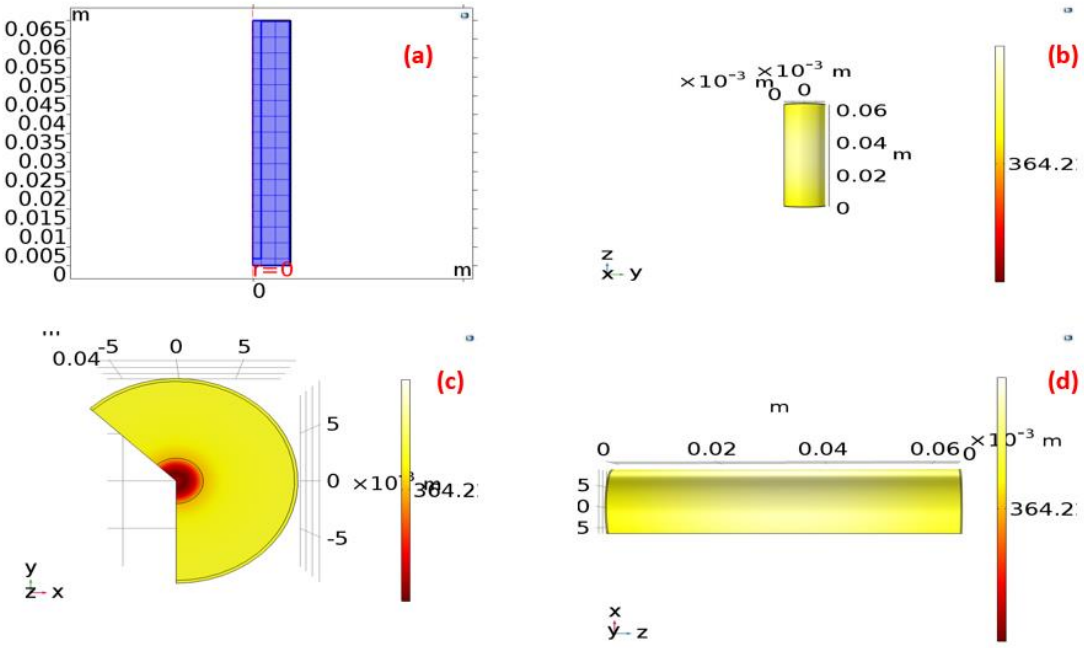

Figure.2.2: *(a) Meshed geometry of cylindrical battery, 2D cylindrical battery view along (b) the YZ axis, (c) the XY axis, and (d) the ZX axis, respectively.*

This meshed structure is mapped with the help of a singular matrix as shown in figure 2.2 (a). Further, evaluation has been carried out in the form of a 2D revolution model along with the combination of XY, YZ, and ZX axis as shown in figure 2.2 (b), (c), (d) respectively. Hence, the meshed structure indicates a blue dotted line which represents the triangular mapped domain on a model geometry with a certain boundary condition at the corner of the battery. After setting up the mathematical geometry and meshing domain, the result study has been performed with the help of different parametric and control functions.

2.2 Experimental: Synthesis Techniques

The synthesis of spinel type ($LiMn_2O_4$), olivine type ($LiFePO_4$) and Olivine-Spinel Dual Composite ($LiFePO_4$ - $LiMn_2O_4$) have been explained in this section. The synthesis of cathode material has been performed using two different methods: Sol-gel method and Solid-solution method.

2.2.1 Sol-gel Method

Sol-gel is also known as wet chemical technique. In this technique, the metal oxides and other composition compounds were synthesized using salt precursors in a solvent as well as chelating agent was used as a catalyst to increase the reaction rate of the synthesis. In liquid, the solid particles of sol act as a stable colloidal solution that helps the precursors for binding of discrete particles with their pores and this complete process is known as gelation. Further, this liquid gel was dried at certain temperature for the formation of Xerogel. This Xerogel was heated at an elevated temperature for densification of final product. Figure 2.3 explains the general synthesis procedure for Sol-gel technique.

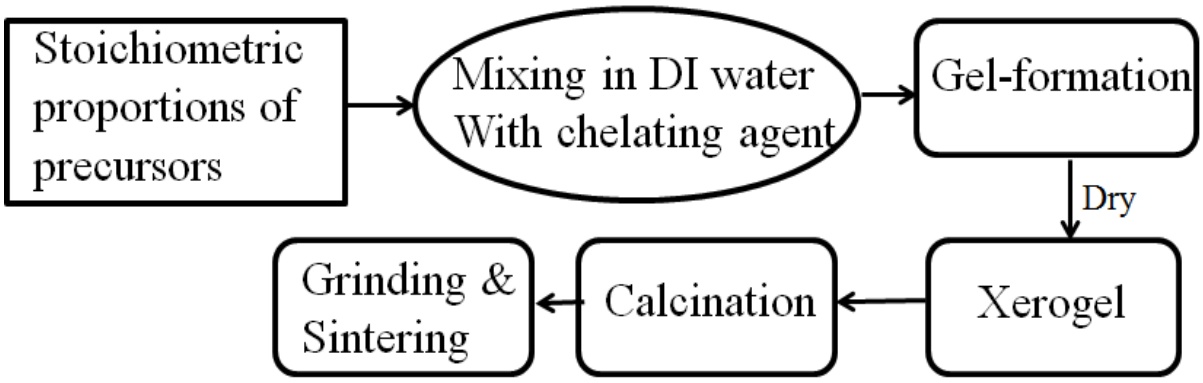

Figure 2.3. *Flow chart for the synthesis of cathode material using Sol-gel technique.*

2.2.1.1 Synthesis of Spinel type ($LiMn_2O_4$) cathode material

The Spinel $LiMn_2O_4$ sample was synthesized using Lithium (Li) and Manganese (Mn) based reagents in a 1:2 stoichiometric ratio. Lithium acetate, Manganese acetate tetrahydrate, and citric acid were employed as precursors in this sol-gel method. All of the reagents were distributed in deionized water and constantly stirred. After continuous stirring, the PH of the sample is maintained. The PH value of the resultant sample was kept between 6 and 7 after rigorous stirring. The resultant mixture was then stirred continuously at 350 rpm at 70 ˚C until it was transformed into a translucent gel. Now, the acquired gel was heated at 180 ˚C in the vacuum oven to acquire a powdered sample. This powdered sample was subsequently

calcinated in two steps: firstly, the decomposition of the compound has been calcinated at 350 ˚C for 8 hrs. and secondly, the final calcination for phase formation has been done at 775 ˚C for 20 hrs. in the muffle furnace. After cooling, the calcined sample was re-grounded, crushed into a mortar pestle. Here, he $LiMn_2O_4$ sample is abbreviated as LMO.

2.2.1.2 Synthesis of Olivine type ($LiFePO_4$)

The Synthesis of olivine type ($LiFePO_4$) cathode material was carried out using different salt precursors at stoichiometric amount such as $LiOH.H_2O$, $FeC_2O_4.2H_2O$ and $H_9N_2O_4P$. Additionally, citric acid served as a chelating agent. All the salt precursors are mixed with a deionized water and put on a magnetic stirrer for continuous stirring at a 70-80 ˚C temperature. After dissolving all the precursors, a citric acid was poured slowly into the mixture and pH of the solution was also maintained between 6-7 using ammonium hydroxide. After continuous stirring, a greenish transparent gel was obtained. This gel was dried in a vacuum oven for the formation of Xerogel. After obtaining the dried powder sample, a decomposition of cathode material was performed in inert atmosphere for 8-10 hour at 350 ˚C. Further, for final calcination, the dried powder was again heated at 750 ˚C for 12 hours in inert atmosphere. Thus, final product (LiFePO4) was re-grounded and obtained for further characterization as abbreviated as ‘LFP’.

2.2.2 Solid-Solution Technique

This method is the most explored method for synthesizing the metal and alloy powder. This method helps to enhance the chemical reactivity of the mixture using ball-milling technique. This process also helps in the improvement of morphological properties of the cathode material incorporating the smallest particle size with high specific area and this process helps to drive the reaction at low temperatures. During this process, all the salt precursors are mixing properly inside the stainless steel jar on a high rpm with a certain duration using ball milling machine.

2.2.2.1 Synthesis of Novel Dual Composite ($LiFePO_4$- $LiMn_2O_4$)

The composites of both the olivine-$LiFePO_4$ (LFP) and spinel-$LiMn_2O_4$ (LMO) were prepared separately using the sol-gel method. First, spinel $LiMn_2O_4$ was prepared separately using Li-Mn metal ions in a 1:2 ratio and using citric acid as a chelating agent. Aqueous ammonia was used to keep the compounds' pH between 6-7 while dispersing them all in deionized water and stirring continuously. After vigorous stirring, gelation was started, then it was heated for 5 hours at 120°C in a vacuum oven for gel-to-powder conversion. Then, this powder was further calcined at 775°C for 20 hours in a muffle furnace. Similarly, the olivine $LiFePO_4$ was prepared using the sol-gel route, using various precursors such as lithium acetate, iron hydroxide, and ammonium phosphate in stoichiometric amounts. This produced compound was decomposed and calcined in the inert atmosphere at 750°C for 12 hours. Both composites were made in powder form using different types of precursors.

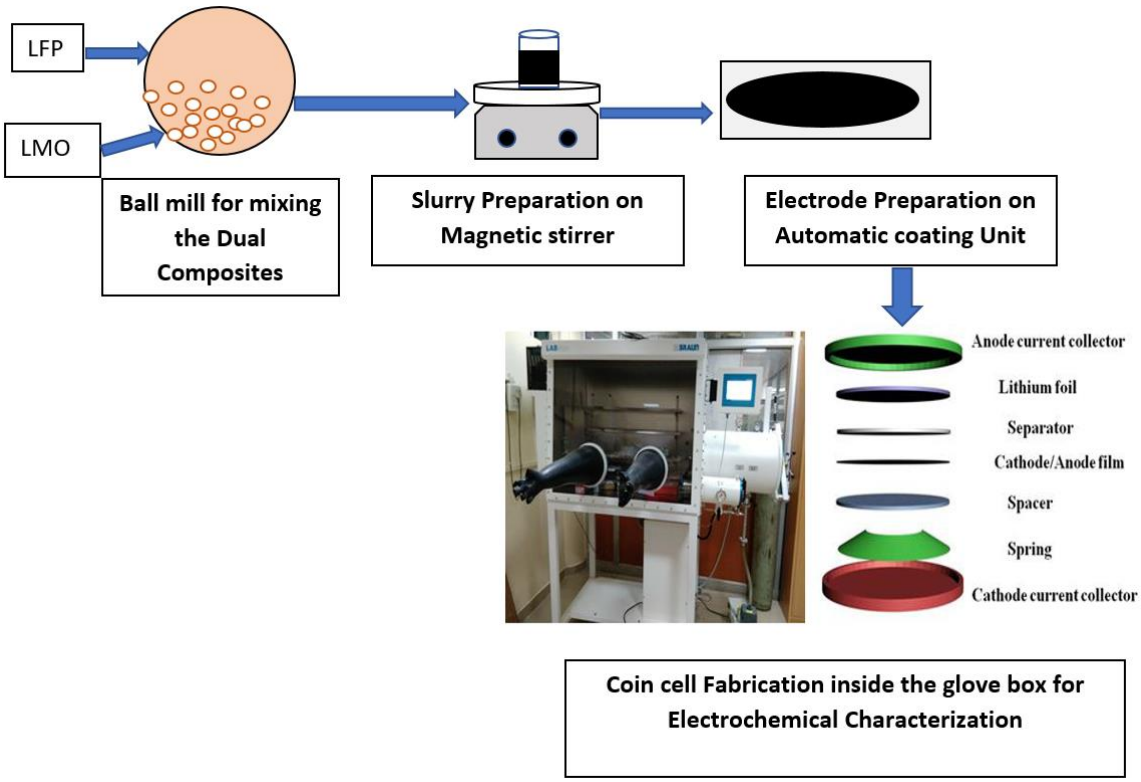

Figure 2.4. *Synthesis of dual composite using Solid-Solution technique.*

The dual composites were prepared by mixing the two active ingredients in a different mass ratio using a ball mill, forming a single monolithic compound, abbreviated as 1LFP/1LMO, 3LFP/1LMO, and 1LFP/3LMO, referring to different mass ratios 1:1, 3:1 and 1:3 with olivine and spinel structure to form the intercalation cathode as shown in figure 2.4.

2.3 Characterization Techniques Used

In order to investigate the properties of synthesized cathode material, a different characterization technique has been chosen to extort the physical, structural, morphological, thermal, electrical and electrochemical analysis of the synthesized samples. This section provides ~~us~~ the brief overview about the characterization instruments and techniques used.

2.3.1 Structural and Morphological Characterization

2.3.1.1 X-Ray Diffraction (XRD)

Utilizing an X-ray diffractometer (XRD) made by RIGAKU, CuK1 radiation with a wavelength of 1.540, and a Ni filter, the synthesized samples of various cathode materials were characterized and evaluated for a computable and quantifiable analysis of the crystal structure and determination of the phase formation of the compound.. The wide range scan of diffraction angle, 10^0 to 90^0 has been measured with a step size, 0.02. X'pert high score software has been used for the analysis of lattice constants and other structural parameters. The crystallite size of the synthesized samples is estimated using Scherrer's formula as shown in equation 2.8;

$$d = k\lambda/\beta Cos(\theta) \tag{2.8}$$

where k is shape factor (0.89), λ is the wavelength of X-rays (1.540 Å), β is the full-width half maximum (FWHM in radian), θ is the Bragg diffraction angle (peak position).

2.3.1.2 Scanning Electron Microscope (SEM)

The HITACHI make S-3700N scanning electron microscope (SEM) was used to characterize the morphological examination of the produced compound at an operating voltage range up to 15 kV. The determination of elemental composition has been carried with attached EDAX attachment in the HITACHI make S-3700N equipment. The SEM images were taken under secondary electron (SE) mode. The “ImageJ software” has been used for calculation of the average grain size of all the synthesized samples.

2.3.1.3 Transmission Electron Microscope (TEM)

A TEM was used to examine the morphological of the synthesized sample in which the thickness of the coating, crystallite/ particle shape/size and the crystalline nature in terms of the fringe width can be determined. FEI's TWIN TF30 model has been utilized to analyze the morphology and crystallinity of the produced materials. Suspension of synthesized cathode materials has been made and thin film of synthesized material is made over carbon-coated copper grids (CF200-Cu) and TEM measurements were performed at operated voltage of 300 kV.

2.3.2 Vibrational and Thermal Characterization

The Fourier transform infrared spectroscopy (FTIR) reveals the functional group of the organic compound and also shows the flow of cations in the octahedral interstices with the help of vibrational modes. For FTIR characterization, a PERKIN ELMER make C91158 spectrometer was used in the wide range of Wavenumbers, 4500-400 cm^{-1} using the KBr as binder. FTIR data has been recorded in the transmission mode as shown in figure 2.5.

Figure 2.5 *FTIR instrument for Vibration Analysis.*

Thermogravimetric Analysis (TGA) test was performed to analyze the thermal properties of the synthesized sample and also obtain the decomposition and calcination temperature at a variable atmosphere. In this, EXSTAR make TGA, SII 6300A model has been used for mass loss *vs*. temperature study and data was collected with different atmospheric conditions as per the requirement of sample as shown in figure 2.6. The flow rate of gases were 200 ml/min with a wide heating temperature range of 30-900 ˚C at a scan rate of 10 ˚K/minute using Pt crucible.

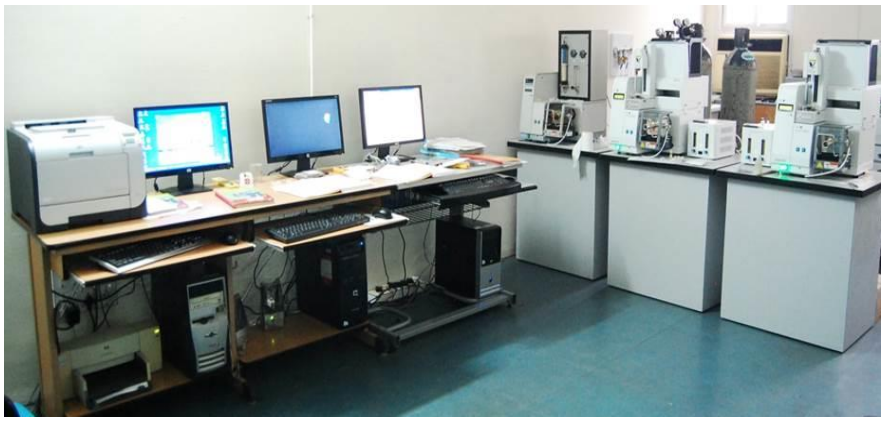

Figure 2.6. *TGA instrument for thermal analysis.*

2.3.3 Electrical Characterization

The electrical conductivity refers to the flow of current across the conductive material, when external electric field is applied across it. The DC ionic conductivity, σ_{DC} (in Scm^{-1}) was calculated with the help of standard equation 2.9 and I-V curve was also plotted on the source measurement instrument as shown in figure 2.7.

$$\sigma = \frac{1}{R}\left(\frac{L}{A}\right) \tag{2.9}$$

Where L in cm is the thickness of the pellet. A in cm^2 is the cross-sectional area of the pellet and R in Ω (ohms) is the resistance of the sample.

Figure 2.7. *Source Measurement Unit (SMU) for electrical conductivity Measurement.*

For investing the electrical conductivity of the synthesized sample, a pellet was made by mixing a 2.5% PVC (polyvinyl alcohol), and then it was annealed at 250 ˚C for 3hr. After drying a pellet, silver paste was applied at both sides of the surface to make the pellet conductive and then dried at 150 ˚C for half an hour. Now, the dried pellet was placed on a two-point probe setup to measure the electronic conductivity using the KEITHLEY 6517A electrometer at a high resistance, variable temperature up to 25-300 ˚C as well as with a variable frequency range of 20 Hz to 1 MHz.

Further, the ionic conductivity i.e. σ was calculated using an activation Energy (E_a) in eV with the help of Arrhenius equation 2.10:

$$\sigma = \sigma_o exp\left(\frac{-E_a}{K_B\, T}\right) \tag{2.10}$$

Where K_B is the Boltzmann constant in $J.K^{-1}$ and T is the temperature in Kelvin (K).

2.3.4 Electrochemical Characterization

For analyzing the electrochemical properties of the synthesized material, the coin-cell battery has been fabricated for testing the performance of material as discussed briefly in this section.

2.3.4.1 Electrode and Coin-cell fabrication

For electrochemical analysis, all the synthesized samples of spinel-LMO, olivine- LFP, and novel dual composite (LMO-LFP) were used to fabricate a half coin cell assembly. In this, the synthesized compound's working electrodes were created by dispersing the 72 weight percent active component, 12 weight percent conductive carbon (Super P), and 16 weight percent binder (Polyvinylidene difluoride, PVDF) in solvent N-methyl-2-pyrrolidinone (NMP). Thus, these were all mixed together for 12 hours to create a thick, homogeneous slurry. Using a Gelon make automatic coating unit, this slurry was then uniformly coated onto an aluminum (Al) foil current collector. After this, the slurry was kept at 120°C for heating overnight in an air medium. After evaporating all the liquid content from the slurry, the circular electrode of 16 mm diameter was punched out and the effective mass loading was measured over the aluminum sheet. These electrodes were again placed in a vacuum oven to evaporate the moisture content before being transferred to a glove box workstation (O_2 and H_2O levels of less than 0.5 ppm). As an activator for the movement of lithium ions, $LiPF_6$ salt was dissolved in ethylene carbonate (EC) and dimethyl carbonate (DMC) at a volume ratio of 1:1 in a liquid electrolyte. A Celgard 2400 was used as a separator to prevent a short circuit between both electrodes. After assembling the coin cell, a cell was placed outside the glove box to stabilize the open-circuit voltage (Voc) for 24 hours. Once Voc became stable, electrochemical characterization was performed on Biologic's make potentiostat/ Galvanostat model VMP3 as shown in figure 2.8.

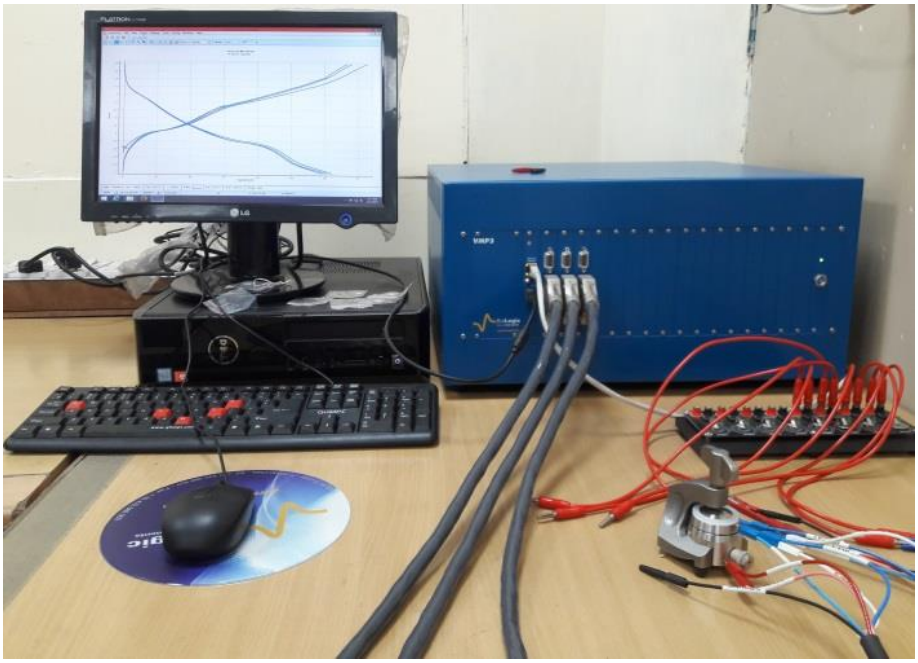

Figure 2.8 *Multichannel Biologic's make VMP3 potentiostat/ galvanostat set up used for electrochemical analysis.*

2.3.4.2 Cyclic Voltammetry (CV)

Cyclic voltammetry (CV) is a most common method for electrochemical measurement because of its high information content. During the CV test, a linear potential is applied across the cell with a constant scan rate for recording the data in the form of current. At a scan rate of 0.05 mVs^{-1}, the voltage range of 2.0-4.2V has been used to plot the current-voltage curve. This curve explores the information about the kinetics and thermodynamics of the electrode reaction as well as diffusion-controlled process in which the electro-active species insert inside the electrode.

2.3.4.3 Electrochemical Impedance Spectroscopy (EIS)

With the x-axis designating the "real part" and the y-axis designating the imaginary (complex) component, the EIS approach represents the plot in terms of frequency domain. This graph is usually a representation of the Nyquist plot, in which the high-frequency domain is represented by the semicircle, and the low-frequency domain by the straight line. The Warburg impedance

(Z_w), which controls the Li^+ diffusion of the active electrode material, is often represented by the inclined line in the low-frequency domain while the semi-circle intercepts on the real axis correspond to the charge transfer resistance (R_s) in the high frequency domain.

Using an AC voltage with an amplitude of 5 mV, the EIS data was plotted for each synthesized sample over the frequency range of 20 Hz to 1 MHz. Additionally, equation 2.11 has been used to determine the diffusion coefficient of the li-ions for all the synthesized material.

$$D = \frac{R^2T^2}{2A^2n^4F^4C^2\sigma_W^2} \quad (2.11)$$

Where, C is the lithium-ion concentration (7.69 x 10^{-3} mol cm^{-3}), F is the Faraday constant (96486 C mol^{-1}), n is number of electrons involved in the redox process (assumed n=1 in this case), T is absolute temperature (K), A is electrode area (cm^2), R is gas constant (8.314 J mol^{-1} K^{-1}), D is Li-ion diffusion coefficient (cm^2/s), and σ_w is the Warburg coefficient which is related to Z' by following equation 2.12.

$$Z' = R_{ct} + R_s + \sigma_w \omega^{-0.5} \quad (2.12)$$

Where ω is the angular frequency. Based on the above Eq. (2.12), Warburg coefficient, σ_w was calculated. As a result, Equation (2.11) has been utilized to compute the Li-ion diffusion coefficients for each sample using predicted Warburg coefficients.

2.3.4.4 Galvanostatic Charge and Discharge (GCD)

In GCD, a half coin cell assembly was used for test the cathode material in which Li-metal act as a reference electrode due to the inherent stability of Li-metal. This lithium metal chip always utilized as a counter electrode and provide a Li-source in large quantity for a cell. For GCD, a constant current is applied across the cell and the potential across the cathode material was measured. Further, a synthesized cathode material was used to fabricate CR-2032 half coin cell to characterize the material properties such as discharge capacity, rate capability and many more using a VMP3 program-controlled model by Biologic make.

Chapter 3: Multiscale Modelling and Simulation of Cathodes Materials for the enhancement of Electrical, Thermal, and Electrochemical performance of Lithium-ion batteries.

This chapter includes the computational modelling of both spinel-based $LiMn_2O_4$ and olivine-based $LiFePO_4$ cathode material. The computational results have been simulated through which, $LiMn_2O_4$ cathode material enhances the electrochemical performance after controlling the internal impedance parameters and also helps to evaluate the thermal and electrical performance of a rechargeable lithium-ion battery. Similarly, the olivine-based $LiFePO_4$ material has also been evaluated through Multiscale modelling and it provides a detailed evaluation of electrochemical, thermal, and electrical results for the Lithium-ion battery.

3.1 Introduction

As discussed in section 1.6, chapter 1 for the theoretical advancement of cathode material, a computational analysis has been performed to validate the experimental results and also anticipate performance, develop and support experiments to optimize the material characteristics and geometries, as well as assess safety and durability in a holistic manner. In this chapter, a 1-D electrochemical model has been modeled and simulated for the evaluation of the electrochemical performance of the spinel-type $LiMn_2O_4$ (LMO) battery. In this model, five various control parameters have been used to analyze the internal performance of the battery for Electrochemical Impedance Spectroscopy (EIS) characterization. In addition, for a better understanding of LIB's electrochemical behavior, a comparative study has been conducted in which experimental and simulated EIS characterization are explored. In this Nyquist spectra, the global least square method was used to simulate and analyzed five different control parameters. The charge and discharge characterization at various C-rates has also been simulated in a 1-D electrochemical model for assessing the performance of the LMO cathode at various C-rates. Moreover, the electrical and thermal analysis of the battery pack at various temperatures has been tested on a 3-D model for evaluation of the safety performance.

Further, an olivine type of cathode material, Lithium Iron Phosphate (LFP) battery is used for computational analysis. A 3-D structure model is designed with the help of three basic parameters such as electrochemistry kinetics, transport phenomena, and thermodynamics. The proposed 3-D structure of a battery is divided as a positive electrode, a negative electrode, electrolyte, separator and the current collector (CC). This construction helps to solve the electrolyte concentration within the porous electrodes and electrolyte potential within the separator.

In this P2D model for lithium-ion battery formulation, different types of characterization techniques have been performed on Li-ion battery. First, the electrochemical characterization techniques have been performed with the help of the electroanalysis method as explained in chapter 2 (section 2.1.2) [95-96]. Electrochemical techniques are further elaborated in two methods i.e. cyclic voltammetry (CV) and Electrochemical impedance spectroscopy (EIS) as further explained in next section. In this process, the model used contains a 2-D axisymmetric domain surrounded by infinite elements, that comprises the P2D electrochemical structure [97]. Secondly, the electrical and thermal characterization was also performed to evaluate the LFP cathode material properties at various temperatures as elaborate in the next section.

3.2 Results and Discussion

3.2.1 Result of Spinel type cathode: $LiMn_2O_4$

3.2.1.1 Electrochemical Analysis

A. Cyclic Voltammetry (CV)

A cyclic voltammetry (CV) curve has been plotted which helps to determine the electrochemical reactivity and transport properties of a lithium-ion battery [98]. In this CV test, the potential varies linearly as a function of time is applied to the working electrodes [99]. Figure. 3.1 shows the recorded cyclic voltammetry curve which determines the relation between the transport chemical species. It also represents the diffusion of lithium ions in the battery and the electrode kinetics [98-99]. The results are plotted at the variable potential range, in which parametric sweep has been used to record the graph at different scan-rates.

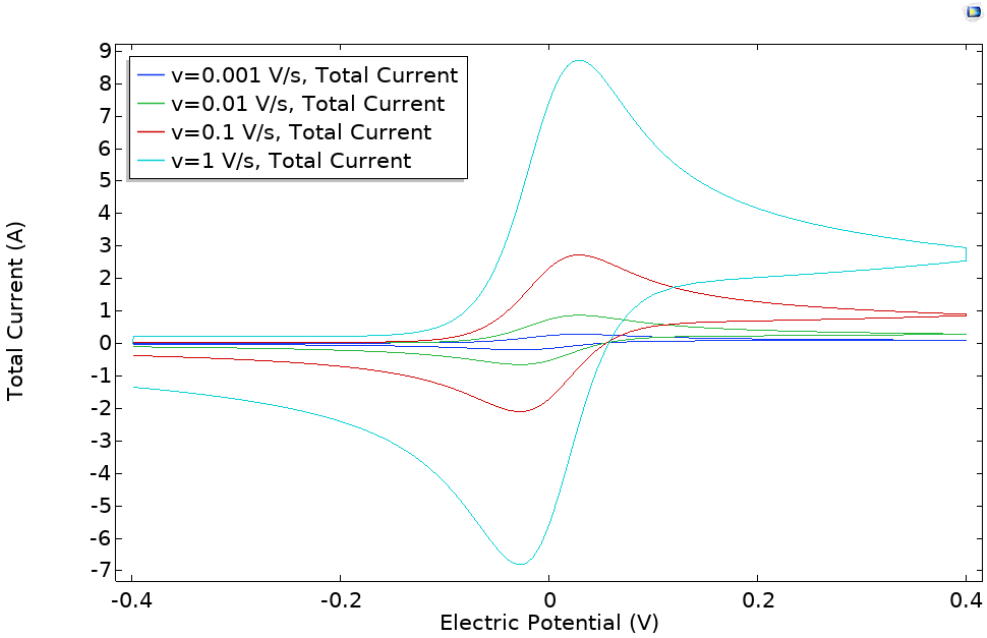

Figure 3.1. Cyclic-voltammetry curve.

The CV result suggests that at a lower scan rate of 0.001 V/s, because of the very low potential, no oxidation reaction occurs, and as a result, the current is very negligible. Additionally, it demonstrates that as the potential rises, the oxidation reaction quickens and the current also begins to rise. Once the reactant has been consumed by the oxidation reaction at the electrode surface, the current is subsequently constrained by the rate of transport at the working electrode. Therefore, the highest peak current of 8Amp has been observed at a higher scan rate of 1 v/s after the peak of voltammetric current. It starts falling independent of the potential rate. This region of the CV curve denotes the diffusion-controlled or transport-controlled region [99-100]. Similarly, the other characteristics are simulated and analyzed to determine the EIS, charge and discharge characteristics of the LMO cathode material.

B. Electrochemical Impedance Spectroscopy (EIS)

In these Nyquist spectra, a real and imaginary component was obtained from EIS, which explores the mass transport properties, capacitive as well as kinetic properties of the battery [99-100]. The Nyquist plot was plotted between the real and imaginary components with 20 mV AC pulse magnitude for obtaining the experimental and simulated impedance spectra in

the positive LMO electrode as shown in figure 3.2. In this plot, the “ref” is represented as the reference point probe that was located at the middle of the separator to retrieve the potential [100-101]. To obtain the simulated data, the optimization has been done using the global least square method [102]. This method has been used to minimize the error between simulated and measured LMO impedance. There has been a certain variable parameter that has to control with a cell voltage of 3.10V. Table 3.1 contained a list of the control parameters.

Table 3.1 *Control Parameters with a cell Voltage of 3.10V.*

Control Parameters	**Initial Value**	**Boundary Condition**
Exchange Current Density	1 Am^{-2}	Lower: 1 Am^{-2} Upper: 6 Am^{-2}
Double Layer Capacitance (DLC)	2.393 $X10^{-1}$ Fm^{-2}	Lower: 1 x 10^{-1} Fm^{-2} Upper: 9 x 10^{-1} Fm^{-2}
Film Resistance	2.848 $X10^{-3}\Omega m^2$	Lower: 1 x $10^{6}\Omega m^2$ Upper: 5 x $10^{-3}\Omega m^2$
Volume DLC Electronic Conductor	2.577 X 10^{5} Fm^{-3}	Lower: 1 x 10^{5} Fm^{-3} Upper: 1 x 10^{6} Fm^{-3}

After the selection of control parameters with narrow bound intervals, the optimization accuracy has been improved and optimization time was reduced [103]. Further, the SNOPT method with a numeric gradient has been used to study the optimization solver and also adding the optimization node to study the AC stationary impedance [104].

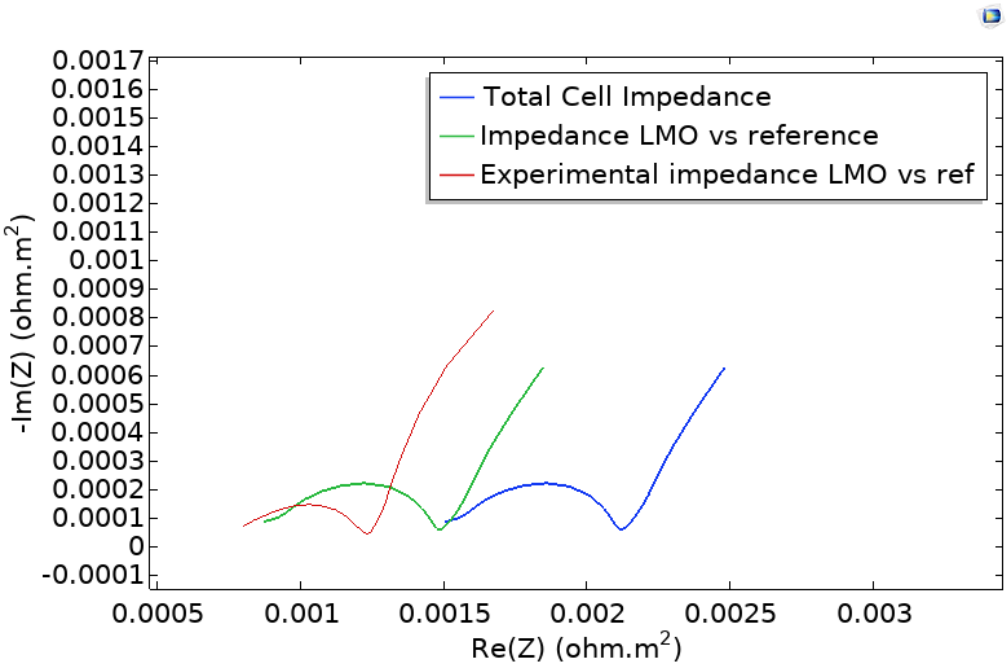

Figure 3.2 Nyquist plot of the impedance spectrum at variable frequency range.

The simulation results indicate the cell impedance and positive electrode LMO with reference has a large semi-circle as shown in figure 3.2 with dark blue and green solid lines respectively, whereas the experimental spectra of LMO with reference have a smaller semi-circle represented in red solid line. The semi-circle represents the charge transfer resistance (R_{ct}) value of total cell impedance, a positive electrode (LMO), and the experimental impedance of LMO was 2.2×10^{-3} Ω-m^2, 1.55×10^{-3} Ω-m^2, 1.22×10^{-3} Ω-m^2, respectively. This plot shows the difference in the charge-transfer resistance of both experimental and simulation curves and this difference was most prominent due to the short time scale process in the experiments. Hence, to overcome this difference, the four control parameters were plotted with a parametric sweep for comparing experimental and simulation plots as shown in figure 3.3. The parametric sweep has been used to investigate the control parameters and also to determine their impact on the cell impedance. Figure 3.3 shows the Nyquist spectra for testing the control parameters with in frequency range of 10 mHz to 10 kHz. This result shows that there was a change in the charge transfer resistance (R_{ct}) of both experimental and simulation spectra of positive electrode LMO.

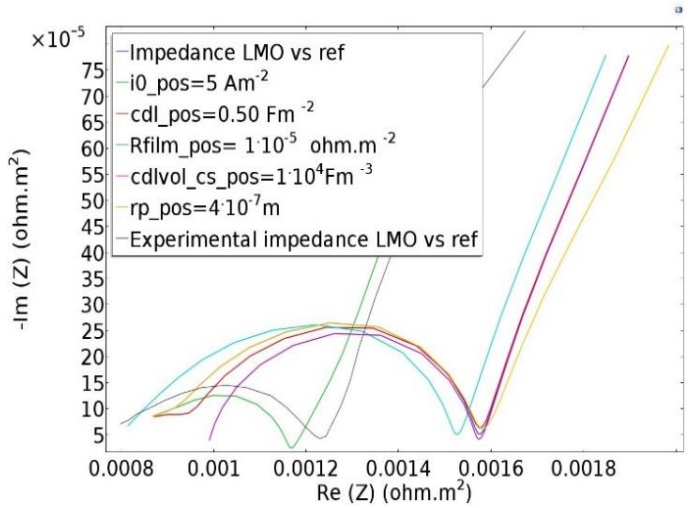

Figure 3.3 Nyquist plot of the impedance spectra for five control parameters at variable frequency.

The R_{ct} value of the positive electrode, LMO in case of experimental and simulation are observed as 1.29×10^{-3} Ωm^2 and 1.6×10^{-3} Ωm^2, respectively. This value of charge transfer resistance reveals a large time-scale process of diffusion in the particles. Its impact is, therefore, more evident in lower-frequency regions. Hence, the LMO positive electrode has greater electronic conductivity after the parametric sweep function. Here, simulation results also clearly reveals that the electrochemical reaction is also limited to their electrodes. This mainly depends upon the internal control parameters, due to which total cell impedance was affected. Further, for improving the electronic conductivity and reducing the cell impedance, the internal impedance control parameters as well as manufacturing impurities and defectiveness should be in proper control.

C. Galvan static Charge and Discharge characteristics (GCD)

For this characterization, the comparative results of two different types of anodes (graphite and MCMB) are plotted on the cylindrical Li-ion battery in which, two combinations of different anode materials have been investigated. The two-electrode pair are formulated, one is LMO/Graphite and the other one is LMO/Carbon (MCMB). The only difference between both these electrode pairs is the change of anode material, through which cathode material was

investigated and evaluated during its characterization. A 2D model of a Lithium-ion battery has been simulated to understand the behavior of $LiMn_2O_4$ cathode material and the rate capability of the battery [105]. Initially, the battery was discharged from its charged state and then fully charged from its discharged state at different C-rates and the discharge characteristics are plotted as shown in the figure. 3.4. The LMO/graphite discharge curve represents the discharge capacity of the battery in an open circuit which is estimated as 99.5% of its battery capacity.

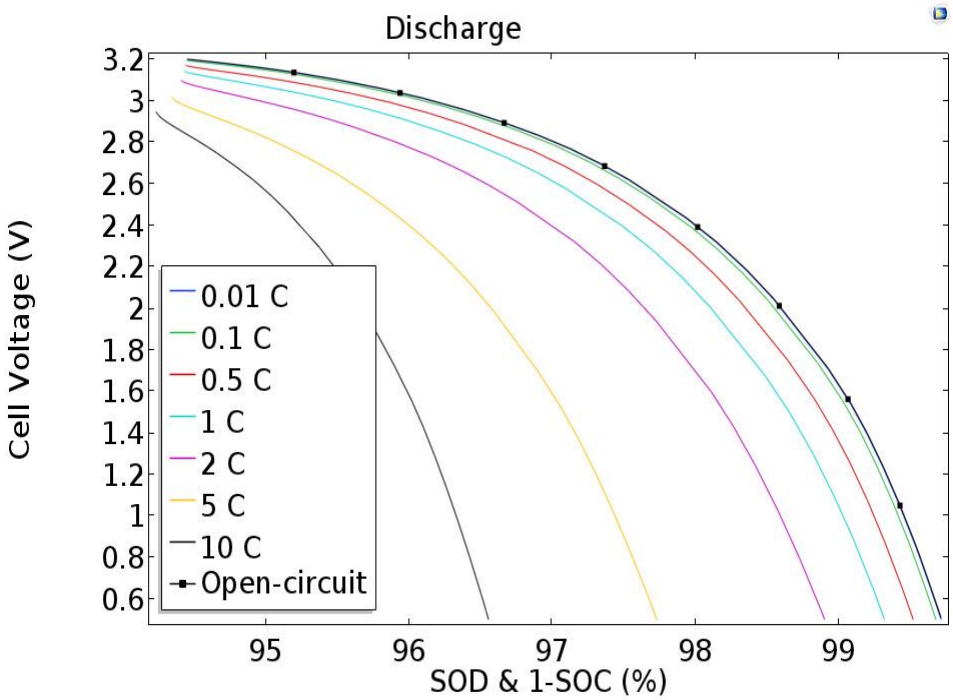

Figure 3.4 *State of Discharge (SOD) Characteristics of LMO/Graphite Combination of cell as cathode and anode materials.*

As the load current starts increasing the voltage drop (polarization) across the battery is also observed to be increasing and it results in a decrement in the capacity of the battery. Hence, when the load current is increased up to 10C rate, the capacity is reached approximately 96.7% of the ideal battery capacity.

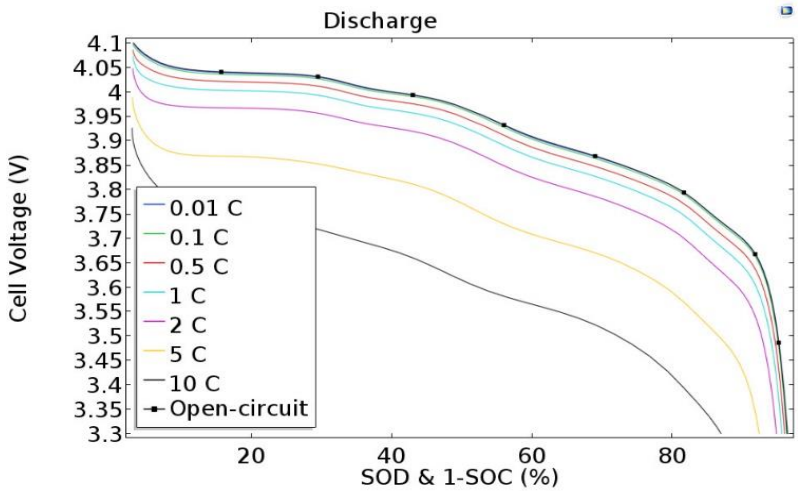

Figure 3.5 *State of Discharge (SOD) Characteristics of LMO/carbon (MCMB) Combination of cell as cathode and anode materials.*

Figure. 3.5 represents the combination of LMO/carbon (MCMB) discharge curve at different low to high discharge rates. Which indicate the similar discharge plots but its capacity is found lower as compared to LMO/graphite electrode and at 10 C rate, the battery capacity is decreased up to 88% of its full capacity. This shows that the LMO/graphite electrode material has better rate capability at a high C-rate than that of the LMO/carbon (MCMB) electrode. Investigations on the cylindrical Li-ion battery's charge characteristics revealed that the battery's charge capacity was less than its discharge capacity. The medium-high current load of the active electrode material and the battery's cell voltage fall inside the electrolyte's stability window, which is the cause of this phenomena [105-109].

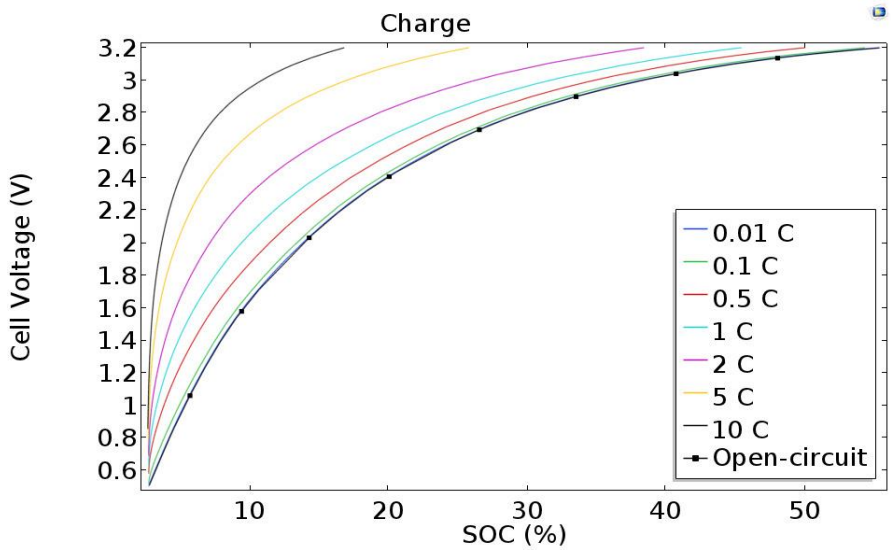

Figure 3.6 *State of Charge (SOC) Characteristics of LMO/Graphite Combination of cell as cathode and anode materials.*

The charge characteristics of LMO/graphite have been plotted in figure 3.6 and it is found that even though the charge capacity was lesser than the discharge capacity, polarization is observed in the discharge curve having the same plateau at 3.2 V. It clearly indicates that the LMO/graphite is stable in nature during oxidation and reduction process.

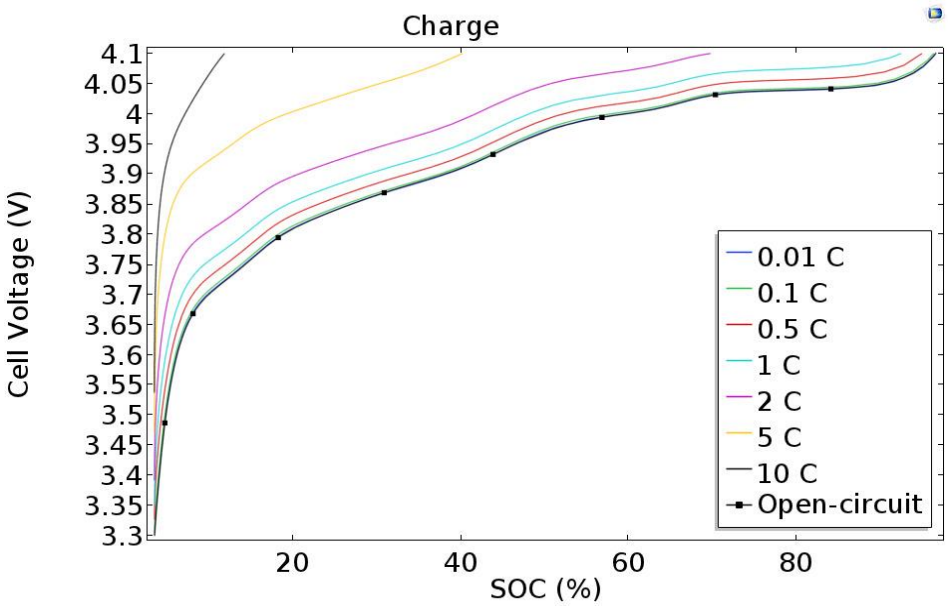

Figure 3.7 *State of Charge (SOC) Characteristics of LMO/Carbon (MCMB) Combination of cell as cathode and anode materials.*

Figure 3.7 depicts the charge characteristics of the LMO/MCMB. It can be seen that while its charge capacity is lower than its discharge capacity, it has a lower charge capacity when

compared to the LMO/graphite. Because of this, it suggests that LMO/graphite has superior battery performance than LMO/carbon (MCMB).

D. Ragone Characteristics

The Ragone plot is obtained to find out the energy and power output in both the combination of batteries make of LMO/Graphite and LMO/Carbon (MCMB). The Ragone plot helps to calculate the energy output using global ordinary differential equation (ODEs) and differential algebraic equation (DAEs) interface according to equation 3.1 [109-114].

$$W = \int_0^t (I.E_{cell})\, dt \tag{3.1}$$

Where, I represent the current in the battery and E_{cell} represent the cell voltage of the battery

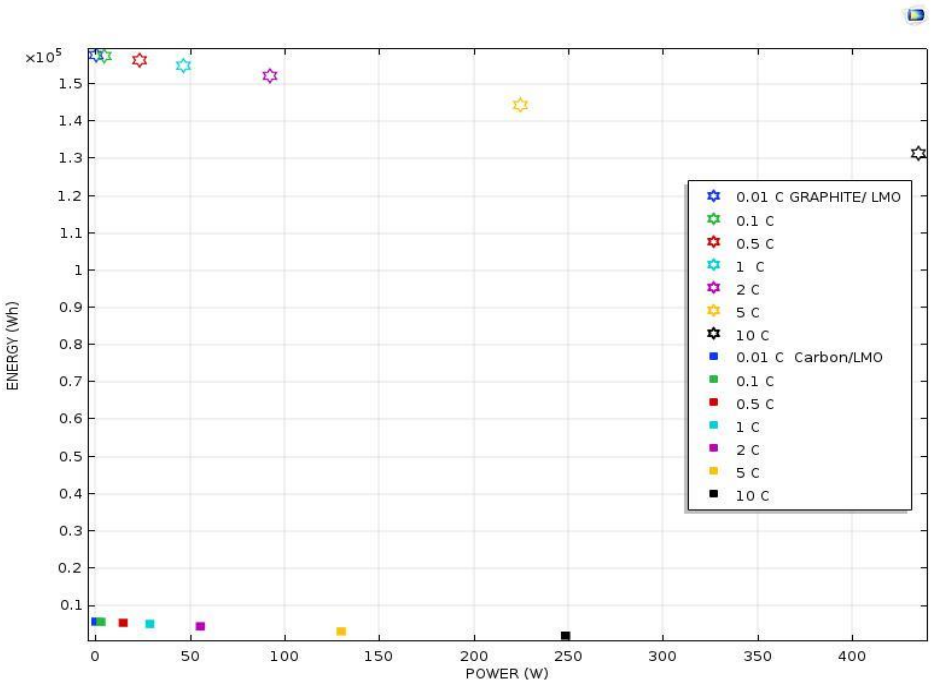

Figure 3.8 *Ragone Plot of LMO/Carbon (MCMB) and LMO/Graphite cell as cathode and anode materials.*

The power output has been plotted (figure 3.8) by dividing the energy by the total discharge time and the battery's operation has been limited by the event interface to the upper and lower cut-off voltages [114]. The ragone curve in figure 3.8, shows that LMO/carbon (MCMB) has lower energy as compared to LMO/Graphite which is due to the lower cell voltage of the

battery. Hence, good rate capability may be achieved using the LMO/Graphite electrode material.

3.2.1.2 Electrical Analysis

The simulated electrical characterization are plotted to obtain the data during simulation such as cell current, potential and load at various C-rate. Figure 3.9 represents the cell potential at limiting range 4.2V and 4V during charging and discharging operation. Similarly, battery load curve demonstrates the charging and discharging phenomenon which helps to evaluate the charging and discharging time in a constant manner during operating condition.

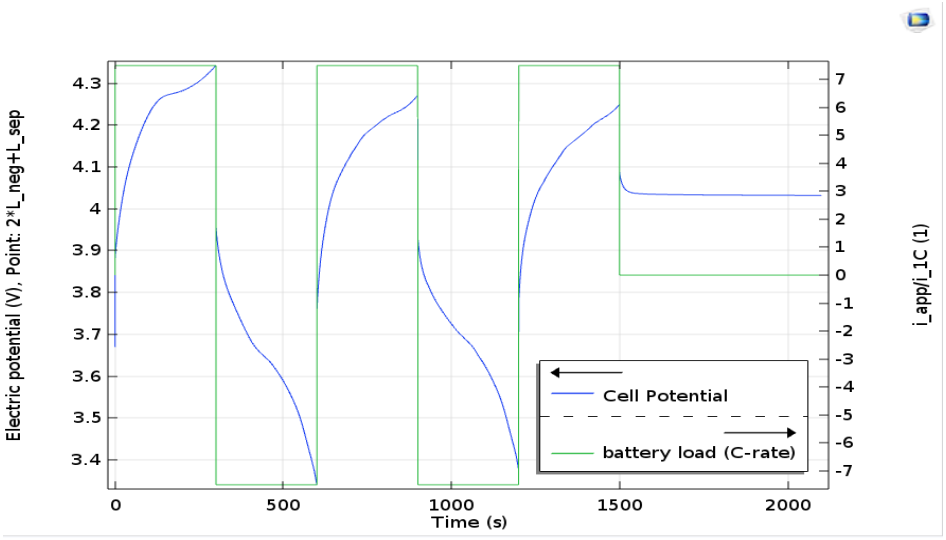

Figure 3.9. *Cell current, Load and Potential during a drive cycle.*

Figure 3.10 represents the mechanical polarization test of the cell, which shows the internal resistance as well as the life cycle of the cell. If polarization across the cell was large then it may lead to the small life cycle as well more heat generation across the cell so it should always be minimum.

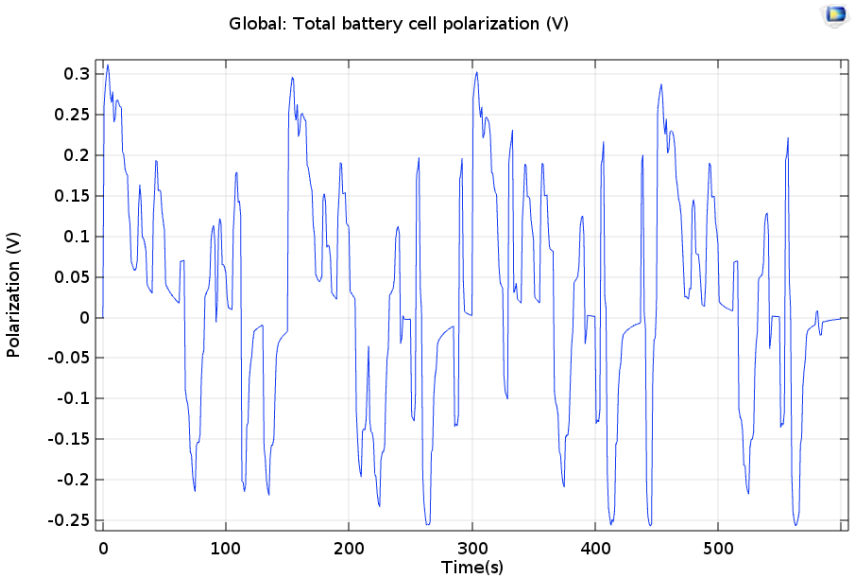

Figure 3.10 *Mechanical Polarization test for cell.*

In this result, polarization voltage was very small about 0.3V which would be considered as a negligible internal resistance across the cell and its cycle represents the cell life which was stable during the drive cycle and also less heat generation in the cell was observed.

3.2.1.3 Thermal Analysis

In this simulation, a lithium-ion coin cell has been formulated through the software and for thermal analysis, a heat source generator is connected with a separator to raise the temperature of the cell. Using homogenized properties, a convective heat flux boundary condition was set for analyzing the temperature difference across the cell. The temperature across the cell increase gradually, the heat flows across the separator in one direction only. Figure 3.11 represents the surface temperature after the 1500s, in which the temperature was uniformly distributed over the surface of the cell and heat was accumulated for a long time across the cell.

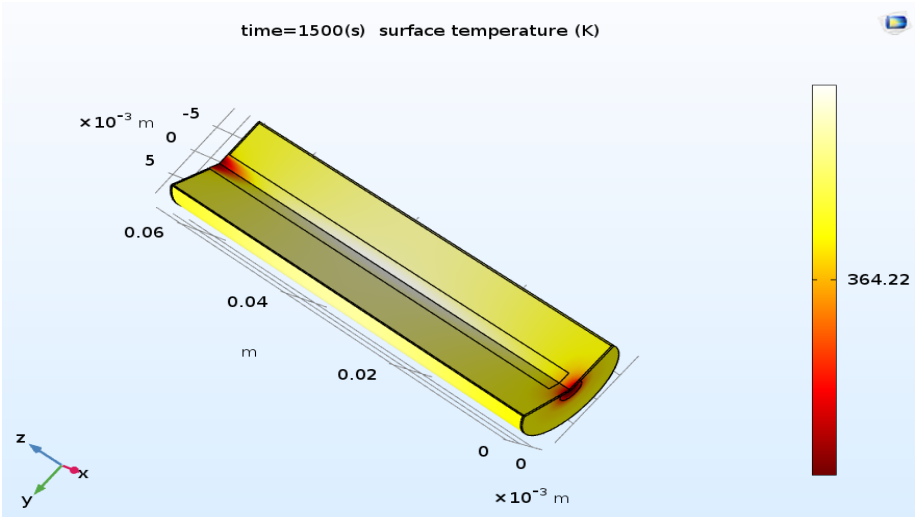

Figure 3.11. *Temperature distribution on the surface of the cylindrical cell.*

After the 3D simulation view of the coin cell, the plot has been plotted at various interval timing and analyze the temperature change across the cell. Figure 3.12 represents the plot of temperature in which mean, the maximum and minimum temperature was analyzed and it shows that there was no variation in the temperature and no hot spot was shown across the boundary of the cell.

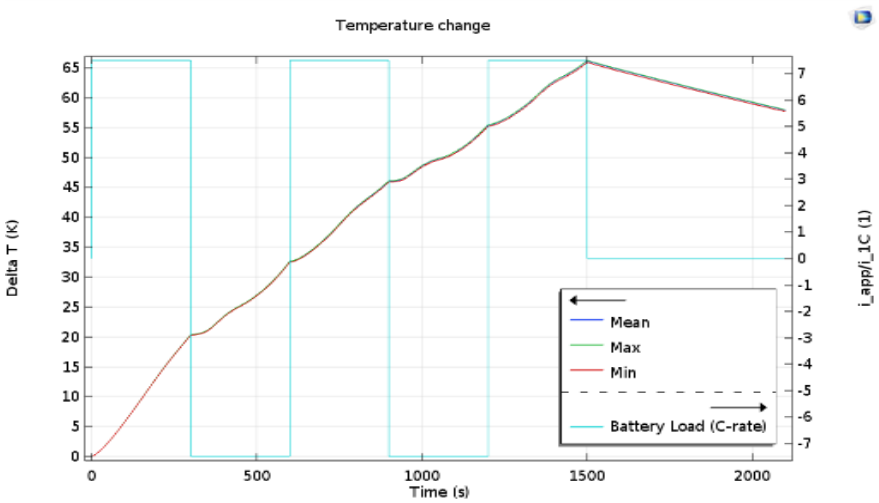

Figure 3.12 *Minimal Variation of the temperature of the cell with time during drive cycle at 1C rate.*

Also, the temperature across the battery was going on increasing during the charge and discharge drive cycle. In the above plot, the battery load at various C-rate was constant which

shows stability in the coin cell. Further, the olivine cathode material (LFP) has been simulated and the characteristics of the cell is evaluated in the next section.

3.2.2 Result of Olivine type cathode- $LiFePO_4$

In this simulation, a coin-cell type Li-ion battery has been modeled for the investigation of $LiFePO_4$ (LFP) cathode material and evaluate the electrochemical characteristics of the battery under the influence of different temperature and operating conditions and results are explained. All the results are analyzed at different boundary conditions and illustrated with a brief description.

3.2.2.1 Electrochemical Analysis

A. Cyclic Voltammetry (CV)

The CV has been performed under the influence of quasi-static approximation with the help of an electroanalytic technique [115]. In this method, a microdisk electrode was designed in which the surface concentration present on the surface of the electrode that was almost equally distributed. Figure 3.13 demonstrates the surface concentration for mass transport-controlled oxidation species. This result helps to investigate the uniform distribution of potential over the surface of the electrode.

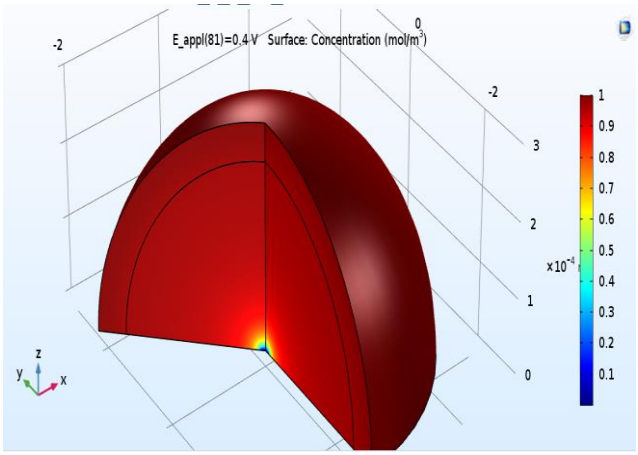

Figure 3.13 *Surface concentration at a microdisk electrode for evaluating the internal surface potential of the LFP model (3-D cross-section model).*

Further, figure 3.14 represents the variation of total current and voltage under steady-state condition. Initially, the total current across the LFP electrode was negligible because the oxidation reaction and it does not take place due to the reducing potential. As the potential increases the oxidation reaction takes place during charging process.

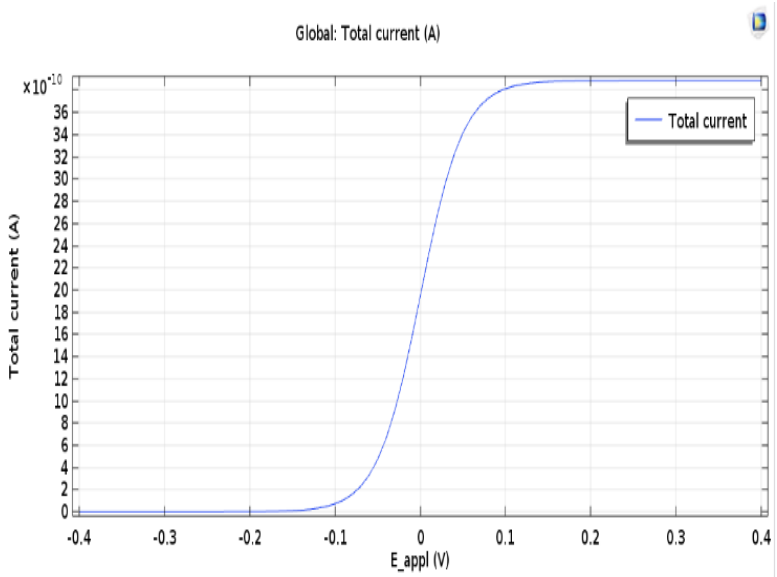

Figure 3.14 *Steady-State Cyclic Voltammogram at a Microdisk LFP Electrode.*

Similarly, the total current across the electrode also starts increasing during this phenomenon [116]. Once the oxidation takes place, the total current across the electrode becomes stable and limits the rate of transport species towards the working electrode. This outcome demonstrates the connection between electrode kinetics and the transport of chemical species.

B. Electrochemical Impedance Spectroscopy (EIS)

EIS is used to examine a battery's harmonic response. The kinetic and mass transport characteristics of the coin-cell battery are revealed using this method, and the capacitive characteristics of the Li-ion battery are also explained [117]. In figure 3.15 shows the relationship between real and imaginary impedance with a variable frequency range. This result has been analyzed at a very-low-frequency range of ko =0.001 cm/s in which mass transport always dominates through which semi-circle obtained. Whereas, at high-frequency range of ko =0.1cm/s, the transition to kinetic control occurs at which straight line obtained on the curve.

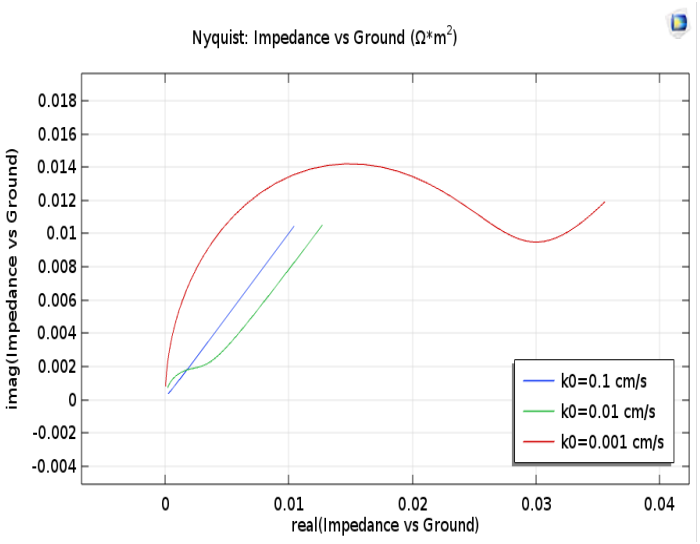

Figure 3.15 *Nyquist plot of LFP electrode at a various range of frequency.*

Figure 3.16 represents the Bode plot at various frequency ranges in which magnitude and phase angle was plotted through which reaction proceeds under the kinetic and transport control at a heterogeneous constant.

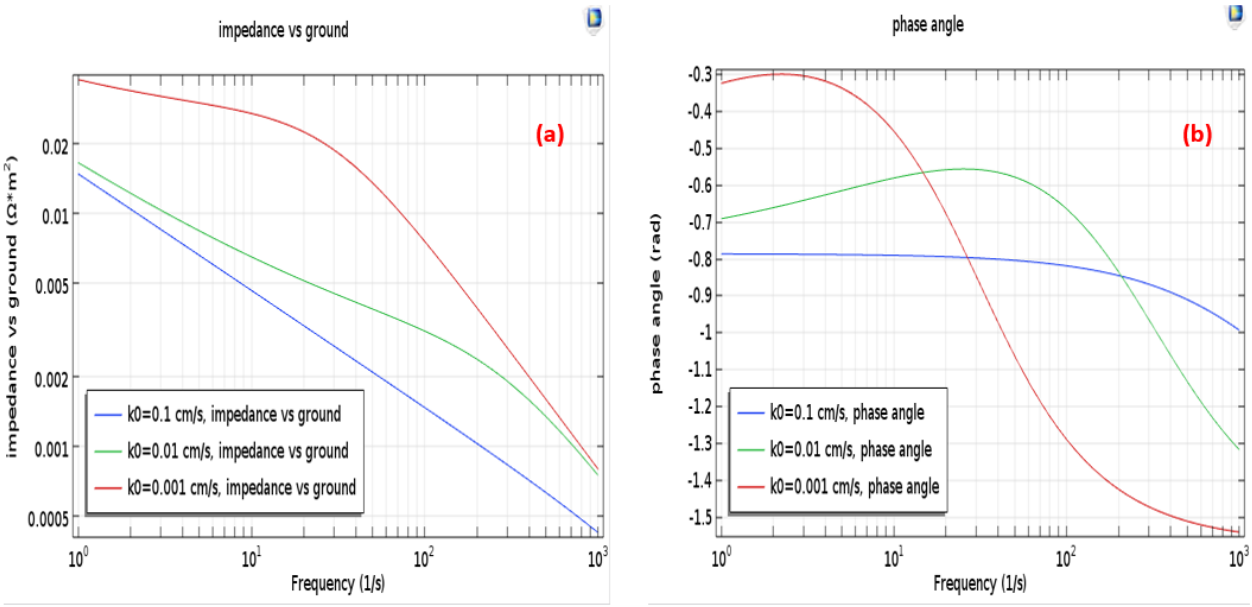

Figure 3.16 *Bode plot: (a) Magnitude of impedance, (b) Phase angle of the complex impedance at a various frequency Range.*

C. ***Galvanostatic charge and discharge characterization (GCD)***

This was the P2D modelling approach in which discharge curve was plotted at various current densities such as 0.1C, 1C, 2C, and 4C as shown in Figure 3.17.

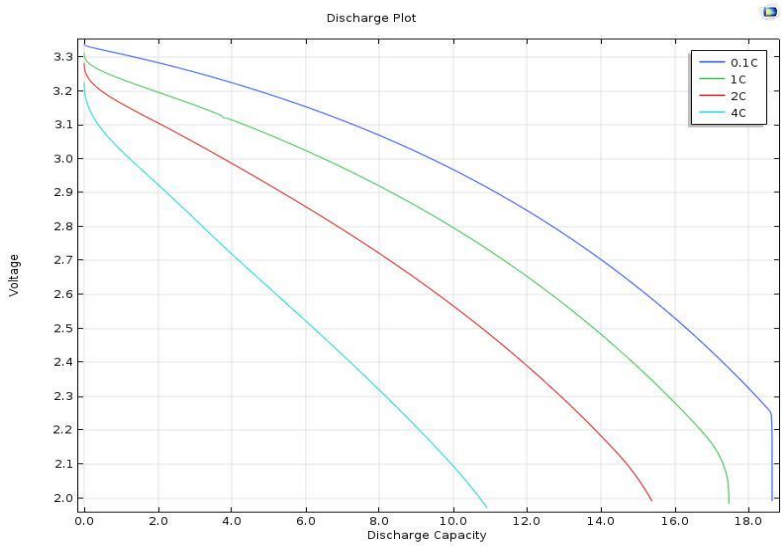

Figure 3.17. *Discharge curve at various low to high C-rate at the time when voltage drop at 3V.*

It is observed that the maximum discharge capacity has been calculated at a 1C rate at the end of the discharge curve at a time when the cell voltage falls below 3 V, leading to a sharp decline in discharge capacity. The nominal discharge current density, corresponding to 1C rate is 17.5 A/m^2 (current density corresponding to a theoretical full discharge in one hour). Additionally, if we evaluate at a 4C rate, the battery's theoretical capacity is 50% of its actual capacity before it hits 3V.

3.2.2.2 Electrical Analysis

In this investigation, the model used with certain boundary conditions and to keep the electronic current balance inside the battery, negative current collector potential has been kept 0 V, whereas at the positive current collector, the current density is set. Hence, the current density is cycled through discharge cycle in which current is set at zero interval initially and then move towards the final charging stage [118].

During this investigation, the conductivity of the LFP cathode electrode was depend upon the electrolyte of the cell because the electrolyte provides the conductive medium across the cell. Hence, electrolyte evaluation also performed during this simulation for demonstration of ionic conductivity and electric potential. In figure 3.18, the ionic conductivity of the EC:DMC (1:1)

concentration electrolyte has been simulated in which conductivity directly depends upon the equilibrium potential of positive and negative electrode. This function varies according to the charge and discharge phenomena because of the change in the material composition.

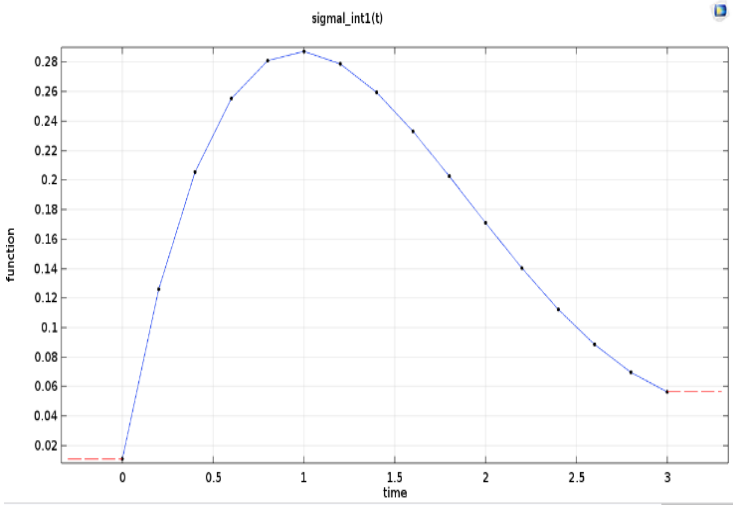

Figure 3.18 *Ionic conductivity of the EC:DMC (1:1) concentration electrolyte.*

Furthermore, in figure 3.19 demonstrates the electrolyte salt concentration at various times such as 600 s, 1200 s, 1800 s, and 2200 s which elaborate the voltage profile of the electrolyte. This curve is plotted during the operation of cell in which the cell experiences a sudden steep in voltage due to the electrolyte has a low effective diffusion coefficient. This, in turn, leads to variation in electrolyte concentration and ionic conductivity.

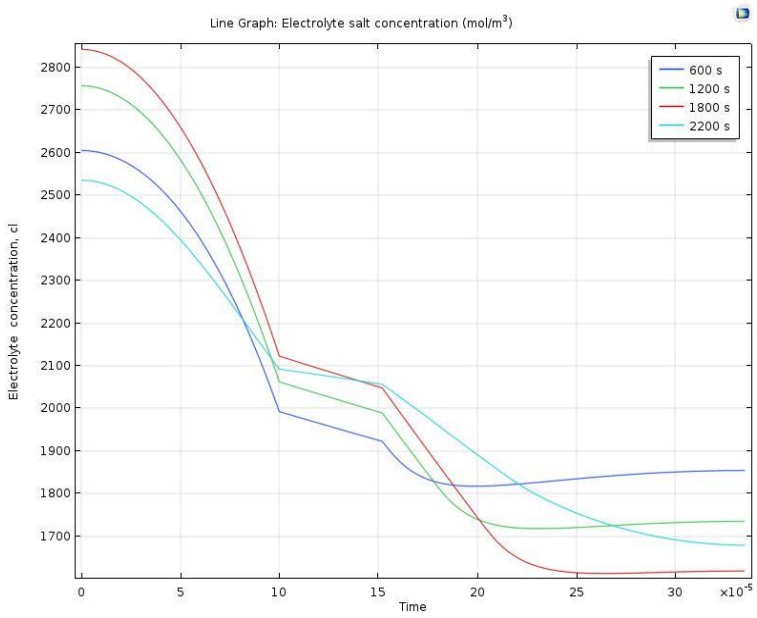

Figure 3.19 *Electrolyte salt concentration at various times.*

Figure 3.20 represents the voltage and current curve during the charge-discharge cycle. This plot is obtained at a nominal current of a 1C rate.

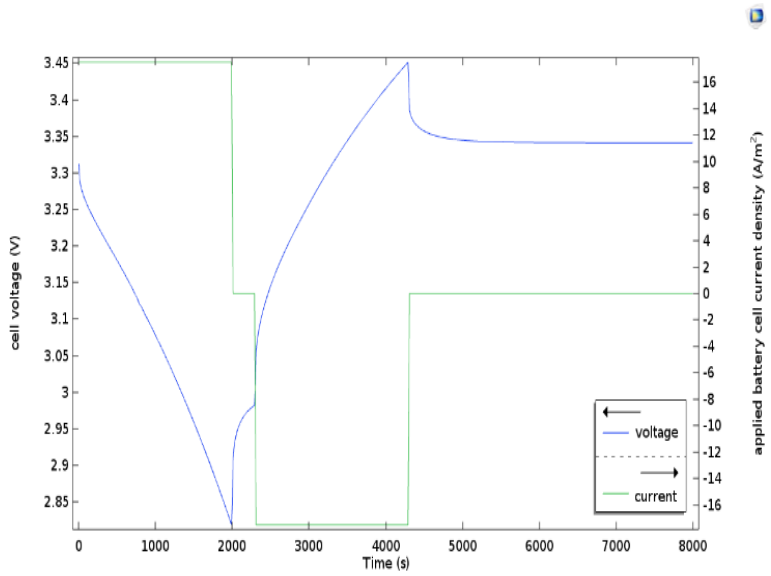

Figure 3.20 *Cell current and voltage of LFP cathode during the charge and discharge cycle at 1C rate.*

Initially, the cell is discharged at 1 C rate for the 2000 s then the circuit remains open for 300 s. After that, the cell is again charged for the 2000 s than it is completely left as an open-circuit. It has been noticed that Ohmic loss is observed in the voltage curve during holding the charge for 300 s. When the current value is kept zero.

3.2.2.3 Thermal Analysis

A 3-D coin-cell type model has been developed in which a penetrating filament (named as temperature monitoring) is used to raise the temperature of the cell which has been connected through the separator between the two electrodes [119]. The initial temperature of the cell is 300 K and it attain maximum temperature 398 K during charging – discharging process as observed by simulation. Figure 3.21 represents the temperature distribution over the surface. Initially, the temperature filament conductivity is set very low after it ramped towards the full conductivity

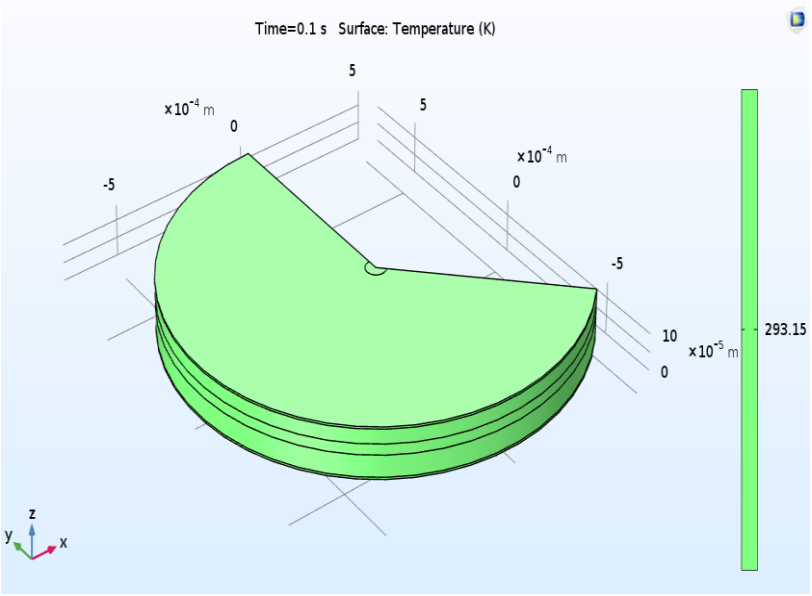

Figure 3.21 *Temperature distribution over the surface of the LFP electrode at t = 0.1 s.*

In this result, the temperature is equally distributed over the surface of the LFP electrode for a penetrating filament radius of 5 μm at time t = 0.1sec, which shows a good temperature distribution and the maximum temperature is located close to the penetrating filament. Hence, the temperature change is confined to a small space close to a filament and the overall surface electrode has a uniform temperature.

Chapter 4: Computational modelling for Novel Olivine-Spinel Dual Composite ($LiFePO_4$- $LiMn_2O_4$) Cathode Material for Lithium-ion Batteries.

This chapter includes the computational modelling for intercalation cathode material. The computational results have been simulated through which the electrical and thermal performance of novel olivine-spinel dual composite ($LiFePO_4$- $LiMn_2O_4$) cathode materials has been explored for a rechargeable lithium-ion battery. Furthermore, the novel sample can be ascribed in the form of the battery pack in which the 3D visualization of the thermal runaway has been simulated and studied the behavior of the cells. Additionally, this modeling provides a platform for other researchers to integrate modeling and experimentation in the future.

4.1 Introduction

To enhance the electrical and electrochemical properties of cathode material as discussed in section 1.5, the dual composite material has been simulated to increase the conductivity of cathode material. In this dual composite material, the positive cathode has dual intercalation lithium-metal-oxide electrodes while the negative electrode is generally carbon-based material. The energy storage of the LIBs depends directly on the active material of the electrode, which migrates from the positive to the negative electrode during charging and vice versa. These charging and discharging phenomena directly reflect the degradation of the battery's chemical and structural stability as well as capacity. Therefore, there is need to focus more on cell chemistry and new materials in this field to optimize the wide variety of applications [120-124].

For further improvement of all these complex numerical methods, it is important to have an integration with a computational approach that can help to understand the performance, design, and experimental data. So far, simulation has depended heavily on cell modules in simplified form (e.g. 1D and P2D model) and also explored the electrical and thermal model to account for cell performance and stability.

This pseudo-two-dimensional (P2D) dual composite model describes a Li-ion battery with two cathode materials of different intercalation such as $LiFePO_4$ (LFP) and $LiMn_2O_4$ (LMO) in the positive electrode, while the negative electrode consists of only one intercalation material such as black carbon (MCMB). There were multiple parameters that plays an important role in the model such as effective electrolyte properties and these properties were based on the Bruggeman relation. Furthermore, this model was validated using an experimental approach. In this model, two intercalation active materials with a different compound ratio such as

1LFP/3LMO, 1LFP/1LMO, and 3LFP/1LMO are used in the positive electrode. These materials have different input properties for the simulation, which have been elaborated in Table 4.1.

Table.4.1 *Intercalating Cathode Material Properties.*

S. No	Design Properties	Thermodynamic Properties	Transport Properties	Kinetic Properties
1	Volume Fraction	Equilibrium Potential	Solid Diffusivities	Intercalation Reaction Rate Constant
2	Particle Sizes	Maximum Lithium Concentration	-	-

P2D model was designed to evaluate the battery performance during discharge conditions for different mix fractions of the two intercalating materials in the positive electrode. Also, to evaluate the thermal distribution in a battery pack at a 4C discharge. Different types of input parameters like geometry design, material properties of the positive and negative electrode, boundary conditions, temperature conditions, and many more have already been described in previous chapter 3 for lithium-ion modeling. However, Table 4.2 describes some more model-related parameters.

Table 4.2. *Internal design parameter for 2D Lithium-ion battery.*

Name	Expression	Units	Description
rp_pos_LFP	$2.5 \times e^{-6}$	$2.5 \times e^{-6}$	Particle radius LFP positive electrode
rp_pos_LMO	$1.7 \times e^{-6}$	$1.7 \times e^{-6}$	Particle radius LMO positive electrode
rp_neg	$2.5 \times e^{-6}$	$2.5 \times e^{-6}$	Particle radius active material negative electrode
i0ref_pos_LFP	7.32	7.32 A/m²	Reference exchange current density LFP positive electrode
i0ref_pos_LMO	17.44	17.44 A/m²	Reference exchange current density LMO positive electrode
i0ref_neg	0.96	0.96 A/m²	Reference exchange current density active material negative electrode
brugl_pos	2.98	2.98	Bruggeman coefficient for tortuosity in positive electrode
brugl_sep	3.15	3.15	Bruggeman coefficient for tortuosity in separator

T	298	298 K	Temperature
L_neg	50 x e^{-6}	5 x e^{-5} m	Length of negative electrode
L_sep	50 x e^{-6}	5 x e^{-5} m	Length of separator
L_pos	50 x e^{-6}	5 x e^{-5} m	Length of positive electrode
epsl_sep	0.37	0.37	Electrolyte phase volume fraction separator
epsl_neg	0.444	0.44	Electrolyte phase volume fraction negative electrode
epsl_pos	0.40	0.4	Electrolyte phase volume fraction positive electrode
epss_pos	(1-epsl_pos-0.17)	0.43	Solid phase volume fraction active material mix positive electrode
fr_pos_LFP	0.33	0.33	Volume fraction of LFP in LFP/LMO mix
epss_pos_LFP	epss_pos*fr_pos_LFP	0.1419	Solid phase volume fraction LFP positive electrode
epss_pos_LMO	epss_pos*(1-fr_pos_LFP)	0.2881	Solid phase volume fraction LMO positive electrode
SOC_cell0	0.98	0.98	Initial cell state-of-charge

4.1.1 Electrochemistry Domain for Mathematical Modelling

Several simulation models for redox-based energy storage systems have been simulated and modeled with different levels of complexity and idealization. This diffusion model is based on the gradient of the chemical potential to intercalate lithium as the driving force for diffusion since it was opposed by the gradient of lithium concentration for dilute solution treatment which was followed by Fick's Law for lithium transport in the active material particles. Equation 4.1's representation of the diffusion equation as spherical coordinates for the material balance of lithium in the particles demonstrates this.

$$J = -D\frac{d\psi}{dx} \tag{4.1}$$

Where J is the diffusion flux and D is the diffusivity of the ions. For redox-based energy storage systems, the differential equations of mass and charge conservation have been described, in which flux of charge with lithium ions has been associated with the conservation of species [125-128]. But, as the Butler-Volmer electrode kinetics equation helps us to elaborate the anodic-cathodic reaction at the interface and the local charge transfer current density, i_0 is taken as a function of the lithium concentration in the intercalating electrode as in equation 4.2. [129].

$$j^{Li} = \frac{i_o}{F}\left[exp\left(\frac{\alpha_a F}{RT}\eta\right) - exp\left(\frac{\alpha_c F}{RT}\eta\right)\right] \quad (4.2)$$

$$i_0 = k{c_e}^{\alpha_a}\left(c_{s,max} - c_s\right)^{\alpha_a}\ {c_s}^{\alpha_c} \quad (4.3)$$

Where all the symbols were already explained in a previous chapter 3. This Butler-Volmer equation always helps us to balance the charge for the material of the electrode and also behaves as a source and sink in the model [127-132]. The liquid electrolyte has been described in terms of diffusional conductivities for transport properties, which represent a volume fraction and are described in equation 4.4.

$$k_D^{eff} = \frac{2RTk^{eff}}{F}(t_+^0 - 1)\left(1 + \frac{d\ In\ f_{\pm}}{d\ In\ c_e}\right) \quad (4.4)$$

Where, k_D^{eff} represents the effective diffusional conductivity of the species. In this pseudo-two-dimensional (P2D) model, the additional coordinate is taken for solid-state diffusion because transport species flow along with the thickness of the electrode direction. Using solution theory, ions are always transported through the electrolyte and the pore-wall flux is set to zero near the separator across the electrode-electrolyte interface of the cell. However, the model is also based on the description of cell properties which can be evaluated with the experimental electrochemical characterization as referred to NTG model [132-134]. The detailed description of this model would go beyond the scope.

Furthermore, for thermal runaway, a heat transport species is expressed in the three-dimensional model in which heat conductivities can be computed with equation 4.5.

$$q = \rho^{C_p} \frac{\partial T}{\partial t} - \nabla (k \nabla T) \quad (4.5)$$

Where ρ the resistivity and Cp is the specific heat capacity of the electrode material. In addition, k is the anisotropic thermal conductivity and T is the temperature [133-135]. This equation is always used for dual-electrode inserted cells, which can change the heat entropy of a half-cell reaction with ohmic heating inside the cell and is also used for the computation of multiple cells, modules, and packs. The thermal generation, as well as electrical work for the battery pack, is always defined by the electrochemical reaction, the heat of mixing, phase changes, and heat capacity of the pack. Hence, this model helps to explore the heating behavior of the pack and the results of this model are further described.

4.2 Results and Discussion

In this study, the electrical data was plotted at the 1C discharge rate of the positive dual composite. This can be described to find out the positive electrode's surface concentration, which is crucial for solid-state batteries. In addition, the thermal runaway inside the battery pack was also discussed in the 3D model.

4.2.1 Simulated Results for Dual LFP-LMO composite

4.2.1.1 Electrical Characterization

The simulated results are obtained in the form of electrical voltage. To ascertain the structural and kinetic characteristics of the active material during the intercalation of two distinct materials on the porous positive electrode, this simulation has been carried out. The battery performance is evaluated during discharge for a blend proportion of two intercalating materials. Figure 4.1 represent the discharge voltage profile for a different positive electrode mixed in the ratio of 1:1 at a discharge rate of 1 C. This result helps to demonstrate the electric potential discharge of the battery at 4.1V with a constant current. As the time increases, the electric potential also decreases and shows the voltage drop plateau across the 3.95V and 3.75V

respectively. Hence, the simulated result in this plot confirms the availability of two different intercalating compounds at the different electric potentials.

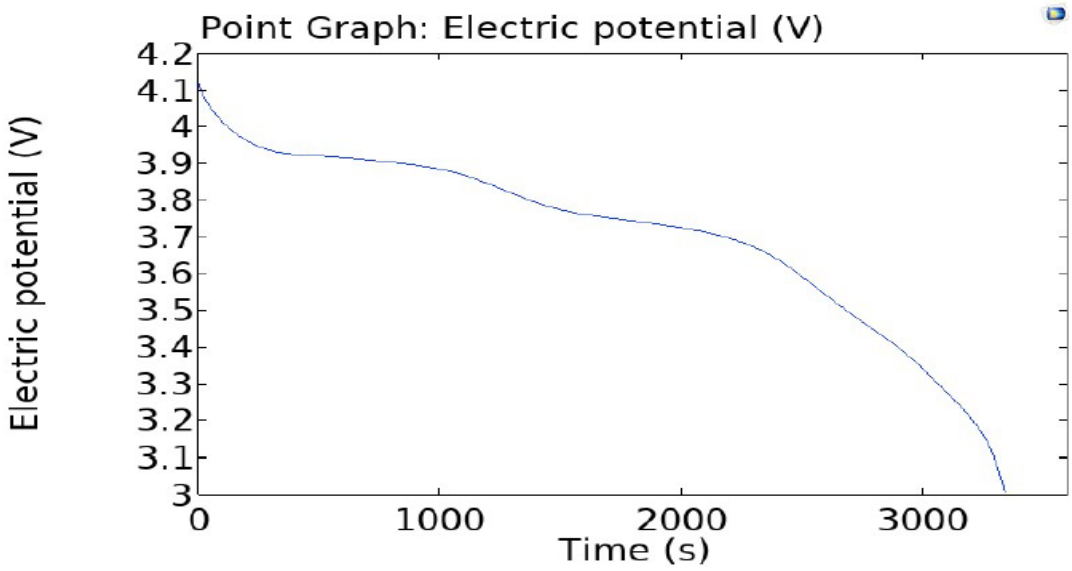

Figure 4.1. *Discharge Voltage profile at 1C rate of dual composite (1LFP/1LMO).*

Additionally, Figure 4.2 displays the lithium concentration at the particle's surface during a 1C discharge in the positive electrode.

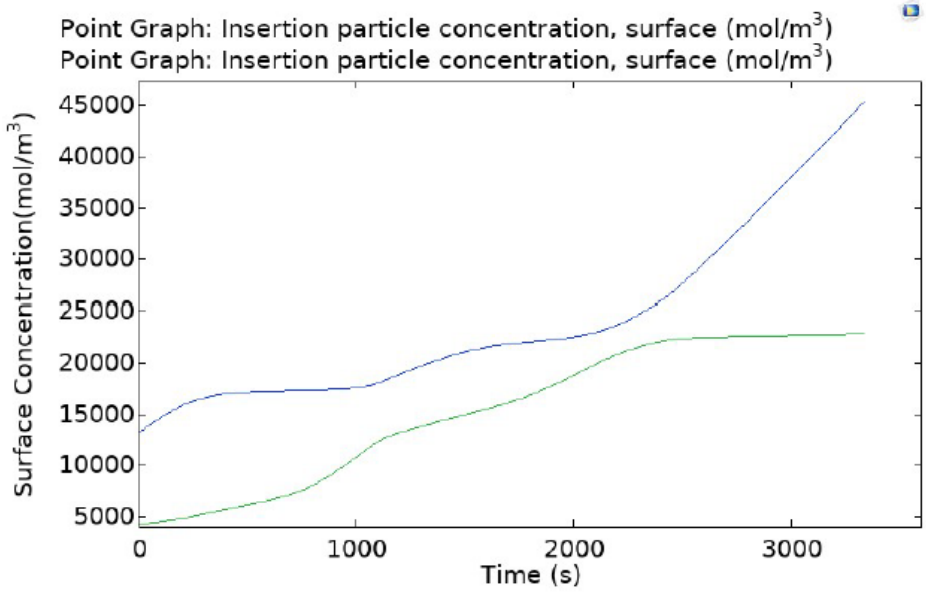

Figure 4.2 *Surface Concentration of the two active material in the positive electrode: blue line (LFP) and green line (LMO) during 1C discharge.*

This plot reflects the variation of the surface concentration with respect to time, in which the blue color and green color show the different active materials of olivine (LFP) and spinel (LMO) structure. This is because of the different electrochemical properties of the two active materials. Hence, the dual composite material confirms the availability of two active material of different properties in one intercalation compound.

4.2.1.2 Thermal Characterization

The thermal profile was modeled using a heat generation, with heat sources taken from the battery models, using electrochemical heating Multiphysics nodes. The battery pack was discharged from 100% to 20% state-of-charge (SOC) at a rate of 4C for 12 minutes.

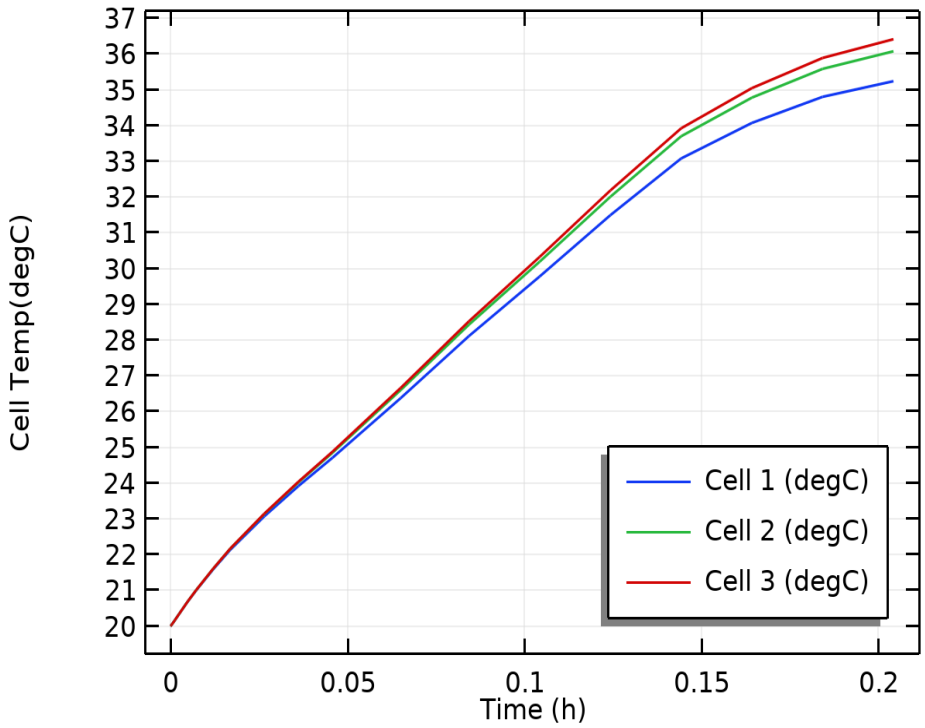

Figure 4.3 *Cell1, Cell 2, and Cell 3 of different mass ratios 1LFP/3LMO, 1LFP/1LMO, and 3LFP/1LMO at various temperatures with respect to time.*

Figure 4.3 shows the curve between temperature and time. In this plot, the three cells are taken for analysis Cell1, Cell 2, and Cell 3 for the different mass ratios as 1LFP/3LMO, 1LFP/1LMO,

and 3LFP/1LMO, respectively. In this plot, almost all the cells are equally assigned with respect to temperature but after a certain time, a slight variation in temperature has been observed and Cell 1, Cell 2 and Cell 3 show the maximum range up to 35˚C, 36˚C, and 37˚C, respectively. During this thermal simulation, error rate was 0.1% to 0.5% maximum due to which 1 degree difference is comparatively more. Hence, Cell 1 shows better thermal stability as compared to the other two intercalating compounds of different ratios.

4.2.2 3D Characterization of dual composite (LFP-LMO)

The 3D characterization of dual composite battery pack has been designed with a cell 1 as a 6S2P configuration. In this, twelve numbers of standard '32650' cylindrical cells of 32 mm diameter and 65 mm height have been placed adjacent to each other. Small connecting strips of pure nickel are taken to make a series and parallel connection to form a 6S2P battery pack combination. The whole battery pack is assumed to be wrapped in the soft casing (plastic wrap), forming a domain filled with air. Further, this battery pack was also used for the thermal simulation as shown in figure 4.4.

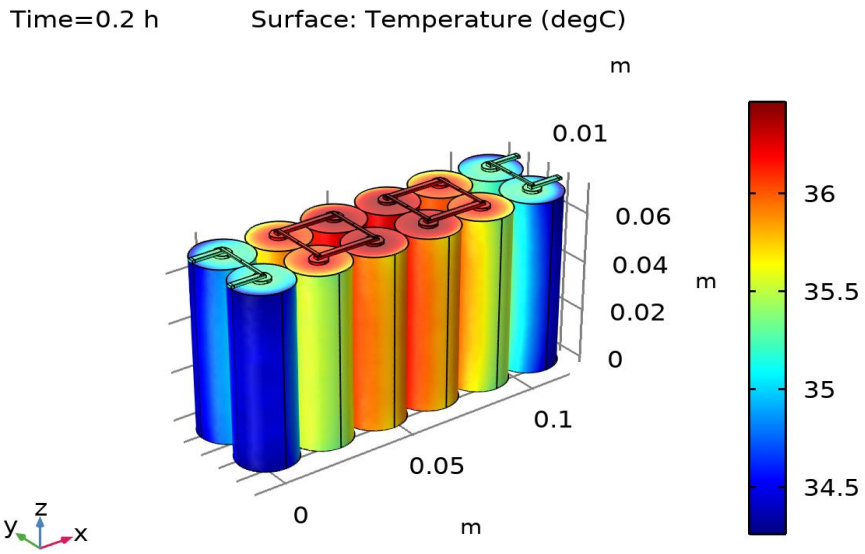

Figure 4.4 *Temperature distribution in the dual composite battery pack of 6S2P configuration.*

The 3D image of the battery pack temperature distribution as the color code distribution represents the blue color as higher temperature and the red color as a lower temperature was shown in figure 4.4. The inner part of the battery pack shows about 2 ˚C higher than the outermost part of the battery pack. The discharge voltage, ohmic drop, exchange current density, and diffusion time constant are all significantly lower in the battery pack's outermost cell, which also has a little lower temperature. Hence, the dual composite cathode material explored the electrical and thermal properties through simulation which conclude that the 1LFP/3LMO i.e. cell 1 is having good thermal stability. Now, after simulation study, the experimental study has been performed to explore the physiochemical and electrochemical properties of the dual composite cathode material in chapter 5.

Chapter 5: Physiochemical, Morphological, and Electrochemical characterization of the synthesized cathode materials for lithium-ion batteries.

This chapter includes the experimental part as synthesis and characterizations of both spinel- Type $LiMn_2O_4$ and olivine-type $LiFePO_4$ cathode material separately. The experimental results have been evaluated through which, $LiMn_2O_4$ cathode material comprises the sharp and intense peaks with the homogenous morphological structure and good conductivity with enhanced electrochemical performances. Similarly, the olivine-based $LiFePO_4$ material demonstrates the synthesized sample's good electrochemical performance and conductivity. Furthermore, these two cathode materials are used to synthesize and characterize the novel olivine- spinel dual composite ($LiFePO_4$ - $LiMn_2O_4$) cathode materials for lithium-ion batteries.

5.1 Introduction

In the last 100 years ago, revolutionary research work on primary and secondary batteries has been carried out. The creation of lithium-ion batteries began in the 1970s [136-137]. While certain other metal oxide materials, such as $LiMn_2O_4$, operate as a cathode, an older lithium-ion battery cathode material comprises several layered structures characterized as Li- cobalt oxide ($LiCoO_2$) or a tunneled structure called lithium- manganese oxide ($LiMnO_2$), $LiFePO_4$, $LiNi_{1-x}Mn_xCo_yO_2$ and many more were also introduced because of inherent advantages [123,131,136]. Out of the multiple structures, the olivine ($LiFePO_4$) and spinel ($LiMn_2O_4$) structures were chosen for the present research work because of their multiple advantages such as LFP having high theoretical and experimental capacity, 170 mAh/g while LMO has good electronic conductivity as already explained in chapter 2. Initially, the olivine structure and spinel structure material were synthesized independently using a sol-gel technique (section 2.2.1). Further, the physicochemical, thermal, electrical, and electrochemical properties of both the synthesized material were studied using TGA, XRD, SEM, FTIR, Ionic conductivity, and Electrochemical Impedance spectroscopy. After obtaining proper phase of a spinel and olivine type compound, a novel olivine-spinel dual composite has been synthesized using a solid-state solution with different mass ratio of both the compounds and abbreviated as 1LFP/1LMO, 3LFP/1LMO and 1LFP/3LMO and then physiochemical, electrical and electrochemical characterization are performed on the novel olivine-spinel compound.

5.2 Results and Discussion

In this section, the results and discussion of all the synthesized samples such as $LiMn_2O_4$, $LiFePO_4$, and ($LiFePO_4$- $LiMn_2O_4$) are provided. The synthesis of LMO, LFP and their dual composite, LFP-LMO were synthesized by sol-gel and solid-state routes as given in chapter 2:

2.2. Hence, the physicochemical characterization results observed by various techniques and their electrochemical analysis has been reported in this chapter 5.

5.2.1 Spinel based-$LiMn_2O_4$ Results

5.2.1.1 Thermal Characterization

Thermogravimetric analysis (TGA) has been performed to determine the decomposition and calcination temperature of the synthesized sample. The $LiMn_2O_4$ sample was characterized by the variation in mass loss at different temperatures as shown in figure 5.1. The TGA curve observed for $LiMn_2O_4$ represents the three main losses as shown in the red color solid line (TGA plot). The first transition loss is observed between 150 ˚C to 200˚C due to the dehydration of water molecules/moisture content. The second transition loss is observed between the temperature range of 250 ˚C to 375 ˚C which is related to the decomposition of organic and carbon elements and also during this transition mass loss (Δm) is estimated as 5.36%. This estimated mass loss is related to the endothermic reaction due to decomposition organic or oxalate compounds in the sample.

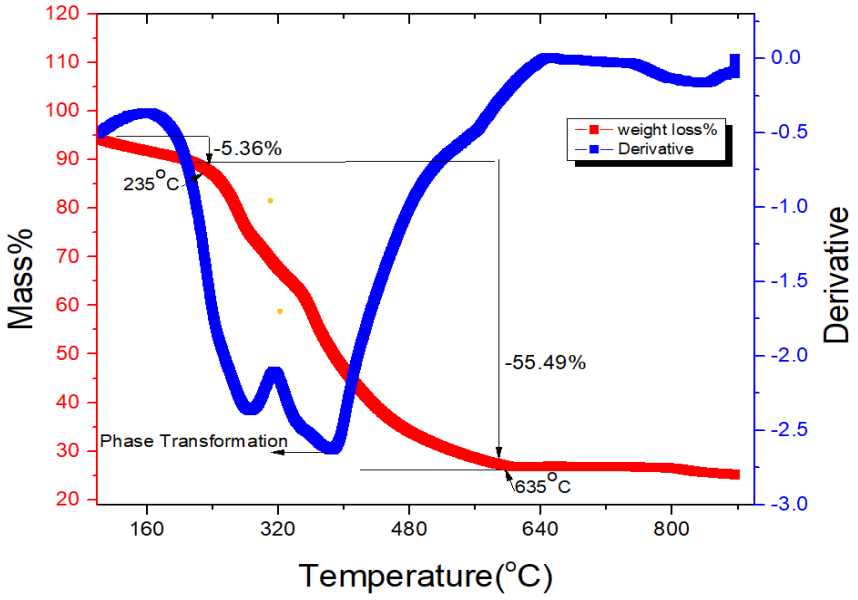

Figure 5.1 *TGA and DTA of LMO Sample observed under O_2 atmosphere at a scan rate of 10 ˚C/minute using Pt crucible.*

The third transition loss was the major loss that were associated in the temperature range of 635 to 800 ˚C with a mass loss of 55.49% as shown in figure 5.1, which corresponds to the decomposition of all the starting materials such as Lithium acetate and Manganese acetate. In differential thermal analysis (DTA), the sharp endothermic peak was occurred at 390 ˚C which was due to the decomposition of acetate and carbonate salts. Similarly, the other sharp endothermic peak was occurred at 650 ˚C due to the compound formation. After that, mixed phases of MnO_2 and Mn_2O_3 are formed and started to decompose in a stable region [121]. In this second region, a pure LMO starts to form a synergistic effect of three different compounds such as MnO_2, Mn_2O_3 and Li_2CO_3 as a phase transformation as well as carbon decomposition in the compound [138]. Therefore, the sample calcination has been performed in two stages: firstly, for the decomposition of organic compound the sample was calcinated at 350 ˚C for 6 hrs and the second calcination was performed at 775 ˚C temperature for 20 hrs to obtain the proper phase and morphology in the LMO sample.

5.2.1.2 Structural and Morphological Characterization

The sample's crystallinity has been determined using an X-ray diffraction (XRD) study. Figure 5.2 demonstrates the XRD pattern for the LMO sample indicates sharp peaks with the proper crystalline phase. Hence, the crystalline phase confirms the spinel-type cubic structure of $LiMn_2O_4$ with the F*d3m* space group and it matches well with the standard database files (JCPDS 00-035-0782).

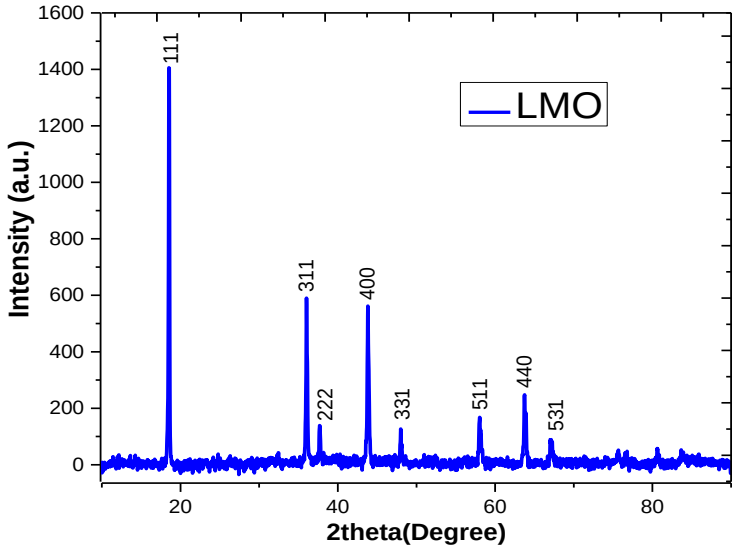

Figure 5.2 *XRD Pattern of synthesized sample of LMO prepared in O_2 atmosphere calcinated at 775 ˚C for 24 hours after decomposition.*

Many parameters were evaluated from the observed XRD patterns of as synthesized LMO sample and are shown in Table 5.1. The lattice parameter for the synthesized sample was 4.779 Å and the volume of the cubic cell was 109.14 $Å^3$. Further, the Williamson-Hall (W-H) plot data was calculated to evaluate the effect of broadening the peak (β_T).

Table 5.1 *XRD parameters of as-synthesized sample of LMO.*

Peak Position(2θ) degree	**FWHM (2θ) Radians**	**d-Spacing (Å)**	**W (4sinθ)**	**H (β_T cosθ)**
18.544	0.128	4.774	0.644	0.0022
36.017	0.122	2.490	1.236	0.0020
37.664	0.130	2.385	1.291	0.0021
43.817	0.153	2.063	1.492	0.2224
47.992	0.090	1.893	1.626	0.0014
58.066	0.176	1.586	1.941	0.0026

63.729	0.162	1.458	2.111	0.0024

The combined impact of crystallite size and the micro-strain was examined in relation to the broadening of the peaks. Hence, the W-H data was obtained to calculate the strain and crystallite size. The slope of the W-H data was 2.039×10^{-4}, which was represented as a strain on the broadening peaks. The grain size of the synthesized sample is calculated as 72 nm, using Scherer equation (equation 2.8). After the structural analysis, the morphological analysis has been carried out with the help of a Scanning electron microscope (SEM).

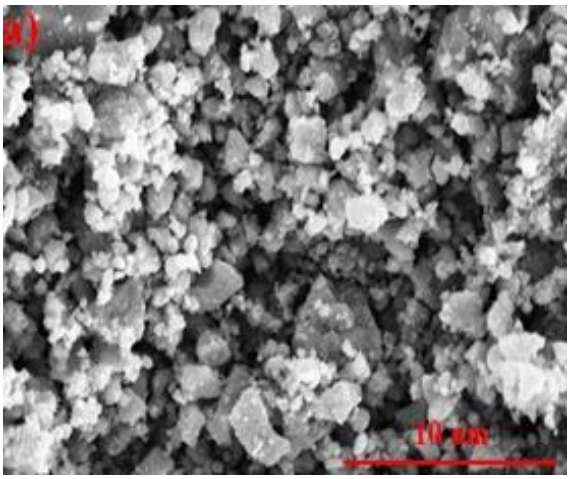

Figure 5.3 *SEM of the LMO sample.*

The SEM image of the as-synthesized sample is shown in figure 5.3 which indicates the smaller spherical-shaped grains with non-uniform morphology. The average grain size of the LMO sample is observed in the range of 8-10 μm as observed ImageJ software.

5.2.1.3 Fourier Transform Infrared Spectroscopy (FTIR) Analysis

The FTIR reveals the functional group of the organic compound and also shows the flow of cations in terms of vibrational modes. The FTIR spectrum of the LMO sample represents the four bands in which three bands show strong peaks as shown in figure 5.4.

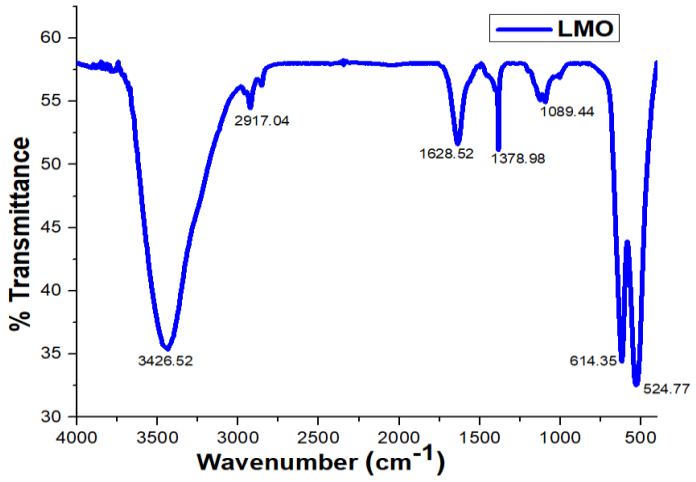

Figure 5.4 *FTIR Spectrum of LMO Synthesized sample.*

The three-strong bands/peaks in the spectrum are shown at 3426, 614, and 524 cm^{-1} in the different regions. In the first region, the peak is lying between 4000 to 2500 cm^{-1} at 3426 cm^{-1} and it was reflected due to the absorption of single C-H and O-H bonds in the sample. Whereas in the second region, the two peaks are located in the range of 2500 to 1000 cm^{-1} at 1628, 1378 cm^{-1} reflecting the small peaks associated with the C-O and O-H bonds. While the weak peak relating to water bonds as well as Mn-O bonds is confirmed at 1089 cm^{-1} vibrational frequency [139]. This high frequency is associated with the asymmetric stretching modes of the MnO_6 group [139,120]. In the third (finger print) region, the strong peaks are lying in the vibrational range between 1000 to 400 cm^{-1} at 614 and 524 $cm^{-1,}$ and both the peaks are associated due to the transition metals and also stretches relates the Mn^{4+}-O and Mn^{3+}-O respectively [140].

5.2.1.4 Electrical Characterization

The electrical characterization of the synthesized sample (LMO) has been evaluated with the help of ionic conductivity measurement. This characterization was also helped to evaluate the activation energy of the LMO sample.

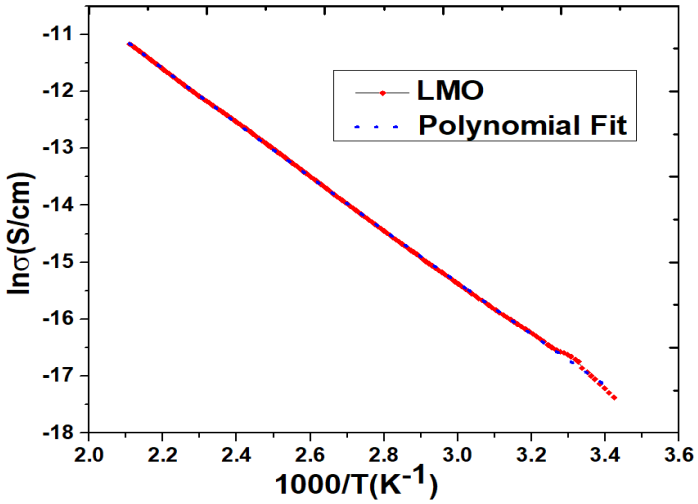

Figure 5.5 *Electronic Conductivity (DC) Measurement of $LiMn_2O_4$ (LMO).*

In figure 5.5, the ionic conductivity curve of the LMO sample was determined with the help of the KEITHLEY 6517A electrometer at a high resistance. This plot reflects the direct measurement of activation energy while calculating the slope of the straight line and also represents the kinetics of lithium-ion (Section 2.3.3, chapter 2). The calculated activation energy of the synthesized LMO sample was 401.94 meV and the electronic conductivity was 4.42×10^{-8} S/cm. These calculated parameters reflect the LMO sample has conductivity of the order of semiconducting material.

5.2.1.5 Electrochemical Characterization

In this characterization, the electrochemical impedance spectroscopy (EIS) of the LMO material was plotted for validation and comparison of simulation results (Section 3.2.1.1, chapter 3). This curve was plotted for a reference to simulate the internal parameters as well as to develop and control the other internal parameters for the enhancement in simulated results (Section 3.2.1.1, chapter 3).

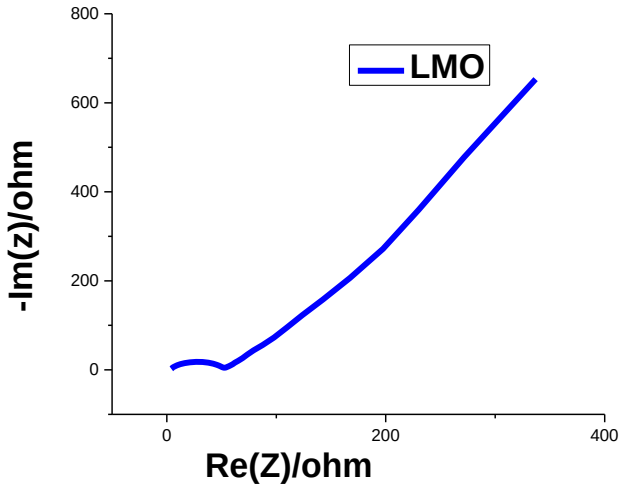

Figure 5.6 *EIS characterization curve of LMO synthesized sample in the frequency Range of 20 Hz to 1 MHz.*

This EIS curve is plotted within the frequency range of 20 Hz to 1MHz with a 5 mV AC pulse to determine the AC impedance and diffusion coefficient of the synthesized sample (section 2.3.4.3, chapter 2). In figure 5.6, the semi-circle has been intercepted on the z-axis to determine the AC resistance of the LMO material. Hence, the AC resistance, Warburg factor and the diffusion coefficient are observed as 59.65 ohm, 159.65 ohm/S and 1.8 x 10^{-16} cm^{-2}/S, respectively, for the synthesized LMO sample.

5.2.2 Olivine based- $LiFePO_4$ Results

5.2.2.1 Thermal Characterization

In order to achieve the nominal temperature for the decomposition and calcination of the precursors utilized in the sol-gel synthesis process, the thermogravimetric analysis (TGA) of the LFP sample was performed in an inert environment (N_2). Figure 5.7 show the variation in the mass of synthesized sample with respect to temperature.

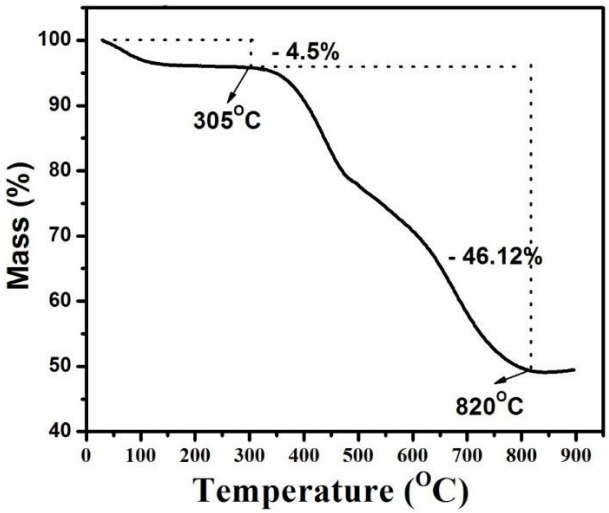

Figure 5.7 *TGA of LFP Sample carried out in inert (N_2) atmosphere at a scan rate of 10 ˚C/minute using Pt crucible.*

In this TGA curve, the two main mass losses were analyzed. The first transition mass loss was appeared between 100 to 350 ˚C (Δ m = 4.5%), which is related to the release of absorbed moisture and also for evaporation of organic compound in the form of different gases as explained in chapter 2. The second transition mass loss appeared at 300 to 825 ˚C (Δ m = 46.12%), which is related to the decomposition of carbon compounds.

The transition mass loss of the synthesized sample (LFP) was stable above 820 ˚C, which directly represents the formation of the olivine phase. Therefore, the TGA curve concludes that the formation of olivine-$LiFePO_4$ phase around 800 to 820 ˚C after decomposition. Hence, the calcination of the LFP sample was performed at 800 ˚C for 24 hrs. in an inert atmosphere after the decomposition.

5.2.2.2 Structural and Morphological Characterization

The XRD characterization of the synthesized LFP sample is shown in figure 5.8. The observed XRD pattern of LFP explores that all the diffraction peak are sharp and crystalline in nature. Hence, strong and sharp peaks are observed in the diffraction angle range of 20 ˚ - 40 ˚ indicating the proper phase and good crystallinity of the synthesized material, which confirms the formation of orthorhombic structure with *pnma* space group.

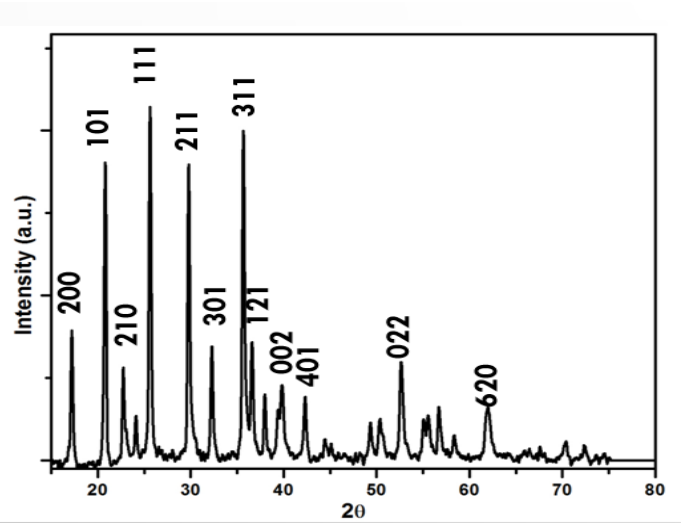

Figure 5.8 *XRD Pattern of Synthesized LFP sample prepared in inert atmosphere.*

The observed pattern of LFP matches well with standard database of XRD pattern, JCPDS - 00 -035-0782-as reference. Therefore, the lattice parameters and atomic positions of observed LFP structure has been reported accordingly. The transition metal in LFP compound i.e. (Fe) occupy the 4c sites and Li occupy the 4a sites at the edges of the octahedral chain. Whereas PO_4 unit shares the edges with two LiO_6 and one FeO_6 octahedral [141-143].

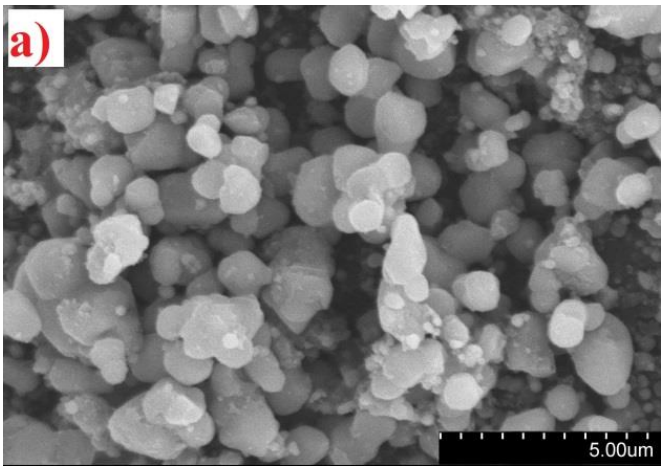

Figure 5.9 *SEM micrographs of LFP sample.*

Furthermore, the morphological characterization of the LFP compound was analyzed using a scanning electron microscope (SEM). It can be analyzed from figure 5.9 that the particle morphology is almost spherical in shape and slightly agglomerated. The grain size of the synthesize LFP sample was lying in the range of 6 to 8 μm.

5.2.2.3 Electrical Characterization

The electronic and ionic conductivity of the LFP compound was measured using the Source Measurement Unit (SMU) as explained in Chapter 2. This characterization revealed the DC conductivity of the synthesized sample using the I-V curve, and this curve gives a linear response reflecting the ohmic response of the compound by electron transport phenomenon. From the figure 5.10, the electrical conductivity of the synthesized LFP sample was plotted and revealed the linear response at varied temperature.

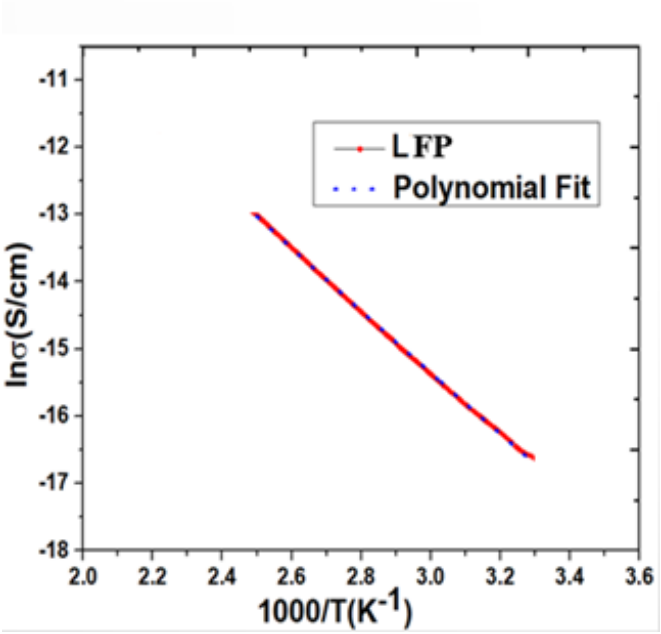

Figure 5.10 *Electronic conductivity (DC) of the LFP sample.*

The conductivity of the LFP sample was 3 x 10^{-9} S/cm and the activation energy was estimated as 707.5 meV. Therefore, the LFP sample was conductive in nature but the researchers need to focus more on improving the conductivity of the LFP sample.

5.2.2.4 Electrochemical Characterization

EIS characterization of the LFP sample has been performed to explore the electrochemical behavior of the cell on the electrode impedance.

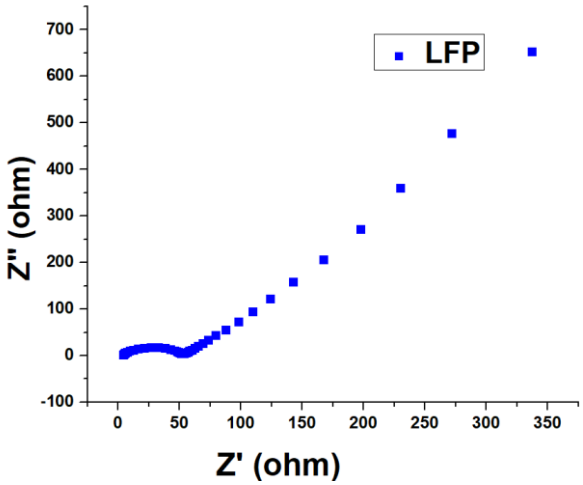

Figure 5.11 *Impedance spectra of LFP synthesized sample in the frequency range of 20 Hz to 1MHz.*

According to the previous chapter 2 explanation, Figure 5.11 displays the EIS curve of the fresh cell for the LFP sample using an AC voltage of 5mV amplitude and a testing frequency that ranges from 20Hz to 1 MHz. Further, the Li-ion diffusion coefficient and Warburg coefficient have also been calculated with the help of equation 2.11 (section 2.3.4.3).

The outcome clearly shows that the LFP sample's charge transfer resistance is 56.4 Ω and the Warburg and diffusion coefficient are 288.85 Ω $s^{-0.5}$ and 1.99 x 10^{-15} cm^2/S, respectively. Hence, it concludes that the ionic conductivity of the sample was lower, and to improve this conductivity, a dual composite cathode material has been synthesized and characterized.

5.2.3 Olivine- Spinel Dual Composite ($LiFePO_4$ - $LiMn_2O_4$)

5.2.3.1 Structural and Morphological Characterization

The XRD pattern of all synthesis samples was characterized in Figure 5.12. The diffraction peaks have been shown to correspond to both pure LFP and LMO compounds with space group C2/m, and the peak position helps to determine phase formation while serving for the assessment of lattice parameters using a standard JCPDS file (JCPDS 00 -035-0782, JCPDS No.-83-2092) is taken for reference.

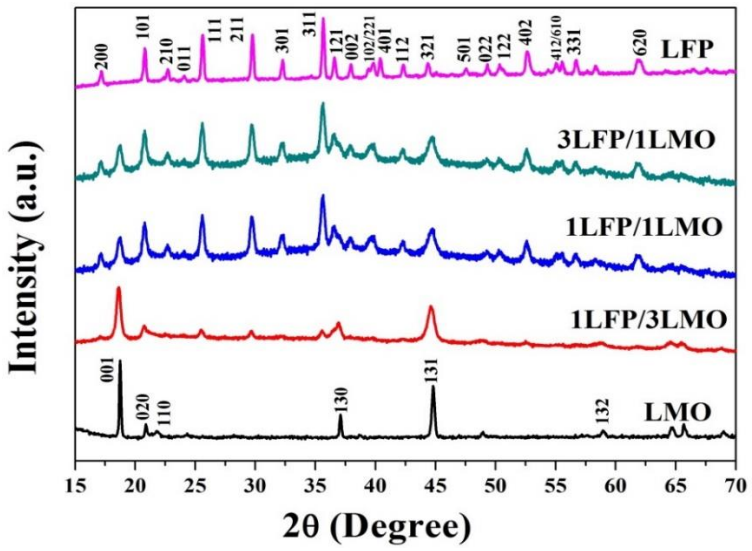

Figure 5.12 *XRD of the synthesized sample at various mass ratios (a) $LiMn_2O_4$ (LMO) (b) 1LFP/3LMO (c) 1LFP/1LMO (d)3LFP/1LMO and (e) $LiFePO_4$ (LFP).*

It was observed from the result that the dual composite of the samples i.e. 3LFP/1LMO, 1LFP/1LMO, and 1LFP/3LMO possess both the phases according to the mass ratio. The LMO structure shows weak diffraction around 20 ˚- 30˚angles, due to the arrangement of Mn ions in the LMO as well as assigned the lattice superstructure into Li-Mn layers. As the ratio of LFP/LMO further increases or decreases, the resultant diffraction pattern may also vary and also reflect the prominent nature of the high-ratio compound. Whereas, the presence of sharp peaks gives confirmation about the crystalline nature of all the compounds in the XRD pattern.

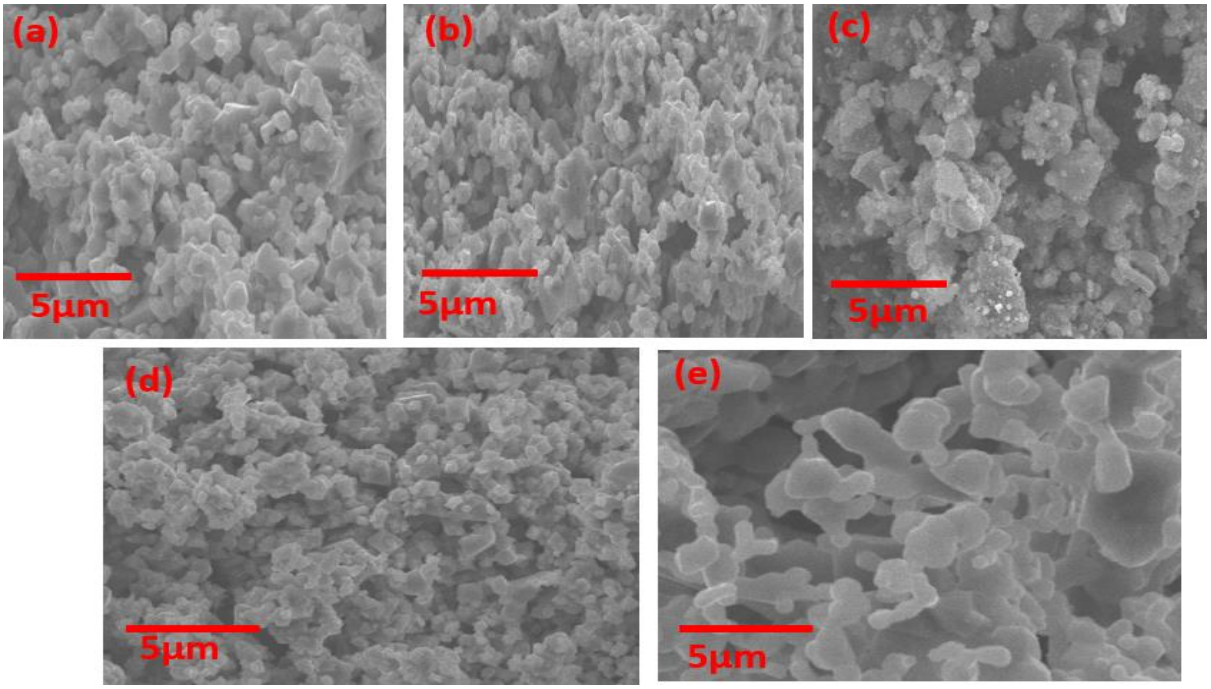

Figure 5.13 *SEM micrographs of the synthesized sample at various mass ratios (a) $LiMn_2O_4$ (LMO) (b) $LiFePO_4$ (LFP) (c) 3LFP/1LMO (d) 1LFP/1LMO and (e) 1LFP/3LMO.*

SEM morphological characterization was performed for all the synthesized samples as well as dual composites. The pristine LFP and LMO have an identical morphology of nearly spherical shape with a grain size of 8-10 µm as shown in figures 5.13 (a) and (b). Furthermore, all the dual composites 3LFP/1LMO, 1LFP/1LMO, and 1LFP/3LMO have different mass ratio concentrations due to which the morphology of the sample was changed as shown in figure 5.13 (c), (d), and (e). The 3LFP/1LMO sample has maximum agglomeration and non-uniformity of the grains and the average grain size of this dual composite is observed as 9 µm. While other two composites 1LFP/1LMO, and 1LFP/3LMO has an average grain size of 8 µm and 7 µm, respectively, with less agglomeration and better distribution of grains.

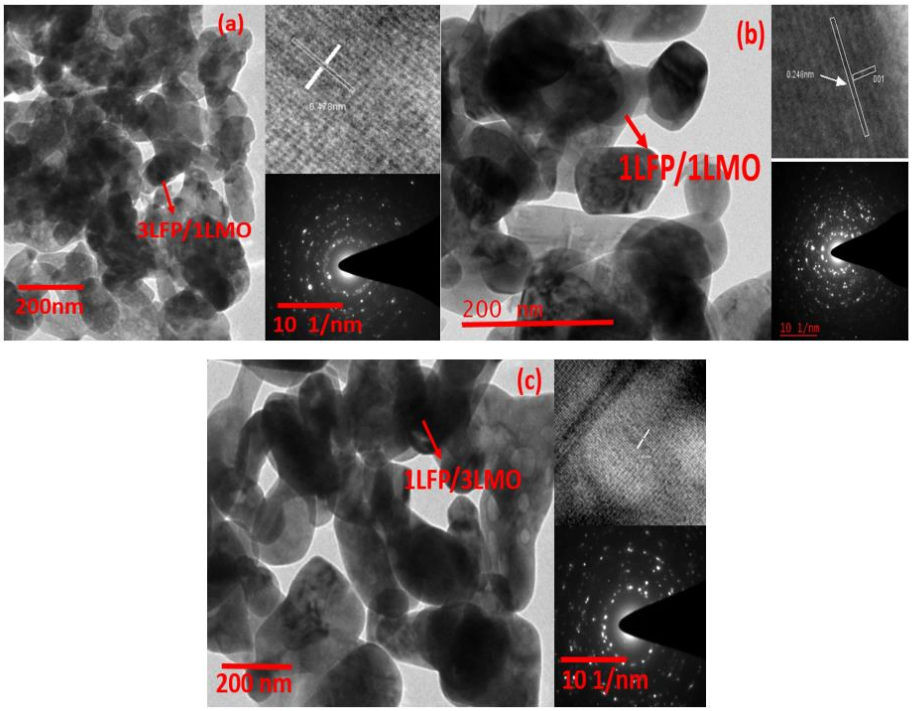

Figure 5.14 *TEM/HRTEM micrographs of the synthesized sample at various mass ratios (a) 3LFP/1LMO (b) 1LFP/1LMO and (c) 1LFP/3LMO.*

Furthermore, the dual composites compound was also chosen to investigate the morphological properties of 3LFP/1LMO, 1LFP/1LMO, and 1LFP/3LMO through TEM/HRTEM characterization as shown in figure 5.14. (a), (b), and (c) respectively. In figure 5.14 (a), the 3LFP/1LMO dual composite reflects that the particles are homogeneously distributed with irregular spherical shapes and more agglomerated with a grain size of 471 nm. Additionally, in figures 5.14 (b) and (c), the dual 1LFP/1LMO and 1LFP/3LMO dual composites are less agglomerated and both the composites possess nearly the same spherical shape structure with the grain size 248 nm, and 210 nm respectively, which was calculated using Image J software. Hence, the obtained results reveal the crystalline nature with uniform space lattices fringes. It has been analyzed that the sample 1LFP/3LMO gives better electrical and electrochemical properties.

5.2.3.2 Electrical Characterization

The electrical conductivity and activation energy of the dual composite samples 3LFP/1LMO, 1LFP/1LMO, and 1LFP/3LMO are shown in figures 5.15 (a) to (f) respectively. From the explored graph, it has been examined that 3LFP/1LMO and 1LFP/1LMO have almost the same conductivity similar to the semiconductor. While in contrast, 1LFP/3LMO is showing superior conductive nature than the other two.

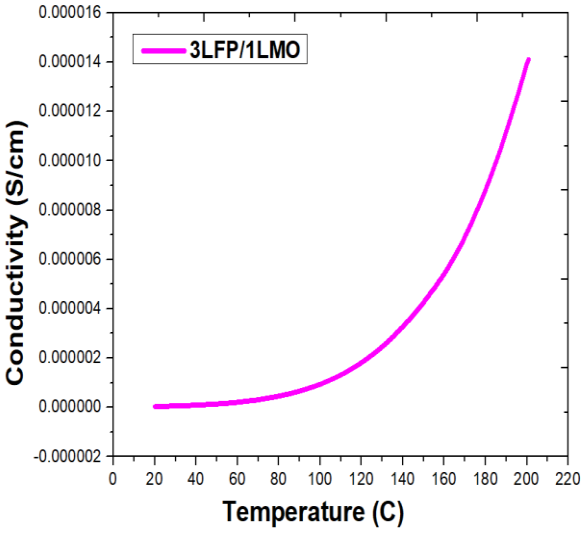

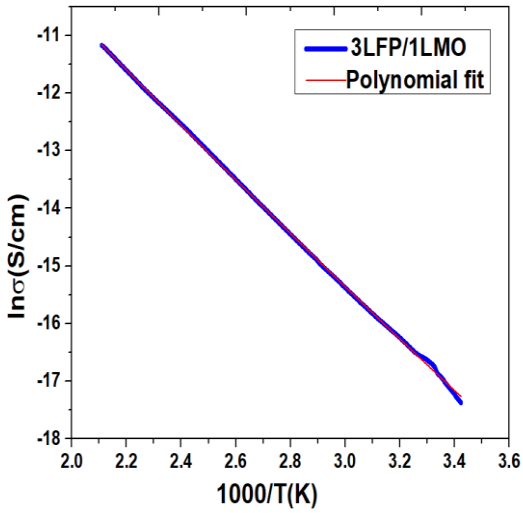

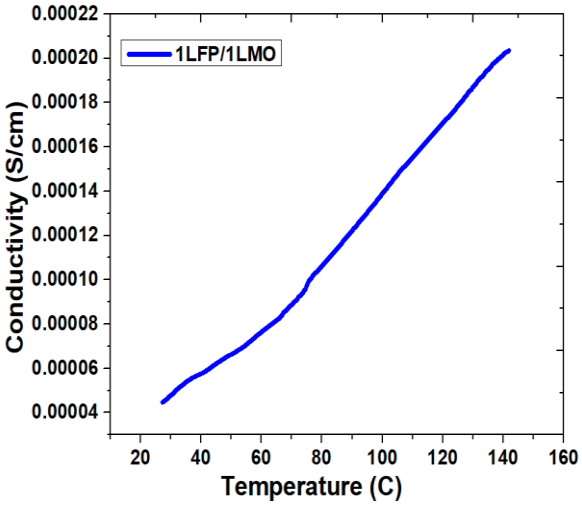

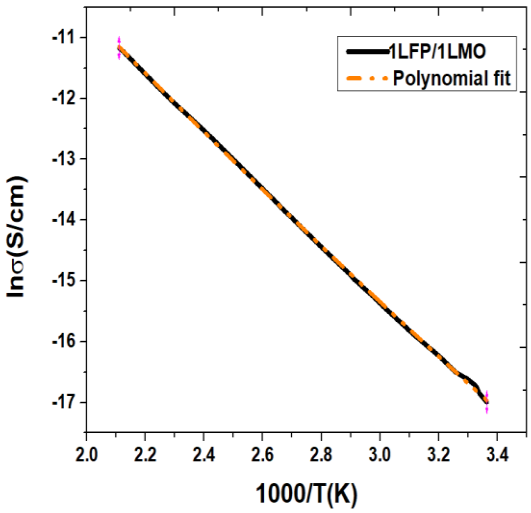

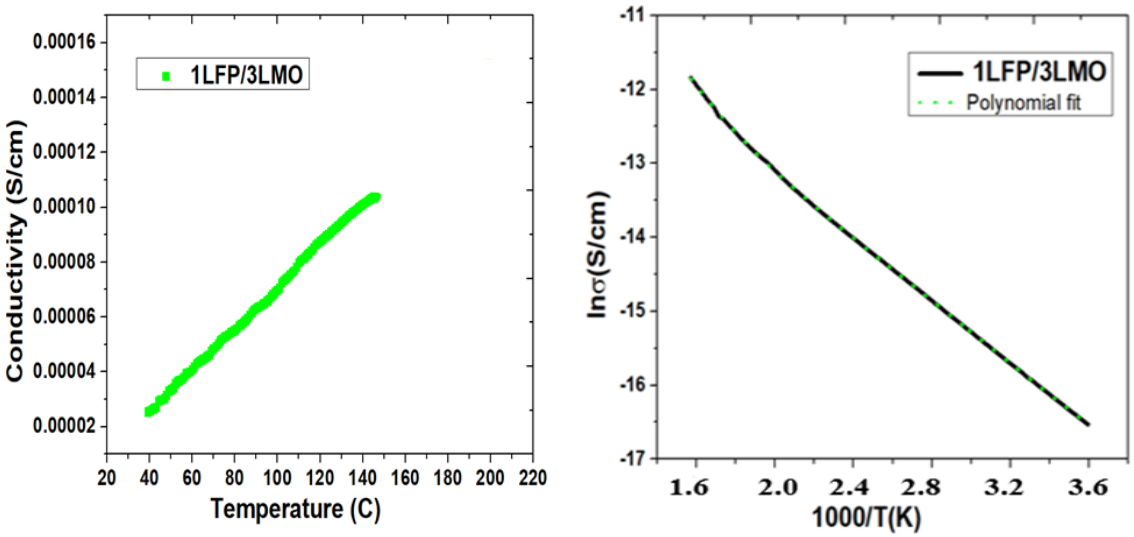

Figure 5.15 *Ionic conductivity and Activation energy measurement of the synthesized dual Composite sample (a) and (b) 3LFP/1LMO (c) and (d) 1LFP/1LMO (e) and (f) 1LFP/3LMO.*

From the Table 5.2, the value of DC resistance, R_{DC} (Ω); conductivity, σ(S/cm), and activation energy of all the synthesized dual composite samples were summarized at the variation of temperature from 25 ˚C to 200 ˚C.

Table 5.2*. Activation energy with conductivity measurements of dual composites.*

Sample	R_{DC}(Ω)	σ_{dc}(S/cm)	E_a(±10) (meV)
3LFP/1LMO	1.2×10^{6}	7.92×10^{-7}	380.92
1LFP/1LMO	2.24×10^{4}	4.47×10^{-7}	340.21
1LFP/3LMO	3.52×10^{2}	2.84×10^{-4}	98.72

Hence, it has been observed that 1LFP/3LMO are more dominant and conductive by the order of 10^{-4}, this huge difference in the conductivity may also help to change the activation energy of the sample. It can also be analyzed from the curves that with decrease in LFP mass ratio results increase in conductivity and also attains maximum value for 1LFP/3LMO sample. The possible reason are not known but it could be due to the spinel material more mass ratio. The

1LFP/3LMO shows the enhanced activation energy among all the dual composites. Further, the electrochemical impedance was measured using coin-cells of all the synthesized samples and the fabrication of coin cell assembly is already discussed in chapter 2 (Section 2.3.4.1).

5.2.3.3 Electrochemical Characterization

The EIS characterization was plotted to examine the variation in electrode impedance on the fresh half-coin cells using standard CR2032, using a 5 mV amplitude and frequencies between 20 Hz and 1 MHz at ambient temperature. Figure 5.16 demonstrates that the straight line is in the low-frequency range while the semicircle's crossings are all in the high-frequency region.

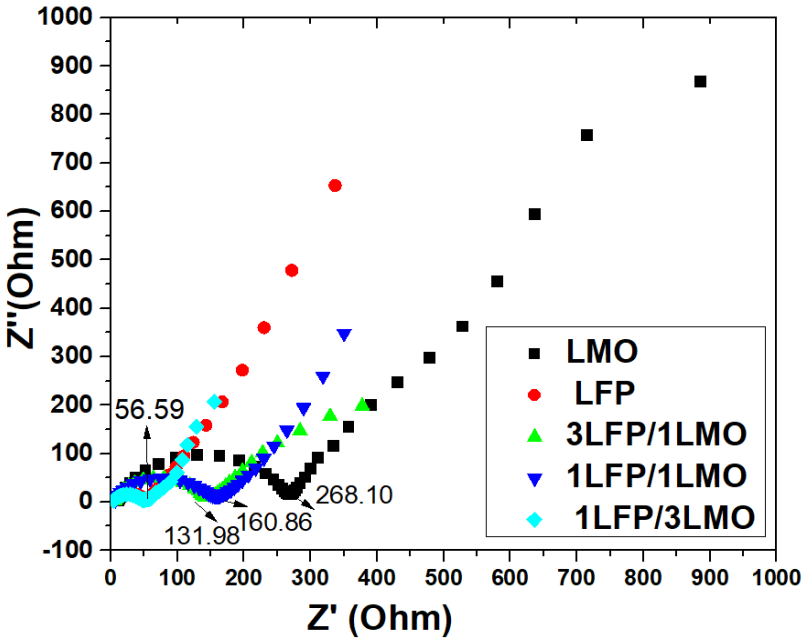

Figure 5.16 *Electrochemical impedance curves of prepared compositions observed for AC pulse of 5 mV amplitude.*

This semicircle is mainly due to the electrochemical reaction between the electrolyte and the electrodes. The intersection points obtained on the x-axis represent the ohmic resistance (R_s) of the cell and directly represent the charge transfer resistance of the electrode. As shown in figure 5.16, the maximum charge transfer resistance (R_{ct}) is analyzed on the LMO sample whereas for 1LFP/3LMO and 1 LFP/1LMO having nearly equal charge transfer resistance i.e. 140.76 Ω and 161.38 Ω respectively. Similarly, the 3LFP/1LMO and LFP shows equal charge

transfer resistance i.e. 52.08 Ω. After evaluating the change in the Rct value, this shows the change in the ionic conductivity of all samples.

Table 5.3 *Diffusion Coefficient of all the dual composite synthesized samples.*

Synthesized Sample	**R_{ct}(Ω)**	**σ_w(Ω /S)**	**D (cm^2/S)**
3LFP/1LMO	140.76	150.87	3.26×10^{-13}
1LFP/1LMO	161.38	180.60	4.21×10^{-14}
1LFP/3LMO	52.08	48.89	4.85×10^{-12}

The diffusion coefficient for all the dual composites was also calculated using the standard equation as already described in the chapter 2 [section 2.3.4.3]. Table 5.3 makes it clear that, out of all the dual composite samples, the synthesized 1LFP/3LMO dual composite has the lowest charge transfer resistance and the maximum diffusion coefficient.

Figure 5.17 represents the cyclic voltammetry (CV) results of the synthesized dual composites 3LFP/1LMO, 1LFP/1LMO, and 1LFP/3LMO, respectively. The voltage window and scan rate for CV characterization were between 2 V to 4.5 V and 0.05 ms^{-1}, respectively. It is reveal from the cv results that the highest anodic peak is around 3.16 V, 3.13 V, and 3.09 V respectively and shoulder peaks are nearly at 4.03 V, 4.04 V, and 4.042 V respectively. Both the peaks are present due to the presence of LMO in all the composite compounds.

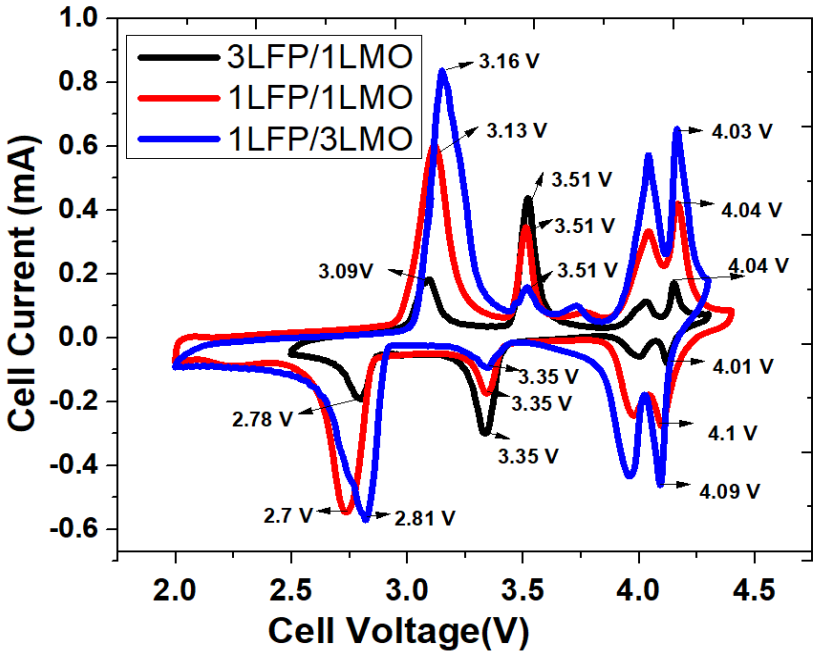

Figure 5.17 *Cyclic Voltammograms of the dual composites at 0.05 mVs^{-1} scan rate at room temperature.*

Similarly, the anodic and cathodic peak is around 3.5 V and 3.35 V respectively and both oxidation and reduction peak is having symmetrical behavior due to the transient reaction between $Fe^{3+}$and Fe^{2+} [144-150]. Different anodic and cathodic peaks were found resulting from the Li-ion intercalation at octahedral sites in the spinel configuration from the MnO_2 presence LMO compound in the dual composites. As the mass ratio of the LMO compound increases, the peak range during the cathodic and anodic reactions also further increases. Due to the lattice oxygen in the form of Li_2O from the monoclinic crystal structure, the symmetry across the peaks was weak. Therefore, the CV results confirmed the co-occurrence of olivine as well as the spinel structure in the dual composites as already indicated by XRD results. Initial charge-discharge capacity curves for dual composites are shown in Figure 5.18 for a current density of 10 mA/g in the voltage range of 2.5 V to 4.5 V.

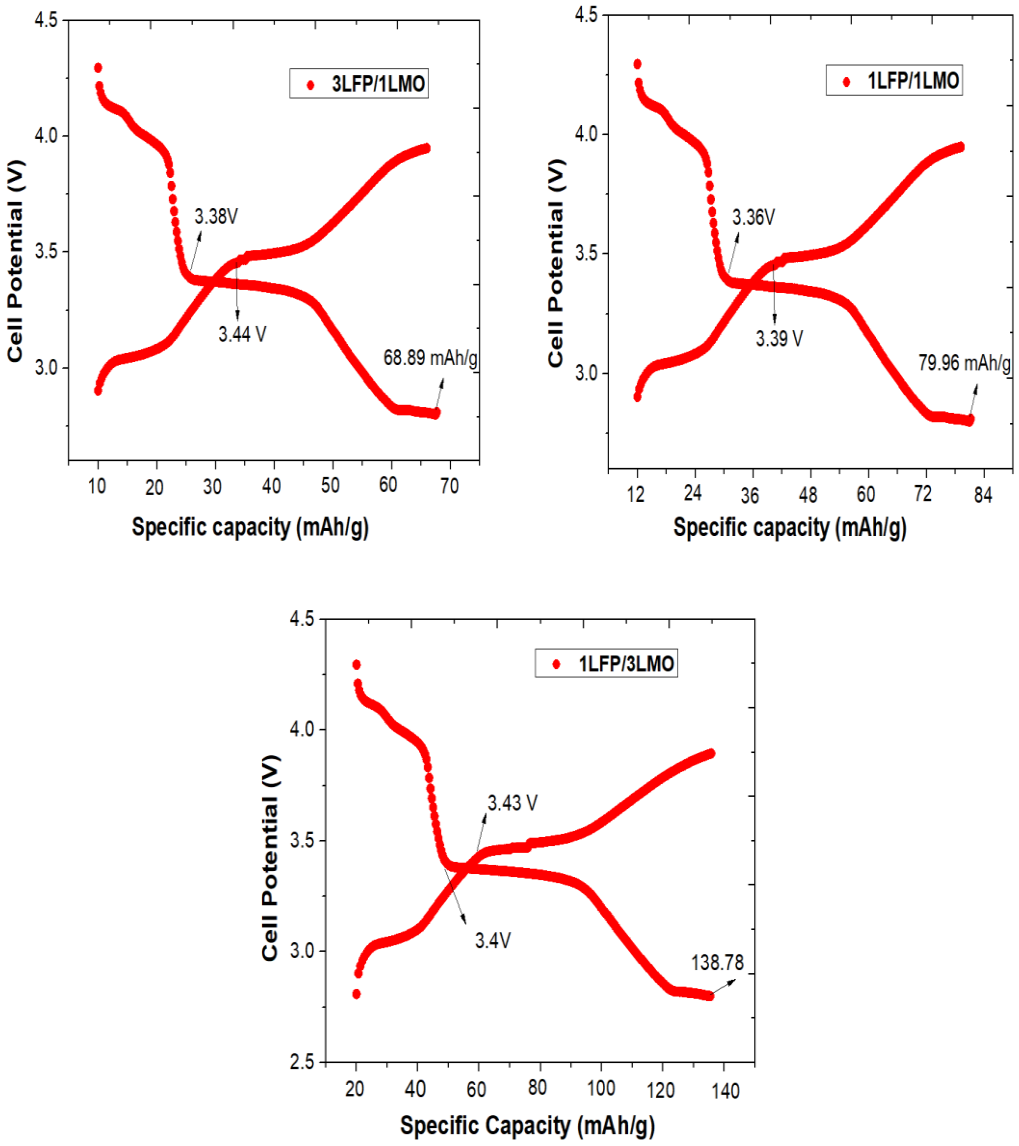

Figure 5.18 *Galvanostatic charge discharge (GCD) curve of the Dual Composites synthesized samples 3LFP/1LMO, 1LFP/1LMO and 1LFP/3LMO, respectively.*

The initial discharge capacities for dual composites 3LFP/1LMO, 1LFP/1LMO, and 1LFP/3LMO were found to be 68.89 mAh/g, 79.96 mAh/g and 138.78 mAh/g respectively. For all the dual composites, the discharge plateau can be analyzed just above the 3.4 V in the discharge curve whereas the slope can be seen at 3.3 V on a charge profile.

Chapter 6: Enhanced Electrical characterization monitored on Hardware test bench with real-time software for Lithium-ion Battery.

The battery test bench is described in this chapter and used to evaluate the electrical characteristics of lithium-ion coin cell battery pack. Hardware circuits are used to test the electrical properties. In order to gather real-time data and display battery-related information such as voltage and load curves, these electrical tests have been carried out on the data acquisition programme. In order to improve the battery characteristics, a parallel connection between the capacitor bank and the battery bank has also been made, as well as an external short circuit test performed.

6.1 Introduction

As discussed in section 1.6 of chapter 1 that to study the electrical characterization of the coin cell battery bank, a simple hardware prototype has been designed with the help of simple electronic components. With the use of data collecting software, a lithium-ion coin cell has been coupled to a circuit for optimizing the discharge curves.

This coin cell was fabricated with the help of dual composite cathode material (1LFP/3LMO) in a research laboratory as discussed in previous chapter 5(section 5.2.2.3) and used to develop a battery bank. In this coin cell, a synthesized cathode material was used to develop a half coin cell assembly, and this coin cell was connected in series and parallel to develop a battery bank. However, a battery bank was connected with a hardware prototype for electrical characterization. This hardware was interfaced with software through the NI-6001 DAQ card and the results were optimized with the help of data acquisition software[151]. The main focus of this experiment is to optimize the electrical characteristics such as battery voltage and current during discharge conditions and also perform battery external short circuit tests.

6.2 Hardware Circuit Diagram

For optimizing the electrical characteristics, the following equipment were used to develop a hardware circuit such as a battery bank of six coin cell that are connected in series and parallel, multiple resistance of various range 0-500 Ω, DC motor using a variable load, capacitor bank connected parallelly, multiple switches, wires, PCB, and other monitoring instruments[151-152].

6.2.1 Experiment setup

A hardware prototype was used for three electrical tests in which different types of discharge curves have been optimized. In figure 6.1, three different circuit diagrams are demonstrated for

electrical characterization. Firstly, a short circuit test has been performed and figure.6.1 (a) demonstrates the circuit diagram in which switch SW1 is closed for measuring the battery potential and current across the terminal with the help of the NI DAQ card.

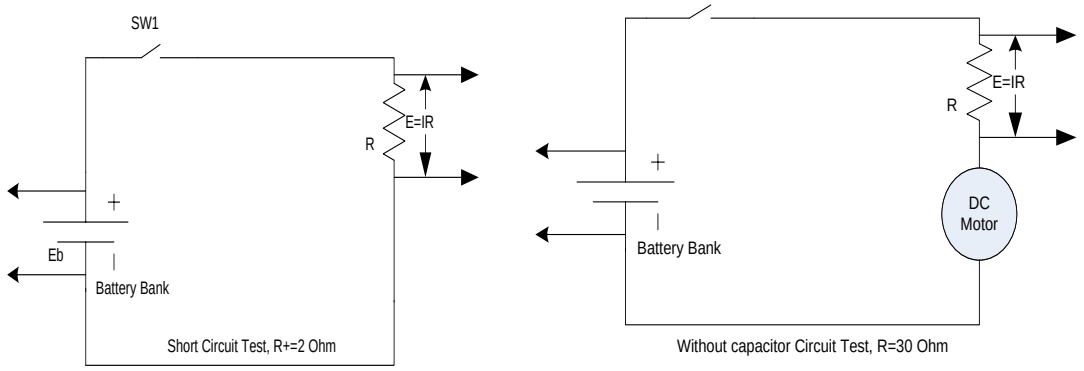

a) Short circuit test b) Battery without capacitor bank

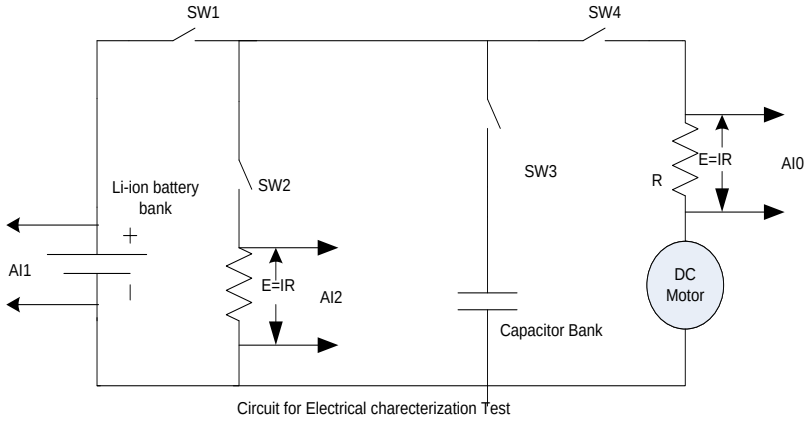

c) Hybrid Combination of a battery bank and Capacitor Bank

Figure 6.1. *Circuit for Hardware design: (a) Circuit for Short Circuit Test, (b) Circuit Design for battery without capacitor bank and (c) Circuit for the hybrid combination of battery and capacitor bank.*

Secondly, a switch SW2 is closed and the DC motor was connected across it as load and the potential and current of the battery bank were monitored as shown in the figure.6.1 (b). In this circuit, a capacitor bank was not connected across the battery bank. Lastly, a hybrid combination of both capacitor bank, as well as battery bank, were connected across the load.

When the capacitor bank is connected in parallel across the circuit and switches SW1, SW3, and SW4 are closed to monitor the battery properties, voltage and current discharge curves were measured as depicted in the figure. 6.1 (c).

In this hardware, when the battery supply is ON and the voltage starts flowing across the variable resistor terminal then two terminal of NI DAQ card was connected and read the data across it. Further, this DAQ card makes a connection with the PC for analyzing data with software[153-154].

This is a real-time simulation software in which hardware and software are interfaced with one another. There are many in-built functions in this software that helps for analyzing data such as communication links, electronic functions, mathematical functions and many more [154-158]. There are two panels in the software i.e. front panel that helps for interfacing between hardware and software whereas other is VI panel that helps for modification in the virtual instrument. Figure.6.2 represents the VI panel of the software in which the program has been developed for analyzing the data of the hardware prototype.

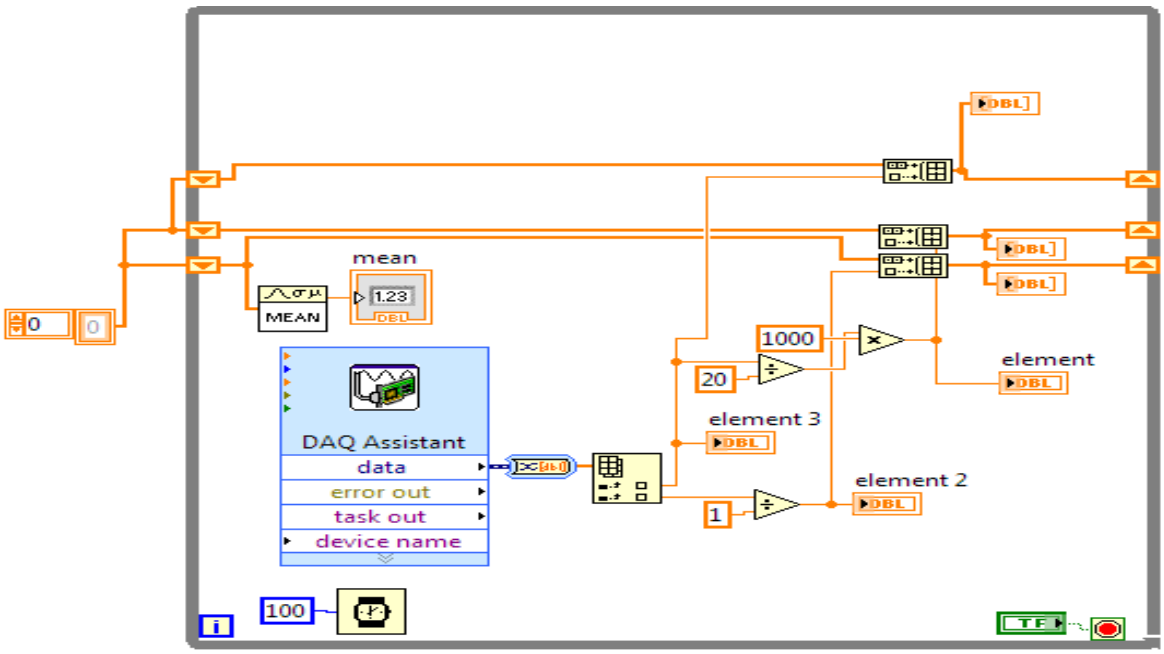

Figure.6.2 *VI Front Panel Program for Hardware Prototype.*

Now, a hardware setup was developed with a 2032-coin cell of $LiMn_2O_4$ material as well as a capacitor bank. Figure.6.3 demonstrates the hardware prototype for electrical testing and discharge curves were obtained on the front panel.

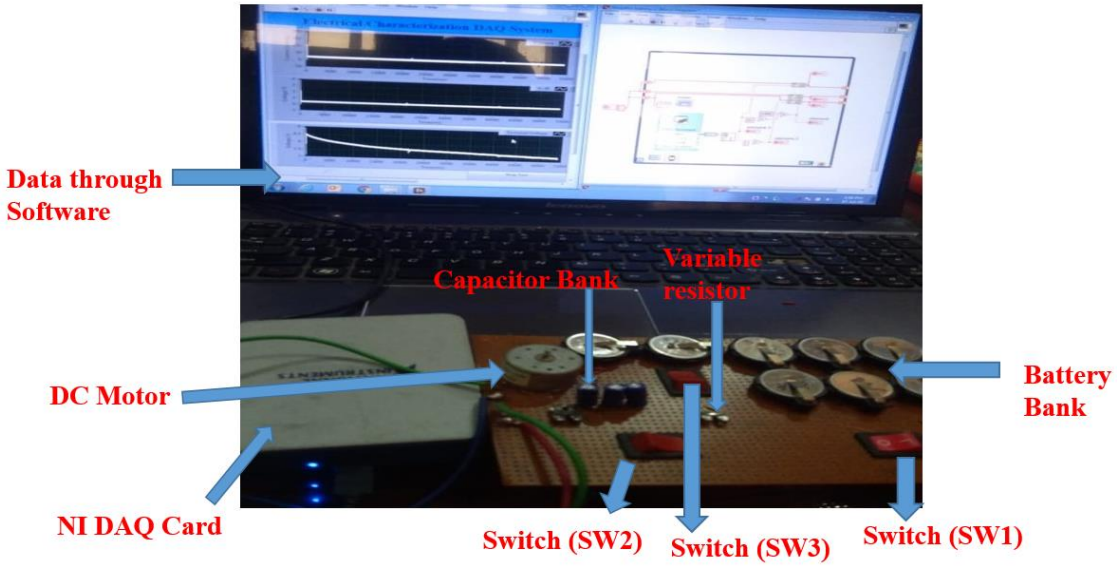

Figure.6.3. *Hardware Prototype for Electrical Testing.*

Moreover, in this study, both the hardware and simulation setup was developed for optimizing the battery characteristics.

6.3 Results and Discussion

For the characterization and analysis, a hardware prototype was connected through the NI-DAQ card and interfaced with data acquisition software for obtaining real-time data. Three different tests have been performed in this characterization to track the electrical performance of the battery bank: a short circuit test, a battery bank connected in parallel with a load without a capacitor bank, and finally, a battery bank connected in parallel with a capacitor bank to boost battery efficiency.

6.3.1 Short Circuit (SC) Test

In this test, an electrical circuit has been connected to evaluate the battery bank characteristics as already explained in figure 6.1. (a). Short circuit tests have been carried out since they can

pose serious problems for real-time applications because they result in excessive overheating, a sharp drop in voltage, and high discharge current.

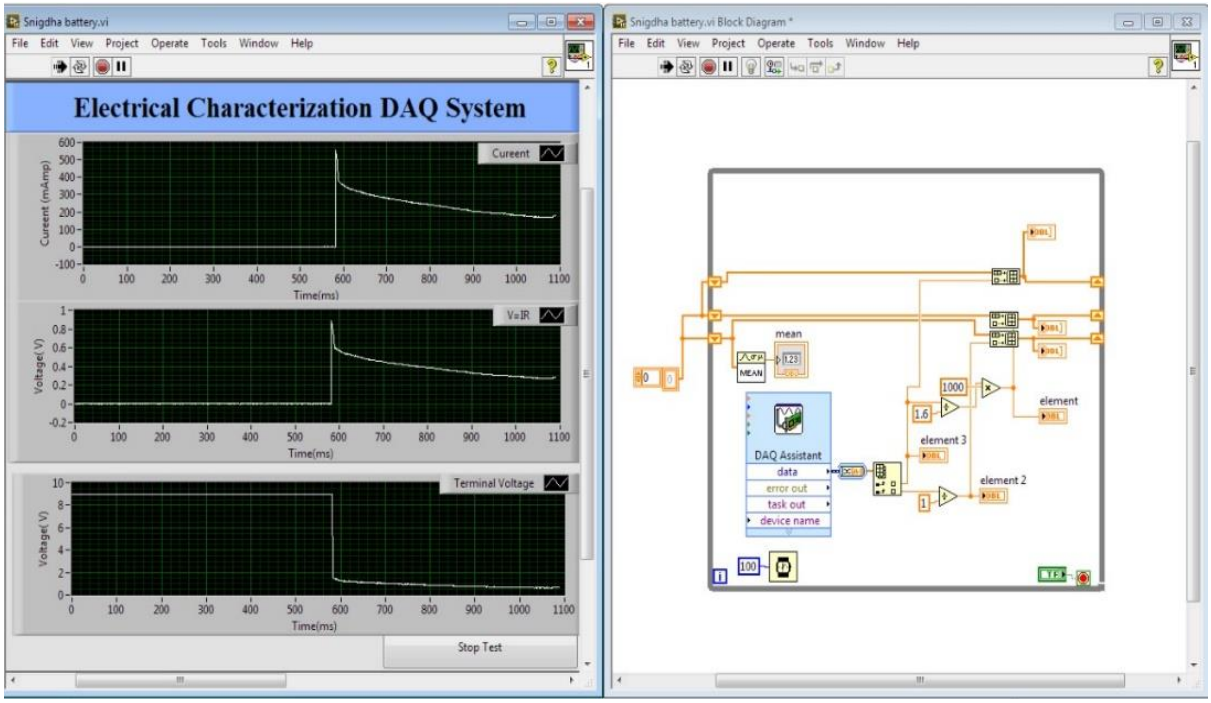

Figure. 6.4. *Short circuit test on coin-cell battery bank to evaluate the short circuit current.*

Figure 6.4 represents the short circuit test characteristics across the hardware prototype. During this test, there is a sudden rise in the current of 515 mA takes place and similarly, there is an increment in voltage drop of 0.85 V across the resistor of 1.5 Ω in the circuit. Hence, there would be a sudden rise in current due to short circuit tests across the battery bank which would help to know the high discharge current across the circuit.

6.3.2 Test on load without Capacitor Bank

In this test, the battery bank has been connected directly to the load (motor) for obtaining the discharge characteristics of the battery. When the capacitor bank is not connected to the circuit, Figure.6.5 depicts the discharge curve of the battery bank. The resistor terminal is tested with

the current increased to 80mA and then held steady at 20mA. Similarly, the battery bank potential is 4.7 V and the potential drop over the 24 resistor is 0.5V.

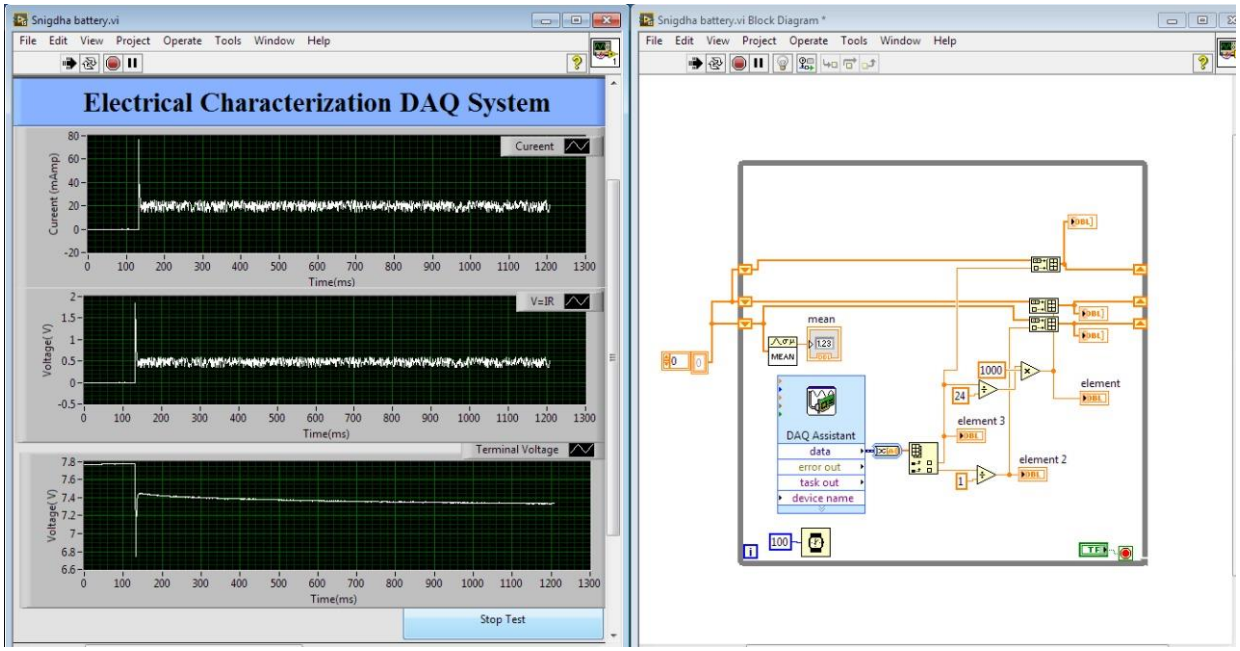

Figure 6.5. *Current and Voltage Waveform without Capacitor Bank.*

But, there is a lot of fluctuation in the waveform, which represents a lot of noise in the circuit as represent in the figure 6.5. Hence, to overcome this fluctuation in the circuit, a capacitor bank has been connected parallel in the circuit.

6.3.3 Test on load with Capacitor Bank

During this test as circuit already explained in figure 6.1. (c). this circuit helps to increase battery efficiency, a capacitor bank was created by connecting three 220 microfarad capacitors in parallel. This capacitor bank was then linked in parallel with a battery bank and a DC load.

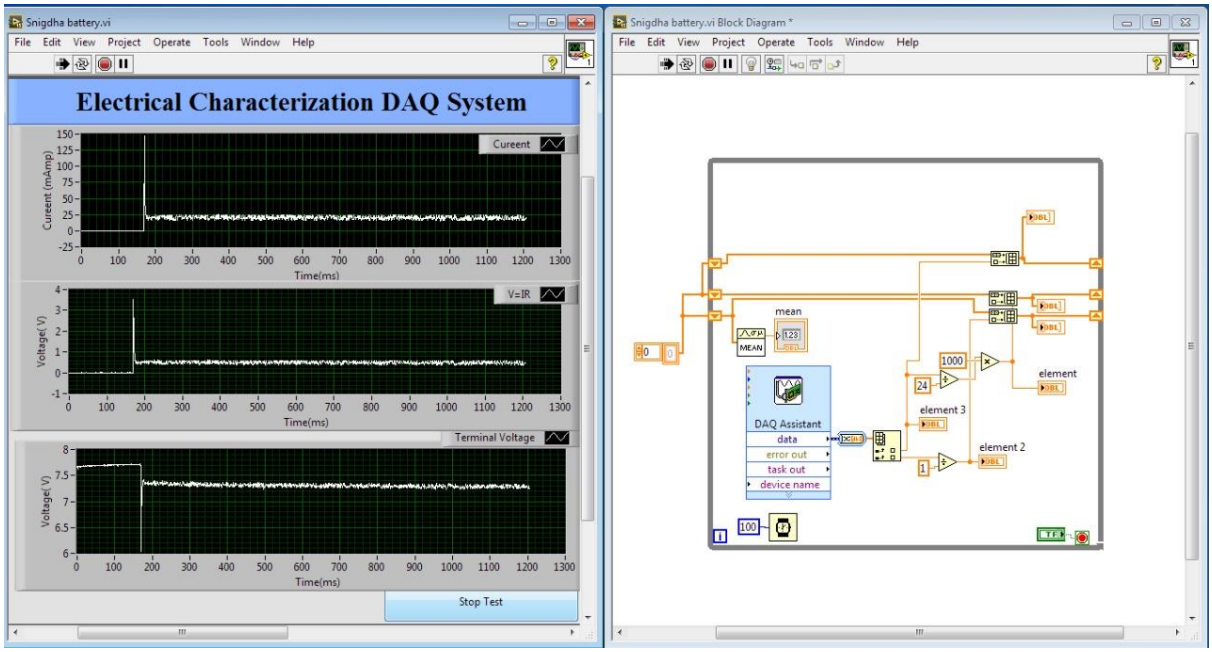

Figure 6.6. *Current and Voltage Discharge Waveform with Capacitor Bank.*

In this test, we optimized the fact that when a capacitor is connected across a battery, a high accelerating current flows through the circuit until it stabilize at 25 mA. The 7.4V measured voltage was the same throughout the battery bank. Therefore, it has been determined that a capacitor bank would supply the increased current across the load.

Chapter 7: Conclusion and Suggestions for Future work

This chapter summarizes the brief conclusion of all the results obtained during this research study along with the introduction of future work.

7.1 Conclusion

In this research work, a comprehensive investigation of the cathode materials spinel and olivine was carried out using theoretical simulation and experimental methods. First, both spinel (LMO) and olivine (LFP) cathode materials were simulated and then experimentally synthesized individually. Then, the dual olivine-spinel composite was simulated and synthesized with different molar ratios for the evaluation of the electrochemical, thermal, and electrical properties.

The computational model for both the spinel and the olivine cathode material was simulated and analyzed under various optimized conditions. Firstly, the spinel-type (LMO) cathode material shows the improved electrochemical characterization after controlling the internal parameters of the designed battery. During the thermal simulation at various temperatures, no hot spot was formed across the cell boundary and the polarization voltage was very small about 0.3V, which would be considered as a negligible internal resistance across the cell. In addition, LMO/graphite displays 96% of discharge capacity of its full state of charge (SOC) at 10C-rate as compared to different anode material. Secondly, the olivine-type (LFP) cathode material exhibits the good electrochemical behavior of the cell at various frequency regions, as well as shows proper charging and discharging behavior with low ohmic and concentration losses across the cell. During the thermal simulation, the surface resistant behavior was evenly distributed at high temperature, showing better stability in the cathode material.

The intercalation study of two cathode materials was formed to evaluate the performance of dual olivine-spinel composite cathode material with different molar ratio. The simulation of the composite proves the addition of two intercalation materials in different molar ratios due to the change in lithium ion concentration in their electrochemical reactions. Therefore, among

all the different molar ratio formations, the 1LFP/3LMO shows a good voltage profile curve at a 1C rate. The thermal management across this battery pack was also stable.

After computation modeling, the experimental characterization of the synthesized spinel (LMO), olivine (LFP), and olivine- spinel (LFP-LMO) dual composite was investigated. The experimental results of the spinel, $LiMn_2O_4$ (LMO) cathode material reveals the sharp and intense peaks with the homogeneous morphological structure with an average grain size of 8-10 μm and also evaluate the ionic conductivity in 4.42 $x10^{-8}$ S/cm. Similarly, the olivine-based $LiFePO_4$ (LFP) material reveals the crystalline peak with orthorhombic structure and an average grain size of 5-6 μm. The ionic conductivity with the activation energy was obtained $3.7x10^{-9}$ S/cm, as well as also the diffusion coefficient of 1.99 x 10^{-15} cm^2/s was determined.

However, in the above experimental results, the ionic conductivity of the synthesized sample had a higher priority because novel olivine-spinel dual composite cathode materials ($LiFePO_4$ - $LiMn_2O_4$) with different molar ratios were synthesized to improve the ionic conductivity. This dual composite was mixed in a different compound ratio such as 3LFP/1LMO, 1LFP/1LMO, and 1LFP/3LMO to form two intercalation active materials. In this, olivine-spinel dual composites, i.e. $LiFePO_4$-$LiMn_2O_4$ were successfully synthesized. The existence of olivine and spinel structure is demonstrated by XRD data. Microstructural analyses show that all of the samples exhibit a blend of smaller and larger grains with essentially the same shape. Among all the arrangements, 1LFP/3LMO shows the best performances. It delivers an initial specific discharge capacity of 138±75 $mAhg^{-1}$ with good ionic conductivity of 2.84 x 10^{-4} S/cm. Among all the simulated and synthesized samples, the novel olivine-spinel (1LFP/3LMO) dual composite shows the best electrochemical, thermal, and electrical performances. Hence the optimized experimental results of dual composite, 1LFP/3LMO are well supported by theoretical simulation.

Furthermore, for exposition of coin-cells on hardware platform, a hardware prototype for testing a lithium-ion coin cell battery packs were developed for evaluating the electrical characterization and application point of view. Hardware setup was used to test the battery bank on electrical load with and without capacitor bank. As capacitor bank represent that it helps to increase the surge current from 80 mA to 150 mA for the DC load and also remove harmonics in the current waveform.

7.2 Scope of Future Studies

Based on the work carried out in the present thesis, some suggestions for future work include:

- In the present thesis, all the studies and investigations have been carried out using solid solutions. Hence, in the future work an effort will be made by different deposition techniques such as, sputtering, pulse laser deposition, thermal evaporation, etc.
- Study the effect of different olivine structure such as $LiFe_{1-x}Ni_xPO_4$ / ZnO doped/ Carbon Coating.
- Test a composite material for a high Voltage Battery Pack with the help of cylindrical cell for commercial applications.
- An effort will be made to enhance the energy storage capacity of Olivine-Spinel composites for the possible application in the field of high energy storage capacitors.
- Modify a hardware system for high voltage application with the help of BMS, Chargers and load banks.

REFERENCES

[1] Chan, C., 1993. An overview of electric vehicle technology. Proceedings of the IEEE 81(9), 1202-1213.

[2] Chan, C., 1999. Engineering philosophy of electric vehicles. In: IEEE International Electric Machines and Drives Conference, Seattle, 1999.

[3] Chan, C., 2002. The state of the art of electric and hybrid vehicles. Proceedings of the IEEE 90, 247-275.

[4] Chan, C., 2003. Advances in electric vehicles. HKIE Transactions 10(4), 1-13.

[5] Chan, C., Chau, K., 1997. An overview of power electronics in electric vehicles. IEEE Transactions on Industrial Electronics 44, 3-13.

[6] Chen, S., Dai, F., Gordin, M.L., et al., 2013. Exceptional electrochemical performance of rechargeable Li–S batteries with a polysulfide-containing electrolyte. RSC Advances 3, 3540-3543.

[7] Arora, P., 2000. Comparison between computer simulations and experimental data for high-rate discharges of plastic lithium-ion batteries. Journal of Power sources, 88(2), 219-231.

[8] Chen, 2010.Porous cathode optimization for lithium cells: Ionic and electronic conductivity, capacity, and selection of materials. Journal of Power Sources, 195 (9), 2851-2862.

[9] Marincas, 2020. Review on Synthesis methods to obtain LiMn2O4-based cathode materials for Li-ion batteries. Journal of Solid State Electrochemistry, 24 (3), 473-497.

[10] Marincas, 2021. Enhancing Lithium Manganese Oxide Electrochemical behavior by doping and surface modifications. Coatings, 11(4), 456.

[11] Gallagher, K.S., Muehlegger, E., 2011, Giving green to get green? Incentives and consumer adoption of hybrid vehicle technology. Journal of Environmental Economics and Management 61, 1-15.

[12] Wu, H., Niu, D., 2017. Study on influence factors of electric vehicles charging station location based on ISM and FMICMAC. Sustainability 9(4), 484-503.

[13] Xia, W., Mahmood, A., Zou, R., et al., 2015. Metal-organic frameworks and their derived nanostructures for electrochemical energy storage and conversion. Energy & Environmental Science 8, 1837-1866.

[14] Elliott, D., Cook, T., 2018. Renewable Energy: from Europe to Africa. Springer, Berlin.

[15] Conway, B.E., 2013. Electrochemical Supercapacitors: Scientific Fundamentals and Technological Applications. Springer, Berlin.

[16] Shen, C., Shan, P., Gao, T., 2011. A comprehensive overview of hybrid electric vehicles. International Journal of Vehicular Technology 2011(S1), 1-7.

[17] Shen, P.K., Wang, C.Y., Jiang, S.P., et al., 2016. Electrochemical Energy: Advanced Materials and Technologies. CRC Press, Boca Raton.

[18] Bockris, J.O., 1981. Electrochemistry and the 21st Century. In: Bockris, J.O., Conway, B.E., Yeager E. (Eds.), Comprehensive Treatise of Electrochemistry. Springer, Boston, pp. 1-38.

[19] Wendt, H., Kreysa, G., 2013. Electrochemical Engineering: Science and Technology in Chemical and Other Industries. Springer, Berlin.

[20] Broussely, M., Pistoia, G., 2007. Industrial applications of batteries: from cars to aerospace and energy storage. Elsevier, Amsterdam.

[21] Zoski, C.G., 2006. Handbook of Electrochemistry. Elsevier, Amsterdam.

[22] Thomas, B., 2010. Linden's Handbook of Batteries. McGraw-Hill Book, New York.

[23] Thomas, B. F., (Google Patents, 1955).

[24] Bullock, K.R., 1994. Lead/acid batteries. Journal of Power Sources 51, 1-17.

[25] Pistoia, G., 2008. Battery Operated Devices and Systems: from Portable Electronics to Industrial Products. Elsevier, Amsterdam.

[26] Huggins, R.A., 2010. Energy Storage. Springer, Berlin.

[27] Shukla, A., Venugopalan, S., Hariprakash, B., 2001. Nickel-based rechargeable batteries. Journal of Power Sources 100, 125-148.
[28] Sadoway, D.R., Mayes, A.M., 2002. Portable power: advanced rechargeable lithium batteries. MRS Bulletin 27, 590-596.
[29] Zimmerman, A.H., 2009. Nickel-Hydrogen Batteries: Principles and Practice. Aerospace Press, Washington DC.
[30] Goodenough, J.B., 2012. Evolution of strategies for modern rechargeable batteries. Accounts of Chemical Research 46, 1053-1061.
[31] Goodenough, J.B., Kim, Y., 2009. Challenges for rechargeable Li batteries. Chemistry of Materials 22, 587-603.
[32] Yuan, Z., Peng, H.J., Hou, T.Z., et al., 2016. Powering lithium-sulfur battery performance by propelling polysulfide redox at sulfiphilic hosts. Nano Letters 16, 519-527.
[33] Zhao, Q., Hu, X., Zhang, K., et al., 2015. Sulfur nano-dots electrodeposited on Ni foam as high-performance cathode for Li–S batteries. Nano Letters 15, 721-726.
[34] Whittingham, M.S., 2004. Lithium batteries and cathode materials. Chemical Reviews 104, 4271-4302.
[35] Bruce, P.G., Hardwick, L.J., Abraham, K., 2011. Lithium-air and lithium-sulfur batteries. MRS Bulletin 36, 506-512.
[36] Amine, K., Kanno, R., Tzeng, Y., 2014. Rechargeable lithium batteries and beyond: progress, challenges, and future directions. MRS Bulletin 39, 395-401.
[37] Peng, H.J., Huang, J.Q., Cheng, X.B., et al., 2017. Review on high-loading and high-energy lithium-sulfur batteries. Advanced Energy Materials 7, 170-260.
[38] Su, Y.S., Manthiram, A., 2012. Lithium-sulfur batteries with a microporous carbon paper as a bifunctional interlayer. Nature Communications 3, 1166.
[39] J. Yuan, X. Liu, H. Zhang, Lithium-ion batteries: advanced materials and technologies, CRC Press, 2011.
[40] A. Patil, V. Patil, D.W. Shin, J.-W. Choi, D.-S. Paik, S.-J. Yoon, Mater. Res. Bull., 43 (2008) 1913-1942.
[41] J.F. Rohan, M. Hasan, S. Patil, D.P. Casey, T. Clancy, Intech, 2014.
[42] R. Koksbang, J. Barker, H. Shi, M. Saidi, Solid State Ionics, 84 (1996) 1-21.
[43] J. Tarascon, D. Guyomard, G. Baker, J. Power Sources, 44 (1993) 689-700.
[44] Rewatkar, M.R., and D.Z.Shende. 2020. Experimental investigation on cenosphere-based paper battery. Energy Sources, Part A: Recovery, Utilization, and Environmental Effects, 42(16), 2018-2033.
[45] Qin, J., S. Zhao, X. Liu, and Y.Liu. 2020. Simulation study on thermal runaway suppression of 18650 lithium battery. Energy Sources, Part A: Recovery, Utilization, and Environmental Effects,1-13.
[46] Chakraborty,A., S. Kunnikuruvan, S.Kumar, B. Markovsky, D.Aurbach, M.Dixit, D.T.Major. 2020. Layered Cathode materials for lithium-ion Batteries: review of computational studies on $LiNi_{1-x-y}CO_xAl_yO_2$. Chemistry of Materials, 32 (3): 915-952.
[47] Baena-Moreno, F.M., M. Rodriquez-Galan, F.Vega, B. Alonso-Farinas, L.F. Vilches Arenas, and B. Navarrete. 2019. Carbon capture and utilization technologies: a literature review and recent advances. Energy Sources, Part A: Recovery, Utilization, and Environmental Effects, 41(12), 1403-1433.
[48] Fergus, J.W. 2010. Recent developments in Cathode materials for lithium-ion batteries. Journal of Power Sources, 195(4), 939-954.
[49] C.M Julien, A. Mauger, K. Zaghib, H. Groult. 2014. Comparative issues of Cathode material for Li-ion Batteries. Inorganics, 2, 132-154.
[50] Y. Sharma, N. Sharma, G.V. Subba Rao, B.V.R. Chowdari, 2007, Nanophase $ZnCo_2O_4$ as a high-performance anode material for Li-ion batteries. Advanced Functional Materials, 17, 2855-2861.

[51] P.A. Vinosha, L.A. Mely, J.E. Jeronsia, S. Krishnan, S.J. Das, 2017, Optik-International Journal for Light and Electron Optics, 134, 99-108.

[52] P.S. Yoo, D.A. Reddy, Y. Jia, S.E. Bae, S. Huh, C. Liu, J. 2017. Magnetic core-shell ZnFe2O4/ZnS nanocomposites for photocatalytic application under visible light. Colloid Interface Sci., 486, 136-143.

[53] F.O. Agyemang, H. Kim. 2016. Electrospun $ZnFe_2O_4$- based nanofiber composites with enhanced super capacitive properties. Mater. Sci. Eng. B, 211, 141-148.

[54] C.G. Han, C. Zhu, G. Saito, N. Sheng, T. Nomura, T. Akiyama. 2017. Enhanced cycling performance of surface-doped $LiMn_2O_4$ modified by a Li_2CuO_2-Li_2NiO_2 solid solution for rechargeable lithium-ion batteries, Electrochim. Acta, 224, 71-79.

[55] C.G. Han, C. Zhu, G. Saito, T. Akiyama. 2016. Improved electrochemical performance of $LiMn_2O_4$ surface modified by a Mn^{4+} - rich phase for rechargeable Lithium-ion batteries. Electrochim. Acta, 209, 225-234.

[56] S. Li, J. Liu, L. Li, X. Li, J. Jing, X. Cui. 2015. Compatibility of Lithium difluoro (sulfato) borate-based electrolyte for $LiMn_2O_4$ cathode. Appl. Surf. Sci., 330 (2015) 316-320.

[57] W. Luo. 2015. Effect of morphology on the physical and electrochemical properties of the high-voltage spinel cathode $LiMn_{1.5}Ni_{0.5}O_4$. J. Alloys Compd., 636 (2015) 24-28.

[58] J. Cao, K. Xiao, F. Jiang, X. Xi, D. Liao, D. He. 2016. Surface design with spinel $LiMn_{1.5}Ni_{0.5}O_4$ for improving electrochemical properties of $LiNi_{0.5}Co_{0.2}Mn_{0.3}O_2$ at high cut-off voltage. Mater. Lett., 184, 29-33.

[59] M.K. Datta, M. Ramanathan, P. Jampani, P. Saha, R. Epur, K. Kadakia, S.J. Chung, P. Patel, B. Gattu, A. Manivannan. 2014. High energy mechano-chemical milling: Convenient approach to the synthesis of $LiMn_{1.5}Ni_{0.5}O_4$ high voltage cathode for lithium-ion batteries. Mater. Sci. Eng. B, 190, 119-125.

[60] S. Kim, C. Kim, J.-K. Noh, S. Yu, S.-J. Kim, W. Chang, W.C. Choi, K.Y. Chung, B.-W. Cho. 2012. Synthesis of layered-layered $xLi_2MnO_3.(1-x)LiMO_2$ (M= Mn, Ni, Co) nanocomposite electrodes materials by mechanochemical process. J. Power Sources, 220, 422-429.

[61] D. Kim, J. Gim, J. Lim, S. Park, J. Kim, 2010. Synthesis of $xLi_2MnO_3.(1-x)LiMO_2$ (M= Cr, Mn, Ni, Co) nanocomposite and their electrochemical properties. Mater. Res. Bull., 45, 252-255.

[62] R. Gummow, A. De Kock, M. Thackeray, Improved capacity retention in rechargeable 4 V lithium/lithium-manganese oxide (spinel) cells, Solid State Ionics, 69 (1994) 59-67.

[63] S. Lee, Y. Cho, H.K. Song, K.T. Lee, J. Cho, Carbon-Coated Single-Crystal LiMn2O4 Nanoparticle Clusters as Cathode Material for High-Energy and High-Power Lithium-Ion Batteries, Angew. Chem. Int. Ed., 51 (2012) 8748-8752.

[64] A. Momchilov, V. Manev, A. Nassalevska, A. Kozawa, Rechargeable lithium battery with spinel-related MnO2 II. Optimization of the LiMn2O4 synthesis conditions, J. Power Sources, 41 (1993) 305-314.

[65] A. Eftekhari, 2017. $LiFePO_4$/C nanocomposites for lithium-ion batteries. J. Power Sources, 343, 395-411.

[66] C. Gong, Z. Xue, S. Wen, Y. Ye, X. Xie, 2016. Advanced carbon materials/olivine $LiFePO_4$ composite cathode for lithium-ion batteries. J. Power Sources, 318 (2016) 93-112.

[67] J. Xu, G. Chen, 2010. Effect of doping on the electronic properties of $LiFePO_4$: A first-principles investigation. Physica B: Condensed Matter, 405 (2010) 803-807.

[68] W.J. Zhang, 2011. Structure and performance of $LiFePO_4$ cathode materials: A review. J. Power Sources, 196 (2011) 2962-2970.

[69] A. Nazari and S. Farhad, 2017. Heat generation in lithium-ion batteries with different nominal capacities and chemistries, Applied Thermal Engineering 125, p.p. 1501-1517.

[70] J. Baron, G. Szymanski, and J. Lipkowski, 2011. Electrochemical methods to measure gold leaching current in an alkaline thiosulfate solution, Journal of electroanalytical chemistry 662 (1), p.p. 57-63.

[71] S. Venkatraman, J. Choi, and A. Manthiram, 2004. Factors influencing the chemical lithium extraction rate from layered $LiNi_{1-y-z}Co_yMn_zO_2$ cathodes. Electrochemistry communications 6 (8), p.p. 832-837.
[72] H.A. Kiehne, Battery technology handbook, CRC Press, 2003.
[73] K. Jalkanen, T. Aho, K. Vuorilehto, 2013. Entropy change effects on the thermal behavior of a $LiFePO_4$/graphite lithium-ion cell at different stages of charge, J. Power Sources, 243, 354-360.
[74] Z. Li, J. Huang, B.Y. Liaw, J. Zhang, 2017. On state-of-charge determination for lithium-ion batteries, J. Power Sources, 348, 281-301.
[75] X. Li, J. Jiang, L.Y. Wang, D. Chen, Y. Zhang, C. Zhang, 2016. A capacity model based on charging process for the state of health estimation of lithium-ion batteries, Appl. Energy, 177, 537-543.
[76] R.A. Huggins, 2000. Reference electrodes and the Gibbs phase rule, Solid State Ionics, 136,1321-1328.
[77] M. Hannan, M. Hoque, A. Mohamed, and A. Ayob,2017. Review of energy storage systems for electric vehicle applications: Issues and challenges, Renewable and Sustainable Energy Reviews 69, p.p. 771-789.
[78] E. Hosseinzadeh, J. Marco and P. Jennings, 2017. Electrochemical-thermal modeling and optimization of lithium-ion battery design parameters using analysis of variance, Energies 10 (9), 1278.
[79] A. Jokar, B. Rajabloo, M. Désilets, and M. Lacroix, 2016. Review of simplified Pseudo-two-dimensional models of lithium-ion batteries, Journal of Power Sources 327, p.p. 44-55, 2016.
[80] J. Yang, X. Wei, H. Dai, J. Zhu, and X. Xu, Lithium-ion battery internal resistance model based on the porous electrode theory, presented at the 2014 IEEE Vehicle Power and Propulsion Conference (VPPC), 2014 (unpublished).
[81] P. Wu, J. Romberg, H. Ge, Y. Zhang, and J. Zhang, presented at the Society of Automotive Engineers (SAE)-China Congress, 2016 (unpublished).
[82] J. Newman and W. Tiedmann, 1975. Porous-electrode theory with battery application, AICHE Journal, vol. 21(1), p.p. 25-41, 1975.
[83] S. Srivastav, P. Tammela, D. Brandell, and M. Sjödin, 2015. Understanding ionic transport in polypyrrole/nano cellulose composite energy storage devices, Electrochimica Acta 182, p.p. 1145-1152, 2015.
[84] A. Melcher, C. Ziebert, M. Rohde, and H. J. Seifert, 2016. Modeling and simulation of the thermal runaway behavior of cylindrical Li-ion cells- computing of critical parameters, Energies 9 (4), 292.
[85] C. Ziebert, A. Melcher, B. Lei, W. Zhao, M. Rohde, and H. Seifert, 2017. Electrochemical-Thermal characterization and thermal modeling for batteries, in Emerging Nanotechnologies in Rechargeable Energy Storage Systems (Elsevier), pp. 195-229.
[86] K. Li, J. Yan, H. Chen and Q. Wang, Water cooling based strategy for lithium-ion battery pack dynamic cycling for thermal management, Applied Thermal Engineering 132, p.p. 575-585, 2018.
[87] Z. Khalik, H. J. Bergveld, and M. Donkers, presented at the 2020 American Control Conference (ACC), 2020 (unpublished).
[88] J. Li, D. Wang, L. Deng, Z. Cui, C. Lyu, L. Wang, and M. Pecht, 2020. Aging modes analysis and physical parameter identification based on a simplified electrochemical model for lithium-ion batteries, Journal of Energy Storage 31, 101538.
[89] Y. Qi, T. Jang, V. Ramadesigan, D. T. Schwartz, and V. R. Subramanian, 2017. Is there a benefit in employing graded electrodes for lithium-ion batteries, Journal of The Electrochemical Society 164 (13), A3196.
[90] N. Li, L. Fu, and K. Jiang, 2019. Gas evolution and the effects on ionic transport inside the lithium-ion battery, Engineering Computations.
[91] J. Xu, B. Liu, X. Wang, and D. Hu, 2016. A computational model of 18650 lithium-ion battery with coupled strain rate and SOC dependencies, Applied Energy 172, p.p. 180-189.

[92] Y. Liu, S. Tang, L. Li, F. Liu, L. Jiang, M. Jia, Y. Ai, C. Yao and H. Gu, 2020. Simulation and parameter identification based on electrochemical-thermal coupling model of a power lithium-ion battery, Journal of Alloys and Compounds, 156003.

[93] Y. Dai and V. Srinivasan, 2015. On graded electrode porosity as a design tool for improving the energy density of batteries, Journal of The Electrochemical Society 163 (3), A406.

[94] S. Panchal, I. Dincer, M. Agelin-Chaab, R. Fraser and M. Fowler,2017. Transient electrochemical heat transfer modeling and experimental validation of a large sized $LiFePO_4$/graphite battery, International Journal of Heat and Mass Transfer 109, p.p. 1239-1251.

[95] Dai, M., Huo, C., Zhang, Q., Khan, K., Zhang, X., and Shen, C., (2018) Electrochemical Mechanism and Structure Simulation of 2D Lithium-Ion Battery," Advanced Theory and Simulations 1 (10), 1800023.

[96] Singh, P., Khare, N., and Chaturvedi. P, "COMSOL Modelling for Li-ion Battery Diagnostics, 2014.

[97] Uddin, K., Perera, S., Widanage, W., Somerville, L., and Marco, J., (2016) Characterising lithium-ion battery degradation through the identification and tracking of electrochemical battery model parameters, Batteries 2 (2), 13.

[98] K. Somasundaram, E. Birgersson and A. S. Mujumdar, 2012. Thermal-electrochemical model for passive thermal management of a spiral-wound lithium-ion battery, Journal of Power Sources 203, p.p. 84-96.

[99] K. Shaju, G. S. Rao and B. Chowdari, 2003. EIS and GITT studies on oxide cathodes, O2-$Li_{(2/3)+x}$ $(Co0.15Mn_{0.85})O_2$ (x=0 and 1/3), Electrochimica Acta 48 (18), p.p. 2691-2703.

[100] H. Li, C. Liu, A. Saini, Y. Wang, H. Jiang, T. Yang, L. Chen, C. Pan, and H. Shen, 2019. Coupling multi-physics simulation and response surface methodology for the thermal optimization of ternary prismatic lithium-ion battery, Journal of Power Sources 438, 226974.

[101] Zhang, Q., D.Wang, B.Yang, X. Cui, and X. Li. 2020. Electrochemical model of lithium-ion battery for wide frequency range applications. Electrochimica Acta, 3.

[102] Liu, Y., S.Tang, L.Li, F.Liu, L.Jiang, M.Jia, Y.Ai, C.Yao, and H.Gu. 2020. Simulation and parameter identification based on electrochemical-thermal coupling model of power lithium-ion battery. Journal of Alloys and Compounds, 844.

[103] S. Gimenez, C. Schilde, L. Frobose, S. Ivanov, and A. Kwade. 2020. Mechanical, Electrical, and Ionic behavior of Lithium-ion battery electrodes via discrete element method simulation. Energy Technology, 8 (2).

[104] Raijmakers, L.H.J, D.L. Danilov, R.A. Eichel, P.H.L. Notten. 2020. An advanced all-solid-state Li-ion battery model. Electrochemica Acta, 330.

[105] C. Edouard, M.Petit, C. Forgez, J.Bernard and R.Revel, 2016. Parameter sensitivity analysis of a simplified electrochemical and thermal model for Li-ion batteries aging, Journal of Power Sources, vol. 33, p.p. 482-494.

[106] L.Zhang, C. Lyu, L. Wang, W.Luo and K. Ma, 2013. Thermal-Electrochemical modeling and parameter sensitivity analysis of lithium-ion battery, Chemical Engineering, Vol. 33, p.p. 943-948.

[107] Y.H.Chen, C.W.Wang, X. Zhang and A.M. Sastry, 2010. Porous cathode optimization for lithium cells: Ionic and electronic conductivity, capacity and selection of material, Journal of Power Sources, vol. 195(9), p.p. 2851-2862.

[108] W.Wu, X.Xiao, and X.Huang, 2012. A multiphysics model for the in situ stress analysis of the separator in a lithium-ion battery cell, Electrochemica Acta, vol. 83, p.p. 227-240.

[109] S. Golmon, K. Maute and M.L.Dunn, 2014. Battery impedance modeling and comprehensive comparisons of state-of-the-art cylindrical 18650 battery cells considering cell's price, Impedance, specific energy, and C-rate, Journal of Power Sources, vol.253, p.p. 239-250, 2014.

[110] J.Li, Y.Cheng, L. Ai, M.Jia, S.Du, B. Yin, S. Woo, and H. Zhang, 2015. 3D simulation on the internal distributed properties of lithium-ion battery with planar tabbed configuration, Journal of Power Sources, vol. 293, p.p. 993-1005.

[111] J.Li, Y.Cheng, M.Jia, Y.Tang, Y.Lin, Z.Zhang, and Y.Liu. 2014. An electrochemical-thermal model based on dynamic responses for lithium iron Phosphate battery, Journal of Power Sources, vol. 255, p.p. 130-143.

[112] A.M.Bizeray, S.Zhao, S.R.Duncan, and D.A Howey. 2015. Lithium-ion battery thermal-electrochemical model-based state estimation using orthogonal collocation and a modified extended Kalman filter, Journal of Power Sources, vol.296, p.p. 400-412.

[113] J.M.Tarascon and M. Armand. 2010. Materials for Sustainable Energy: A Collection of peer-reviewed research and review articles from nature Publishing group, p.p. 171-179.

[114] W. Tong, K. Somasundaram, E. Birgersson, A. S. Mujumdar, and C. Yap. 2016. Thermo-electrochemical model for forced convection air cooling of a lithium-ion battery module, Applied Thermal Engineering 99, 672-682.

[115] Jiang, T., Zhang, S., Qiu, X., Zhu, W., and Chen, L. 2007. Preparation and characterization of silicon-based three-dimensional cellular anode for lithium-ion battery, Electrochemistry communications 9 (5), 930-934.

[116] Zavalis, T., Behm, M., and Lindbergh, G. 2012. Investigation of short-circuit scenarios in a lithium-ion battery cell, Journal of The Electrochemical Society 159 (6), A848-A859.

[117] Smith, K., and Wang, C., (2006) Power and thermal characterization of a lithium-ion battery pack for hybrid-electric vehicles, Journal of power sources 160 (1), 662-673.

[118] Thanagasundram, S., Arunachala, R., Makinejad, K., Teutsch, T., and Jossen, A., 2012 (unpublished) presented at the European Electric Vehicle Congress.

[119] Ye, Y., Shi, Y., Cai, N., Lee, J., and He, X., (2012) Electro-thermal modeling and experimental validation for lithium-ion battery, Journal of Power Sources 199, 227-238.

[120] Hasham, A.M., Abbas, S.M., Hou, X., Eid, A.E., Abdel-Ghang, A.E., 2019. A facile one-step synthesis method of spinel LiMn2O4 Cathode Material for Lithium Batteries.Journal of Heliyon, 5 (7).

[121] Helan, M., and Berchmans, J., 2011. Low-Temperature Synthesis of Lithium Manganese Oxide Using LiCl-Li_2CO_3 and Manganese Acetate Eutectic mixture. Journal of Materials and Manufacturing Process, 26, 1369-1373.

[122] Hasnain, S. M. 1998. Review on Sustainable Thermal Energy Storage Technologies, Part I: Heat storage materials and techniques. Energy Conversion and Management, 39 (11): 1127-1138.

[123] Kim, H.J., T. Krishna, K.Zeb, V.Rajangam, C.V.V.M. Gopi, S. Sambasivam, K.V.G.Raghavendra, I.M. Obaidat. 2020. A comprehensive Review on Li-ion Battery Materials and their recycling techniques. Electronics, 9 (7), 1161.

[124] Karo, J., and Brandell, D., 2009. A molecular dynamics study of the influence of side-chain length and spacing on lithium mobility in non-crystalline $LiPF_6.PEO_x$; x=10 and 30. Journal of solid-state Ionics, 180(23-25), 1272-1284.

[125] Lee, W., S.Muhmood, C.Sergey, H.Lee, J.Yoon, Y.M.Kang, W.S.Yoon. 2020. Advances in the cathode materials for lithium rechargeable batteries. Angewandte chemie International Edition 59(7): 2578-2605.

[126] Li, X. 2015. Modeling and simulation study of a metal-free organic-inorganic aqueous flow battery with the flow-through electrode. Electrochimica Acta, 170, 98-109.

[127] Pannala, S., Turner, J.A., Allu, S., Elwasif, W.R., Kalnaus, S., Simunovic, S., Kumar, A., Billings, J.J., Wang, H., and Nanda, J., 2015. Multiscale modeling and characterization for performance and safety of lithium-ion batteries. Journal of Applied Physics, 118, 072017. Pongsaksawad, W., Powell, A.C., and

[128] Dussault, D., 2007. Phase-field Modelling of Transport-limited Electrolysis in solid and liquid states. Journal of Electrochemical Society, 154 (6), F122-F133.

[129] Powell, A.C., and Pongsaksawad, W., 2007. Simulation of Electrochemical Process II. Edited by V.G. DeGiorgi, C.A. Brebbia, and R.A. Adey, wit press/ Computational Mechanics Publications, Southampton, 54, 43-52.

[130] Qin, J., S. Zhao, X. Liu, and Y.Liu. 2020. Simulation study on thermal runaway suppression of 18650 lithium battery. Energy Sources, Part A: Recovery, Utilization, and Environmental Effects, 1-13.

[131] Rewatkar, M.R., and D.Z.Shende. 2020. Experimental investigation on cenosphere-based paper battery. Energy Sources, Part A: Recovery, Utilization, and Environmental Effects, 42(16), 2018-2033.

[132] Sharma, S., Panwar, A.K., and Tripathi, M.M., 2021. Thermal-Electrochemical Modelling and Analysis of Different Cathode-Anode pairs for Lithium-ion Battery. Journal of Advanced Electrical and Computer Engineering, 21, 57-64.

[133] Tasaki, K., and Harris, S.J., 2010. Computational Study on the solubility of Lithium salts formed on Lithium-Ion Battery Negative Electrode in Organic Solvents. Journal of Physical Chemistry C, 114 (17), 8076-8083.

[134] Wang, C.Y., Gu, W.B., and Liaw, B.Y., 1998. Micro-macroscopic Coupled Modelling of Batteries and Fuel Cells. I. Model Development. Journal of Electrochemistry, 145 (10), 3407-3417.

[135] Xia,W., A. Mahmood, R. Zou, and Q.Xu. 2015. Metal-organic Frameworks and their derived nanostructures for electrochemical energy storage and conversion. Energy & Environment Science, 8 (7), 1837-1866.

[136] Arora, P., M. Doyle, A.S. Gozdz, R.E.White, and J. Newman. 2000. Comparison between computer simulations and experimental data for high-rate discharges of plastic lithium-ion batteries. Journal of Power sources, 88(2), 219-231.

[137] Baena-Moreno, F.M., M. Rodriquez-Galan, F.Vega, B. Alonso-Farinas, L.F. Vilches Arenas, and B. Navarrete. 2019. Carbon capture and utilization technologies: a literature review and recent advances. Energy Sources, Part A: Recovery, Utilization, and Environmental Effects, 41(12), 1403-1433.

[138] Fadzil, A.F.M., Bustam, M.A., Aziz, N.D.A., 2017. Characterization of doped $LiMn_2O_4$ powder prepared by the Sol-gel method: Thermal analysis and XRD studies. AIP conference Proceeding, 1877.

[139] Ali, K., Raza, H.A., Malik, M.I., Shamsah, S.I., Amna, R., and Sarfraz, A., 2020. Effect of $LiMn_2O_4$, Nanofibers of $LiMn_2O_4$, and Graphene/Polyaniline/Carbon Nanotube as Electrode Materials in the Fuel Cell. Journal of New Materials for Electrochemical Systems, 23, 37-42.

[140] Chiovoloni, S., Moran, C., LeMaire, P.K., and Singhal, R., 2017. Optimization of Synthesis Conditions of $LiMn_{2-x}Fe_xO_4$ Cathode Materials based on Thermal Characterizations. American Journal of Analytical Chemistry, 8, 51-59.

[141] K. Tang, X. Yu, J. Sun, H. Li, X. Huang. 2011. Kinetic analysis on $LiFePO_4$ thin films by CV, GITT, and EIS. Electrochim. Acta, 56, 4869- 4875.

[142] F. Deng, X. Zeng, J. Zou, J. Huang, X. Xiong, X. Li. 2011. Synthesis of in situ network-like vapor-grown carbon fiber improved LiFePO4 cathode materials by microwave pyrolysis chemical vapor deposition. J. Alloys Compd., 509, L324-L327.

[143] Z. Su, Z. Lu, X. Gao, P. Shen, X. Liu, J. Wang. 2009. Preparation and electrochemical properties of Indium- and sulfur-doped LiMnO2 with orthorhombic structure as cathode materials. J. Power Sources, 189, 411-415.

[144] E.M. Jin, B. Jin, Y.S. Jeon, K.H. Park, H.B. Gu. 2009. Electrochemical properties of $LiMnO_2$ for lithium polymer battery. J. Power Sources, 189, 620-623.

[145] B. Li, Y. Yu, J. Zhao. 2015. Facile synthesis of spherical $x Li_2MnO_3.(1-x)Li(Mn_{0.33}Co_{0.33}Ni_{0.33})O_2$ as cathode materials for lithium-ion batteries with improved electrochemical performance. J. Power Sources, 275, 64-72.

[146] S. Basu, P.P. Dahiya, M. Akhtar, S.K. Ray, J.K. Chang, S.B. Majumder. 2016. Skin bioelectronics towards long-term, continuous health monitoring. Mater. Sci. Eng. B.

[147] Y. Li, Y. Makita, Z. Lin, S. Lin, N. Nagaoka, X. Yang. 2011. Synthesis and characterization of lithium manganese oxides with core-shell $Li_4Mn_5O_{12}@Li_2MnO_3$ structure as lithium battery electrode materials. Solid State Ionics, 196, 34-40.

[148] J. Pires, L. Timperman, A. Castets, J.S. Peña, E. Dumont, S. Levasseur, R. Dedryvere, C. Tessier, M. Anouti. 2015. Role of propane sultone as an additive to improve the performance of a lithium-rich cathode material at a high potential RSC Advances, 5 (2015) 42088-42094.

[149] J. Lin, D. Mu, Y. Jin, B. Wu, Y. Ma, F. Wu. 2013. Li-rich layered composite Li $[Li_{0.2}Ni_{0.2}Mn_{0.6}]O_2$ synthesized by a novel approach as cathode material for lithium-ion battery. J. Power Sources, 230 (2013) 76-80.

[150] P. Suresh, A.K. Shukla, N. Munichandraiah. 2006. Characterization of Zn- and Fe-substituted $LiMnO_2$ as cathode materials in Li-ion cells. J. Power Sources, 161, 1307-1313.

[151] S. Castano-Solis, D. Serrano-Jimenez, J. Fraile-Ardanuy, J. Sanz-Feito. 2019. Hybrid characterization procedure of Li-ion battery packs for wide frequency range dynamics applications, Electric Power Systems Research, 166, 9-17.

[152] C.C. Hua, M.-Y. Lin. 2000. A study of charging control of lead-acid battery for electric vehicles, in ISIE'2000. Proceedings of the 2000 IEEE International Symposium on Industrial Electronics (Cat. No. 00TH8543), IEEE, pp. 135-140.

[153] S. Buller, E. Karden, A. Lohner, R.W. De Doncker.1998. LabView-based universal battery monitoring, and management system, in INTELEC-Twentieth International Telecommunications Energy Conference (Cat. No. 98CH36263), IEEE, pp. 630-635.

[154] R. Rizk, H. Louahlia, H. Gualous, P. Schaetzel, G. Alcicek. 2019. Experimental analysis on Li-ion battery local heat distribution, Journal of Thermal Analysis and Calorimetry, 1-15.

[155] A. Jamaluddin, L. Sihombing, A. Supriyanto, A. Purwanto, M. Nizam. 2013. Design real-time battery monitoring system using LabVIEW interface for Arduino (lifa), in 2013 Joint International Conference on Rural Information & Communication Technology and Electric-Vehicle Technology (ICT & ICeV-T), IEEE, pp. 1-4.

[156] L. Rambaldi, E. Bocci, F. Orecchini. 2011. Preliminary experimental evaluation of four-wheel motors, batteries plus ultracapacitors, and series hybrid powertrain, Applied Energy, 88, 442-448.

[157] A. Jamaluddin, A. Nuraini, A. Jumari, A. Purwanto. 2017. A Monitoring System of Battery LiFePO4 for Assessment Stand-Alone Street Light Photovoltaic System Based on LabVIEW Interface for Arduino, International Journal of Power Electronics and Drive Systems, 8, 926.

[158] D.A. Notter, M. Gauch, R. Widmer, P. Wager, A. Stamp, R. Zah, H.J. Althaus. 2010. Contribution of Li-ion batteries to the environmental impact of electric vehicles, in, ACS Publications.